Infragravity waves

–

Propagation, dissipation and sediment transport in the inner surf zone of a low sloping beach

Master Thesis

A.T.M. de Bakker
Supervisor: B.G. Ruessink
Utrecht University
Faculty of Geosciences
Department Physical Geography
3118533
November 2011
2nd version

Preface

This master thesis is the result of a year's work under the supervision of Gerben Ruessink. I would like to thank him for all the guidance and time he invested into this research and therefore also in me. Furthermore, I would like to thank the technicians of the department of physical geography, Henk Markies and Marcel van Maarseveen, for installing and maintaining the equipment and helping out when there were problems.
I would also like to thank my fellow Master students Emily McCullough and Aline Pieterse, for the nice time during the fieldwork on Ameland. I would like to thank Aline especially, for helping me with the positioning and maintenance of the miniframes, which I could not have done alone, and also for all the helpful advice and discussions. Finally, I would like to thank my family and my boyfriend Paolo, for all the support they gave, and the interest they expressed.

Content page

Introduction

This master thesis will discuss observations of propagation, dissipation and sediment transport behavior of infragravity waves in the inner surf zone of a low sloping beach, on Ameland, The Netherlands.

Infragravity waves have been studied over the past sixty years since their initial observations by *Munk [1949]* and *Tucker [1950]*. Infragravity waves, sometimes also referred to as subharmonic waves, low frequency waves or (bound) long waves, are considered to play a major role in beach erosion under high energetic conditions. Because during high energetic conditions the short sea and swell waves break further offshore, the infragravity wave can dominate in the inner nearshore zone. Accordingly, sediment transport can be dominated by infragravity waves. The boundary between short waves and long waves is between 0.05 and 0.04 Hz, depending on the geographical location (e.g. open ocean coast versus semi-sheltered sea). The short waves have a typical frequency between 0.05 and 0.33 Hz, and the low frequency waves have a typical frequency between 0.005 and 0.05 Hz.
Certain processes regarding infragravity waves are still not well understood. Firstly, the way in which infragravity waves are transformed from bound to free waves is still under dispute. Furthermore, infragravity waves do not always fully reflect at the shoreline but experience significant energy loss, the processes that are responsible for this require further research. Thirdly, the role of infragravity waves in sediment suspension and transport is not understood, as the direction of the sediment transport at infragravity frequencies does not always show a clear spatial pattern.

This master thesis is divided into two parts. The first part gives an overview of the current available literature and discusses the processes mentioned above that are not well understood. In the second part of the thesis the research questions for the master research are defined. Furthermore, the field research will be discussed and the analysis of the obtained data will be given.

Part I - Literature review

Lay-out

The lay-out of the literature review is as follows. The generation, propagation and reflection of the infragravity wave will be discussed in chapter 1. From the obtained results it can be concluded that there is significant energy dissipation of the infragravity wave in the nearshore zone. The potential mechanisms responsible for this energy loss will be discussed in chapter 2. Then, the role of infragravity waves in sediment suspension and sediment transport will be studied in chapter 3.

1. Infragravity wave generation and propagation

1.1 Generation of infragravity waves

Short wave groups (frequency of 0.05-0.33 Hz) force a second order long wave (frequency of 0.005-0.5 Hz) that is in anti-phase with the wave group (Figure 1.1).

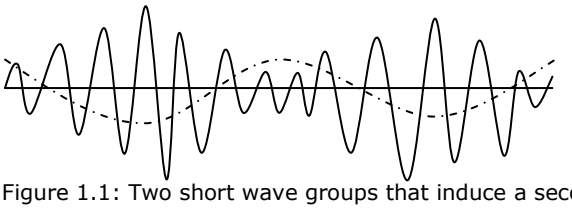

Figure 1.1: Two short wave groups that induce a secondary long wave.

Because high waves have a larger mass transport than low waves, the difference in momentum flux causes fluid to be transferred from groups of high waves to groups of low waves. This process causes the development of a 'set down wave' which has the same wave length and period as the short wave groups. This second order wave is usually referred to as infragravity wave, subharmonic wave, low frequency wave or (bound) long wave. This bound long wave is quadratically related to sea-swell energy as predicted by second-order wave theory, and is therefore affected by the behavior of short wave groups at local features (e.g. sloping bed and bars). When the short waves break in shallow water, the group structure disappears and the long wave is not bound anymore, and becomes a free wave.

Another possible mechanism for the generation of free waves is the time-varying breakpoint, based on a model of *Symonds et al. [1982]*. The idea is that alternating groups of high and low waves generate a time varying breakpoint which induces a time varying wave set-up and hence infragravity waves. The model predicts the seaward and shoreward propagating long waves at the wave group frequency. Figure 1.2 shows a schematic representation of this long wave structure at two sides of the mean breakpoint. It is assumed that the breakpoint is limited to a small zone. Figure 1.2a shows the situation of an incident (IBFLW) and outgoing (OBFLW) breakpoint forced long wave. The incident wave reflects (RBFLW) and propagates offshore. If the phase of both outgoing waves coincides, the infragravity wave will be amplified. This is possible when the breakpoint is situated at a nodal point of the free long wave. If the phase of the outgoing waves is 180 degrees out of phase (Figure 1.2b) the infragravity wave will be damped. This is occurring when the breakpoint is situated at an anti-node.

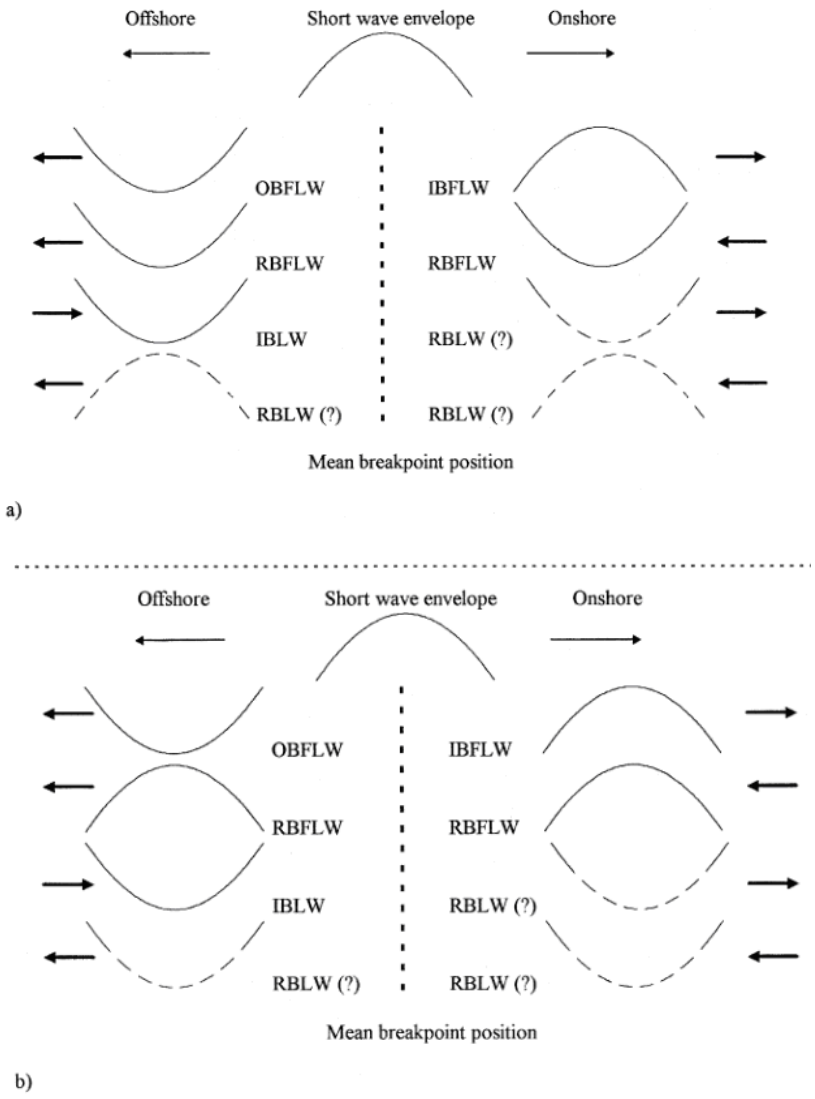

Figure 1.2: Expected long wave phase due to surf beat generation by a time-varying breakpoint. IBFLW, RBFLW, OBFLW – incident, reflected and outgoing breakpoint forced long wave. IBLW-incident bound long wave, RBLW-released/reflected 'bound' long wave. (a) Maximum response, mean breakpoint at a nodal point for a free standing long wave. (b) Minimum response, mean breakpoint at an antinode of a free standing long wave. Source: Baldock et al. [2000].

Battjes et al. [2004] suggested that the mechanism dominating free long wave generation depends on the bed slope. With a steep slope the time-varying breakpoint would be more effective, while in a mild-sloping regime the released bound long wave is dominant.

As predicted by second order wave theory, forced infragravity energy is quadratic related to sea-swell energy. This is confirmed by *Herbers et al. [1995a].* Forced infragravity energy related to swell energy at locations in deep water (8, 30 and 204 m water depth) is visible in Figure 1.3a.

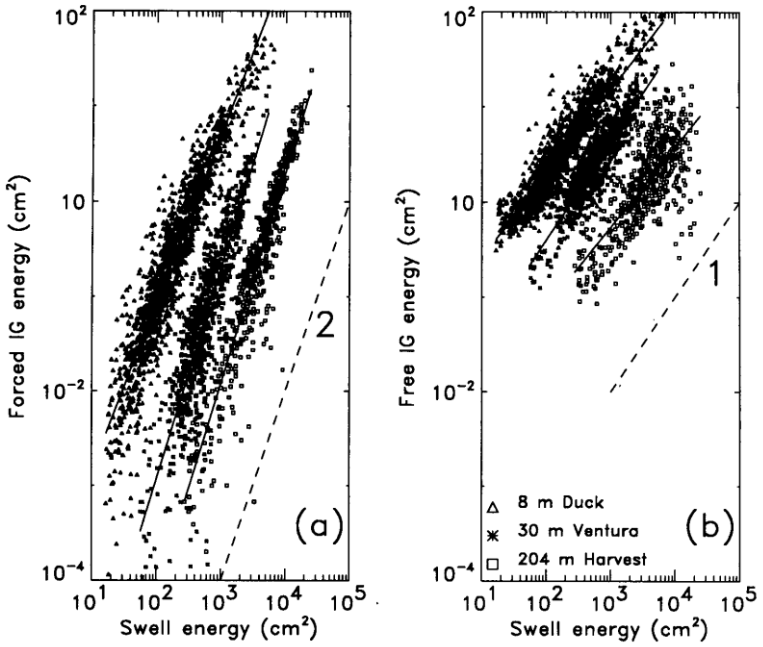

Figure 1.3: (a) Forced infragravity energy, (b) free infragravity energy. Infragravity energies were integrated over the frequency ranges 0.004-0.05 Hz and 0.0004-0.04 Hz in the Atlantic and Pacific, respectively. The data are from 8 m depth at Duck (triangles, upper clouds), 30 m at Ventura (asterisks, middle clouds), and 204 m at Harvest Platform (squares, lower clouds). The solid lines are least-squares-fit curves to the logarithms of the observed energies. Dashed lines labelled 1 and 2 indicate linear and quadratic dependencies, respectively. Source: [Herbers et al., 1995a].

If the source of free infragravity energy was initiated by forced long waves that are released at a fixed location, then it too would be more or less quadratic related to sea-swell energy. However, since not all short waves break at the same water depth (larger short waves break further offshore in deeper water) and energy transfer to low frequencies is therefore not taking place at the same location, the relation is less than quadratic (Figure 1.3b) and is approaching linearity. Also the time-varying breakpoint is predicting a weaker than quadratic relation for free wave energy.

The outgoing free wave can be subdivided into edge waves and leaky waves. Leaky waves propagate to deeper water, whereas edge waves are trapped in the nearshore by refraction and travel along the beach. It is assumed that depth contours are parallel to the coast. As edge waves propagate obliquely towards the coast, water depth varies along the wave crest (Figure 1.4).

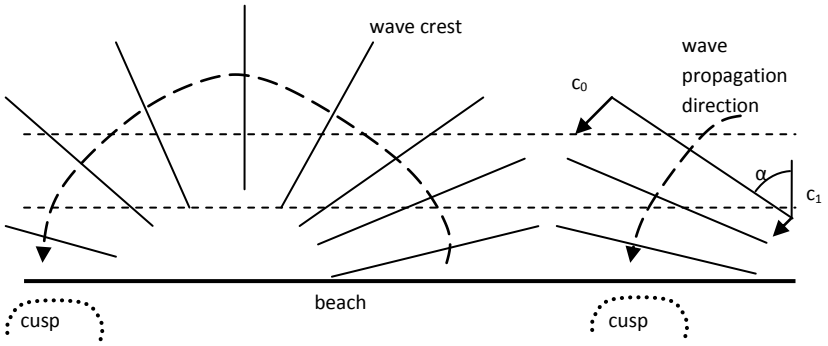

Figure 1.4: Schematic presentation of edge wave development. α represents the angle of incidence to shore normal (°), c_0 equals wave propagation velocity in deep water and c_1 equals wave propagation velocity in shallow water (m/s). The dashed lines parallel to the beach represent depth contour lines.

The wave propagation velocity depends on water depth through the relation $c = (gh)^{0.5}$. As the wave crest in deeper water travels faster, the crest bends towards the coast. If the angle of incidence is large enough part of the wave crest will reflect while the other part is still propagating towards to coast. The reflected wave crest bends again based on the principle of wave propagation velocity differences. At a certain point wave crests appear in the shore normal direction, which results in a repetition of propagation towards the coast.

Leaky waves and edge waves may occur at the same time, but it is very difficult to separate them from each other when analyzing the field data, unless an extensive longshore array of instruments is used. Since the waves are present in a large zone, they may be affected by larger-scale geographical settings. Differences in settings might cause differences in trapping and hence in the relative amount of edge and leaky waves.

1.2 Infragravity energy

1.2.1 Temporal variations in the surf zone

Ruessink [1998a] observed the contribution of bound and free long waves to the total infragravity energy in 3.5 m water depth of a mild sloping beach. The total infragravity energy levels (E_{ig}) are well related to offshore short-wave energy ($E_{ss,0}$) (Figure 1.5 left). Short wave breaking (closed circles) does not seem to affect the relation. The bound long wave energy (E_{bnd}) increases rapidly with increasing offshore short wave energy. At locations more offshore from the measured location presented in Figure 1.5, the relation was more or less quadratic. However, at 3.5 m water depth the relation decreased to 1.4, possibly due to the limited number of observations, but it could also imply a decrease in bound long waves in more shallow water. Under breaking conditions, the bound long wave energy remained constant or even decreased (Figure 1.5 middle). It can be seen that the stop in growth of the bound long wave coincides with an enhanced increase in free long wave energy. This implies a transformation of bound to free long wave energy inside the surf zone.

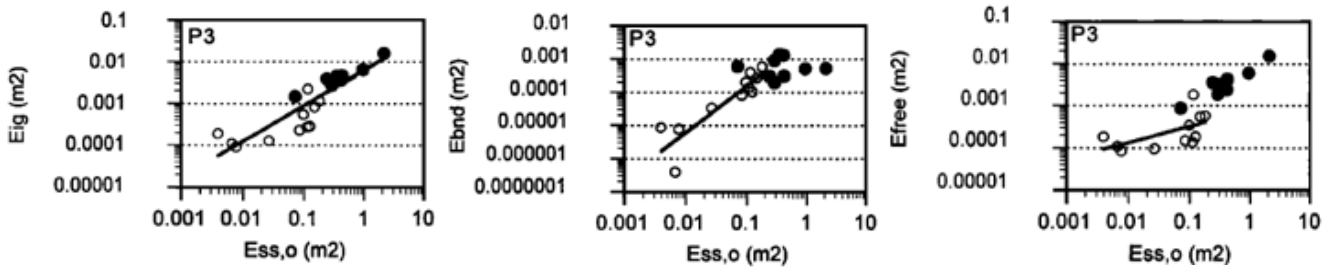

Figure 1.5: (left) Measured total, (middle) bound, and (right) free infragravity energy E_{ig}, E_{bnd} and E_{free}, respectively, as a function of the offshore short-wave energy $E_{ss,o}$ at 3.5 m water depth. Open and solid circles refer to nonbreaking and breaking conditions, respectively. The solid line in each plot is the best linear fit to the logarithm of the data (for E_{bnd} and E_{free} nonbreaking data only). Source: Ruessink [1998a].

When analyzing the observed ratio of bound to total energy as a function of relative wave height at a water depth of 3.5 m (Figure 1.6), it can be concluded that the ratio was low during low energy conditions and increased with relative wave height. It reached a maximum just before the start of the breaking of short waves ($H_{ss}/h=0.33$). After breaking, the ratio decreased again to negligible values in a saturated wave field.

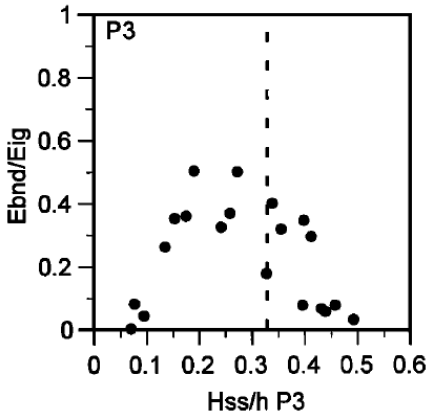

Figure 1.6: Observed ratio of bound to total infragravity energy E_{bnd}/E_{ig} as a function of relative wave height H_{ss}/h at P3. The dashed vertical lines mark the onset of wave breaking ($H_{ss}/h=0.33$). Source: Ruessink [1998a].

Sheremet et al. [2002] observed the same behavior as *Ruessink [1998a]* in their field campaign at a steep sloping beach. At a water depth of 3 m, the phase coupling increases when energetic conditions are increasing to intermediate, reaches a maximum there and then decreases with further increase in energetic conditions (Figure 1.7).

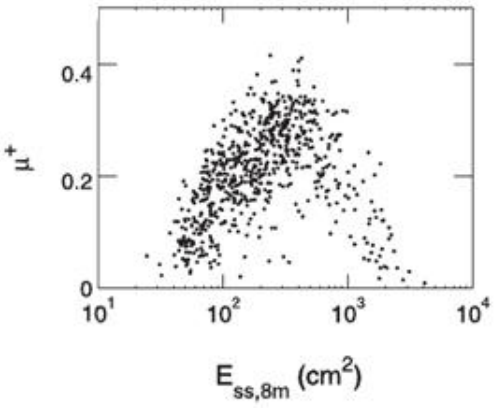

Figure 1.7: Bulk nonlinear phase coupling μ^+ versus sea-swell energy in 8 m depth $E_{ss,8m}$ at a water depth of 3 m meter. Source: Sheremet et al. [2002].

Ruessink [1998b] observed a tidal modulation in the data, which is increasingly noticeable in shallower water (Figure 1.8b), and with increasing offshore short wave energy. However, under high energy, breaking wave conditions the tidal variation was not visible.

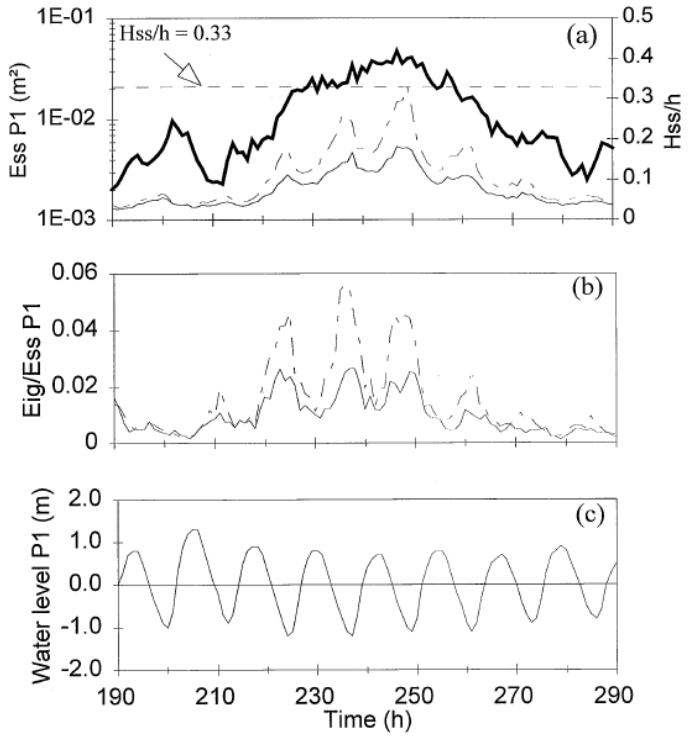

Figure 1.8: Time series of: (a) offshore short-wave energy E_{ss}^{P1} (thick line) and the local relative wave height H_{ss}/h at P3 (thin line) and P6 (dotted-dashed line), (b) ratio of local infragravity to offshore short-wave energy E_{ig}/ E_{ss}^{P1} at P3 (thin line) and P6 (dotted-dashed line) and (c) water level at P1 with respect to NAP. Hour 0 is the onset of the campaign. Source: Ruessink [1998 b].

1.2.2 Spatial variations in the surf zone

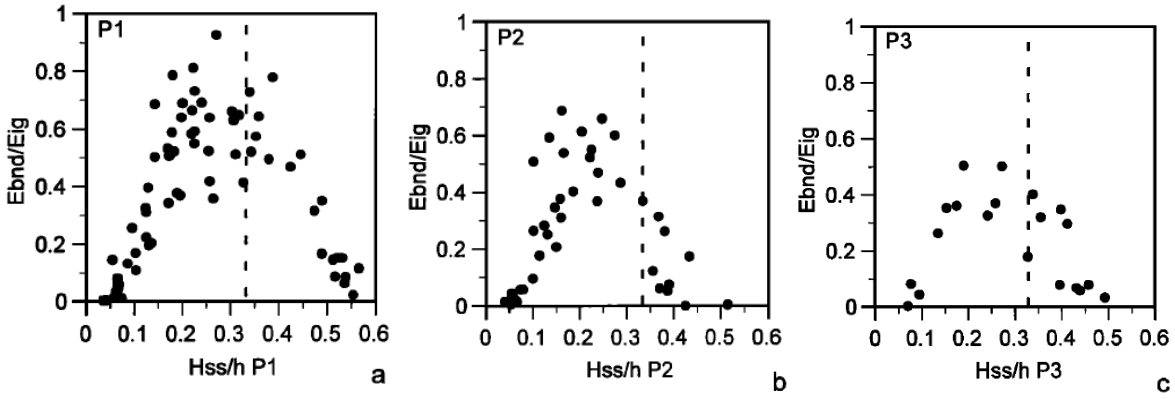

Figure 1.9: Observed ratio of bound to total infragravity energy E_{bnd}/E_{ig} as a function of relative wave height H_{ss}/h at (a) P1, (b) P2, and (c) P3. Relative location when proceeding in the seaward direction; P1, P2 and P3. The dashed vertical lines mark the onset of wave breaking (H_{ss}/h=0.33). Source: Ruessink [1998a].

From the data of *Ruessink [1998a]* that was obtained on a mild sloping beach, the cross-shore evolution of the infragravity energy is studied (Figure 1.9). It can be concluded that the ratio of bound to total energy decreases in the onshore direction (from P1 at 5 m water depth to P3 at 3.5 m water depth), which indicates that free waves are becoming more dominant.

Ruessink *[1998b]* studied the cross-shore trend of infragravity waves at a water depth of 4-10 m on a mild sloping beach. The cross-shore trend is shown in Figure 1.10 for three different energy conditions; low (open squares), intermediate (solid triangles) and high

(open circles). During low energy conditions the infragravity wave is a bit amplified in the onshore direction (Figure 1.10b). The wave field is dominated by free waves, since the correlation (r0) of low frequency waves with short wave groups is close to zero. During intermediate conditions though, bound long waves contribute significantly to the total energy. The energy is amplified up to the moment where the short waves are initiating to break (between P3 and P4), and after that decrease in the onshore direction. Moreover, the moment of breaking is coinciding with a decrease in correlation with the short wave groups. During high energy conditions infragravity energy is largest, but unlike the two previous examples, decreases in the onshore direction owing to dissipation. Except at P1, free long-wave motions dominate the total long-wave field.

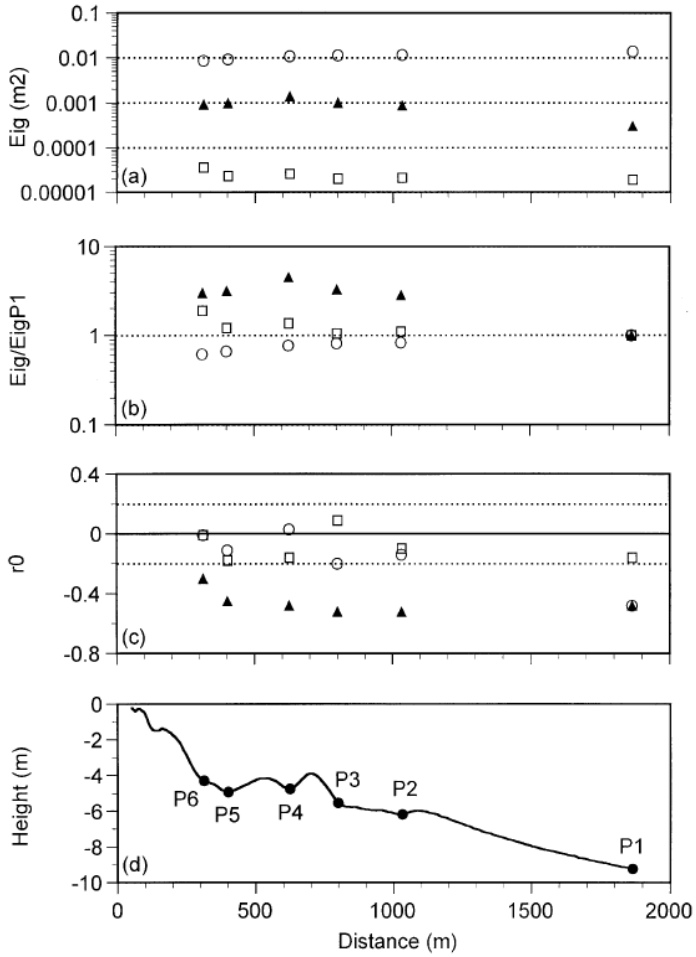

Figure 1.10: Cross-shore change in: (a) infragravity energy E_{ig}, (b) amplification E_{ig}/E_{ig}^{P1} and (c) cross-correlation coefficient at time lag 0 r_0 between the short-wave group and the total infragravity motion for three examples. The open squares, solid triangles and open circles are representative of low-energy (E_{ss}^{P1}=3.9-03 m^2), intermediate (E_{ss}^{P1}=0.19 m^2) and high-energy conditions (E_{ss}^{P1}=1.02 m^2), respectively. The horizontal dotted lines in (c) are the 95% confidence levels on r_0=0. The cross-shore profile of the measurement section is shown in (d). Source: Ruessink [1998b].

Herbers et al. [1995a] concluded that free infragravity energy dominates in deeper water on the shelf (Figure 1.11), although forced wave contributions are more significant in shallower water and can become dominant in deeper water when the conditions are very energetic.

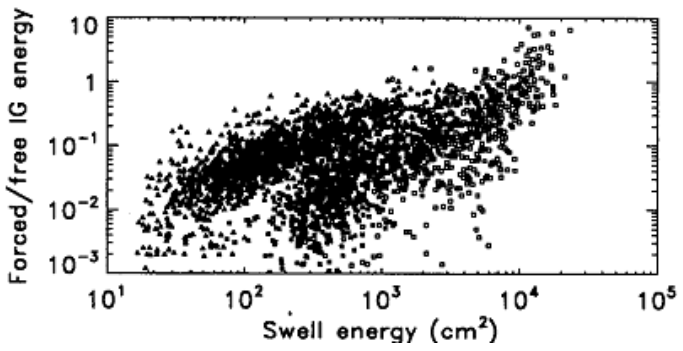

Figure 1.11: The ratio of forced to free infragravity energy versus swell energy. The data are from 8 m depth at Duck (triangles), 30 m at Ventura (asterisks), and 204 m at Harvest Platform (squares). Source: [Herbers et al., 1995a].

Ruessink [1998b] concluded from other field data, at a water depth varying from 4 to 10 m at a mild-sloping beach, that the low frequency energy was more or less linearly related with the offshore short wave energy (Figure 1.12). This indicates that free waves are dominating also at these water depths.

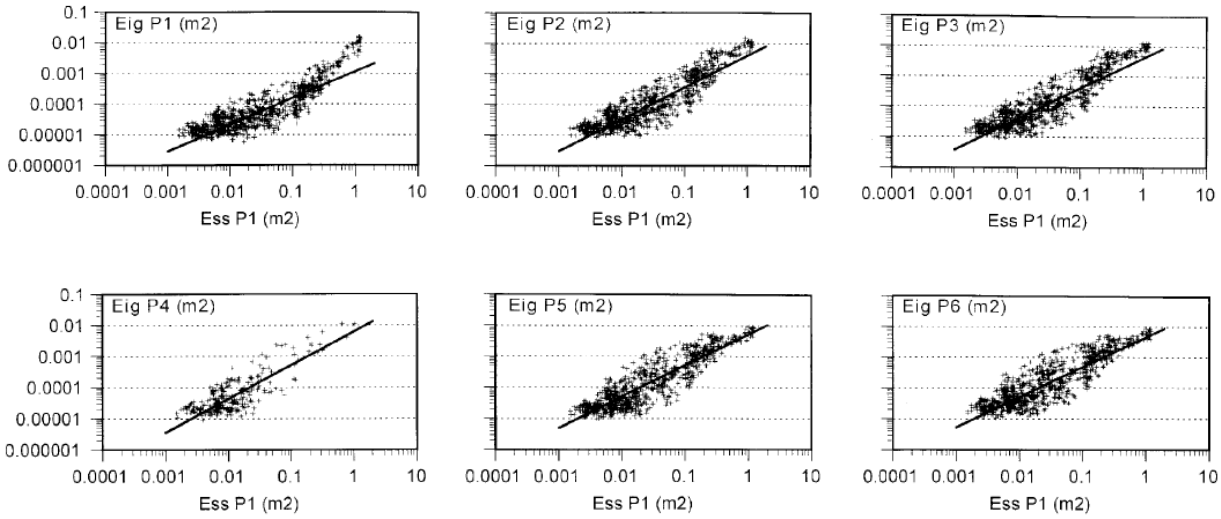

Figure 1.12: Infragravity energy E_{ig} as a function of offshore short wave energy E_{ss}^{P1} (0.04-0.33 Hz). Relative location when proceeding in the seaward direction; P6 to P1. The straight lines are the least squares fits through the logarithms of the data. The corresponding coefficients are P1: 0.87, P2: 1.04 , P3: 1.02, P4: 1.08, P5: 1.01 and P6: 0.98. Source: Ruessink [1998b].

1.2.3 Swash zone

The swash zone is the boundary between the inner surf zone and the sub aerial beach processes. The run-up (the location of the water line on the beach) is determined by the set-up and fluctuations around the set-up level, called swash. The wave run-up is typically parameterized by:

$$\frac{R}{H_s} = c\,\xi_0, \qquad (1)$$

where R is the significant run-up height, H_s is the deep water significant wave height, c is a dimensionless constant and ξ_0 is the Iribarren number. It is a non-dimensional surf similarity parameter that is useful in parameterizing a number of surf zone processes, and is defined as:

$$\xi_0 = \frac{\tan\beta}{(H_s / L_0)^{1/2}}, \qquad (2)$$

where β is the beach slope, L_0 is the deep water wave length ($L_0=gT^2/2\pi$), g is the gravitational acceleration and T is the peak incident wave period. High Iribarren numbers indicate reflective beaches, whereas low numbers indicate dissipative beaches. Field research of run-up dynamics have mainly taken place on intermediate to reflective beaches. In this literature review, more attention is paid to the few field cases concerning low-sloping beaches.

Guza and Thornton [1982] performed research at a low energy, mildly dissipative beach, with an Iribarren number in between 0.3 and 1.4. With energetic high frequency waves, a large fraction of the total swash is at surf beat periods. Figure 1.13 shows the swash spectra. There is visible that the high frequency part is approximated by f^{-3} (where f stands for frequency). When incident wave energy increases, the run-up spectra are saturated at high frequencies, whereas low frequencies are not and increase in energy.

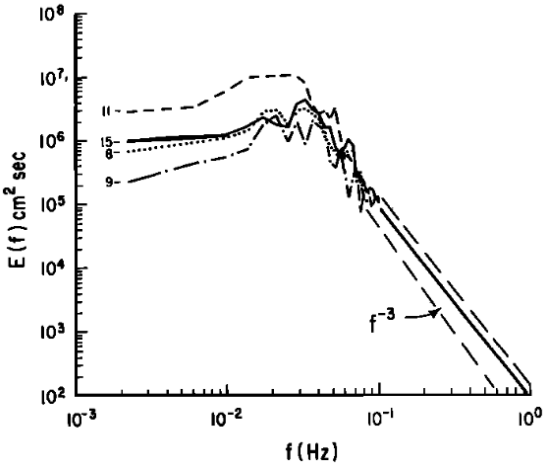

Figure 1.13: High resolution November swash spectra. Run numbers identify each spectra, wherein 8 represents a significant wave height (H_s) of 1.02 m, 9: H_s=0.60 m, 11: H_s=1.36 m and 15: H_s=1.11 m. There are between 8 and 30 degrees of freedom. Source: Guza and Thornton, [1982].

The variances of each frequency range (high or low), calculated by summing over the required frequency band for each day, are converted to significant swash excursions. These are plotted against significant incident wave height (H_s) in Figure 1.14. It can be seen that the high frequency energy levels are more or less constant, and do not increase when significant incident wave height increases. On the contrary, the low frequency energy increases significantly.

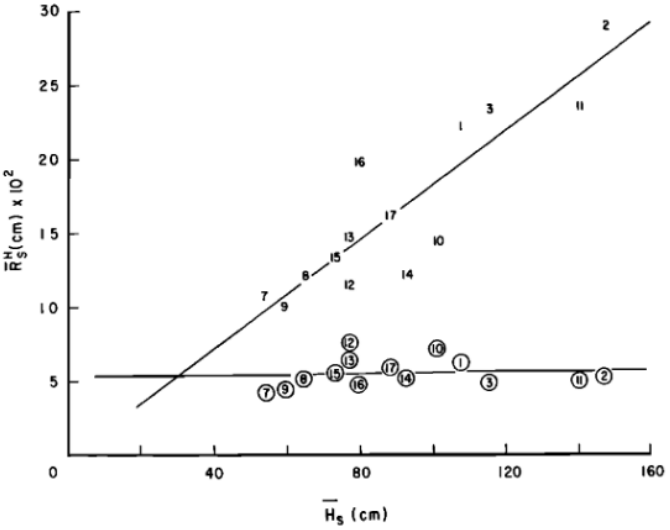

Figure 1.14: Significant swash excursions (R_s^{-H}) obtained from low and high frequency swash variances versus significant incident wave height (H_s). Numbers are run identification. Uncircled and circled numbers are low (f < 0.05 Hz) and high (f>0.05 Hz) frequencies, respectively. Source: Guza and Thornton [1982].

The constant of proportionality in the linear H_0 dependence of the swash height is observed as being 0.7.

Ruessink et al. [1998] carried out a field campaign under highly dissipative conditions (ξ_0 <0.35) on a low-sloping beach and observed that infragravity motions are dominating the swash (R_{ig}/R=0.85). They observed furthermore that the saturation of the sea-swell frequencies (again with a f^{-3} relation) during run-up extended into the infragravity wave band. In Figure 1.15 it can be seen that only the spectrum with the lowest frequencies (0.004≤f≤0.018 Hz) increased more or less linearly with increasing offshore wave height, the middle (0.018<f≤0.033 Hz) and higher (0.033<f≤0.05 Hz) frequency band did not increase much and reached a maximum around respectively H_0=3 m and H_0=2m. This implies saturation of these two higher low frequency bands, and hence breaking of infragravity waves. This long wave breaking is further discussed in chapter 2.

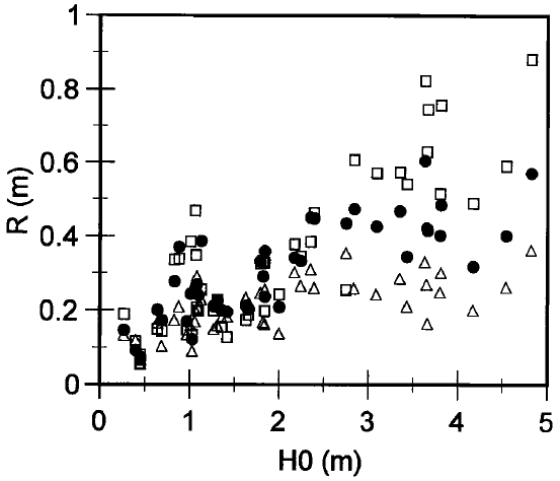

Figure 1.15: Observed swash height R for frequency bands 0.004≤f≤0.018 Hz (open squares), 0.018<f≤0.033 Hz (solid circles) and 0.033<f≤0.05 Hz (open triangles) versus offshore wave height H_0. Source: Ruessink et al., [1998c].

Ruessink et al. [1998] observed a proportionality constant of H_0 with the swash height of only 0.18. This would imply a dependence on the Iribarren number for the R_{ig}/H_0 ratio, since *Guza and Thornton [1982]* for higher Iribarren numbers observed a much larger constant. They ascribe this difference to the saturation of the higher infragravity frequencies for situations with ξ_0 less than 0.3.

Ruggiero et al. [2004] also observed that almost the entire run-up variance occurred in the infragravity band. It was a more dissipative beach site than that of *Ruessink et al. [1998c]* since the ratio of R_{ig}/R was in this case 0.98, in respect to 0.85 observed by *Ruessink et al. [1998]*.
There is a sharp roll off in energy of the saturated region, which is proportional to f^{-4} (Figure 1.16), opposing the values observed by *Ruessink et al. [1998c]* and *Guza and Thornton [1982]* of f^{-3}.

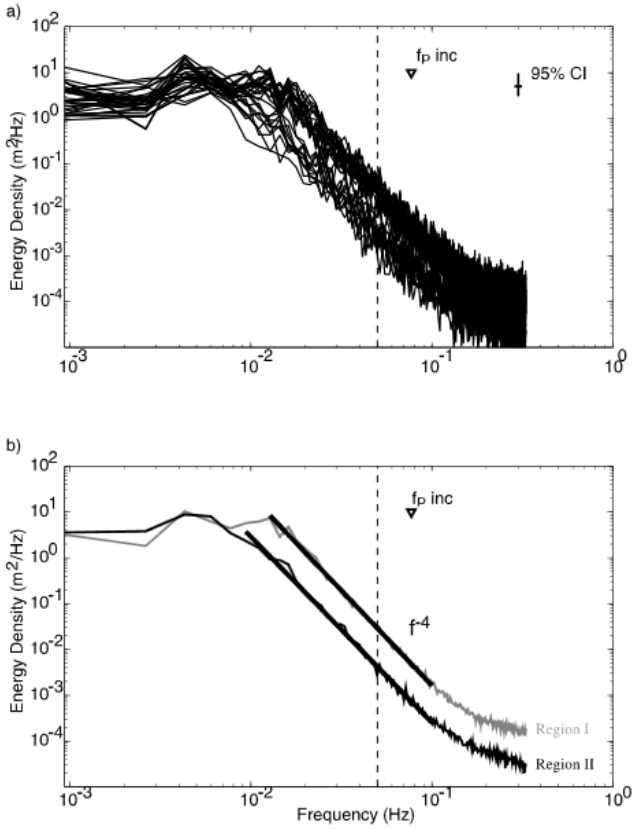

Figure 1.16: (a) Observed run-up energy density spectra from all 33 transects and (b) average energy density spectra from region I (top shaded line) and from region II (bottom solid line). The triangles indicate the peak frequency of the deep water waves, and the vertical dashed lines at 0.05 Hz indicate the division between the infragravity and the sea swell frequency bands. The solid lines through the spectra within the saturated bands are the best fits to the estimates in log-log space. Source: Ruggiero et al. [2004].

In the Figure above there can be seen that the saturated zone extends far into the infragravity wave band. The lowest saturated frequency is 0.0043 Hz to 0.0161 Hz. There can be seen that the saturation extends a bit further into region II, this region has the lower beach slopes.

They observe a constant in proportionality of H_0 with the swash height of 0.33, which is twice as large as the 0.18 found by *Ruessink et al. [1998c]*, but is much smaller than the 0.7, which was observed by *Guza and Thornton [1982]*.

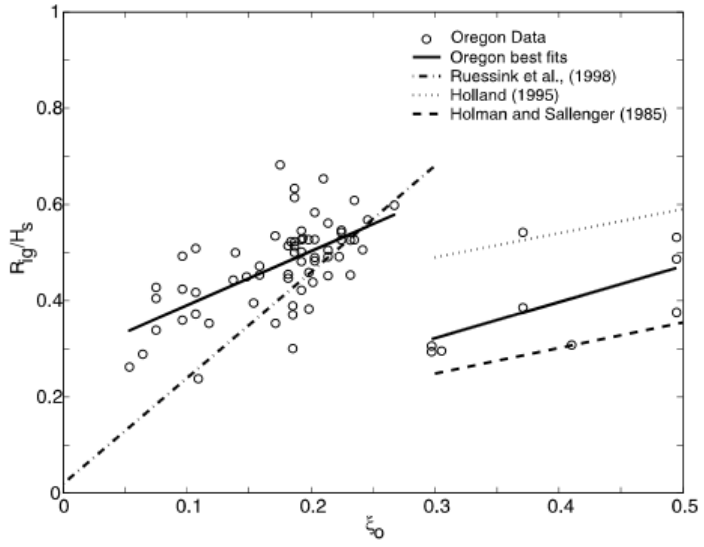

Figure 1.17: Normalized significant infragravity run-up elevation versus Iribarren number. The circles represent all of the Oregon run-up data and the solid lines are the linear relationships for $\xi_0<0.3$, $R_{ig}/H_s=1.12\xi_0 + 0.28$, r=0.62 and for $\xi_0>0.3$, $R_{ig}/H_s=0.75\ \xi_0 + 0.01$, r=0.62. Also shown are the relationships of Ruessink et al. [1998], $R_{ig}/H_s=2.20\ \xi_0+0.02$ (dash-dotted line), Holland [1995], $R_{ig}/H_s=0.5\ \xi_0+0.34$ (dotted line) and Holman and Sallenger [1985], $R_{ig}/H_s=0.53\ \xi_0+0.09$ (dashed line). Source: Ruggiero et al. [2004].

Similar to the results of *Ruessink et al. [1998c]*, the slope (Figure 1.17) of the regression is steeper for smaller Iribarren numbers than for numbers larger than 0.3. However, the slope of *Ruggiero et al. [2004]* is twice as less compared to *Ruessink et al. [1998c]*. *Ruessink et al. [1998c]* suggest that this steeper relation can be caused by the far extent of the saturation into the infragravity frequency band, which seems to be confirmed by the data of *Ruggiero et al. [2004]*.

1.3 Reflection

1.3.1 Seaward and shoreward propagating components

Shoreward propagating low frequency waves reflect at the shoreline and propagate then in the seaward direction. Reflection coefficients <1 (>1) imply an energy sink (source) between the shoreline and the observations sites.

Elgar et al. [1994] analyzed data measured at 13 m water depth, 2 km offshore. In contrast with sea-swell energy, infragravity energy reflection was often found to be larger than one. It increased from 0.5-1 during low energy conditions, to 1-3 during high energy conditions (Figure 1.18).

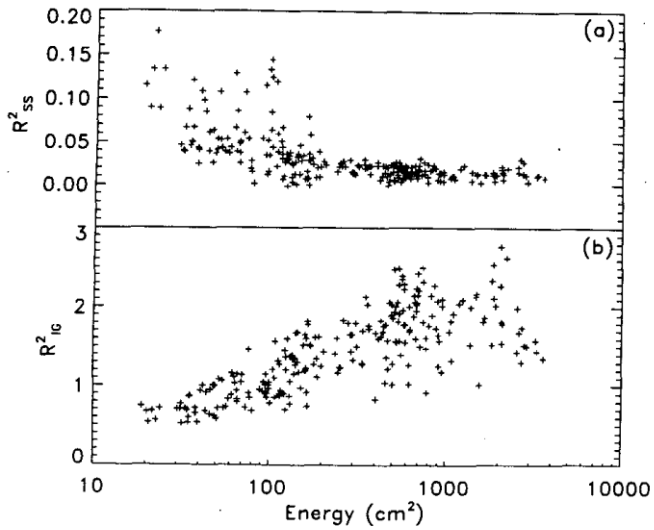

Figure 1.18: Ratio of seaward to shoreward propagating energy vs energy in the swell-sea frequency band. (a) Swell-sea (R^2_{ss}) and (b) infragravity (R^2_{ig}) frequency bands. Source: Elgar et al. [1994].

There has to be noted that since the array was positioned far from the shoreline, the processes that are occurring in the zone between, must be considered to explain the observed infragravity wave reflections. A likely explanation is that infragravity energy is generated shoreward of the array and radiates seaward after reflection, unlike sea-swell energy which is mostly generated seaward of the array and dissipates in the surf zone *[Elgar et al. 1994]*. Thus the surf zone is a source of infragravity energy and hence $R^2>1$.

Observations of *Herbers et al. [1995b]* confirm that the net energy flux can be directed seaward (reflection > 1) or shoreward (reflection < 1), and present values in the range

of 0.5 - 4.0 (Figure 1.19). Note the drop to <1 at very large E_{ss} which indicates dissipation of infragravity energy. This implies that the surf zone is a sink, which is consistent with Figure 10 at high energetic conditions.

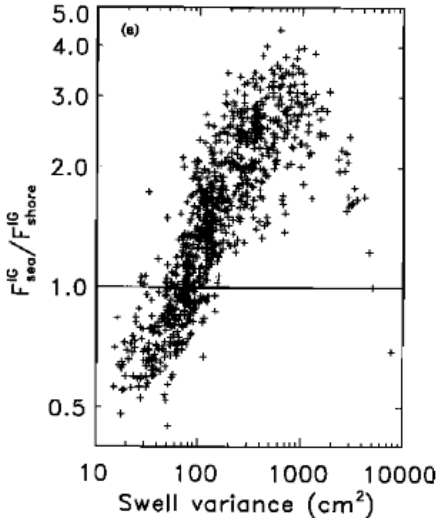

Figure 1.19: (a) The ratio $F^{IG}_{sea}/F^{IG}_{shore}$ of the seaward to the shoreward component of the cross-shore energy flux in the infragravity frequency band versus the swell variance. Source: Herbers et al. [1995b].

Sheremet et al. [2002] performed field experiments in more shallow water at depths of 1 - 6 m, on a steep sloping beach. They analyzed reflection and phase coupling for two significant wave heights; H_s=2 m and H_s=1 m. They observed that in both cases reflection of low frequency waves is significant (Figures 1.20e and 1.20f), whereas sea-swell reflection is weak (Figure 1.20a and 1.20b).
The shoreward infragravity energy flux increases in the shoreward direction during shoaling (Figures 1.20c and 1.20d), where the phase coupling with the short wave groups (Figures 1.20g and 1.20h) is rather large (0.2 - 0.4). Within the surf zone the short waves are breaking, this is visible by the decrease of the shoreward energy flux (Figure 20a shoreward of ca. 385 m and Figure 20b shoreward of ca. 175 m). Within the surf zone the phase coupling decreases rapidly to zero, and also the reflected waves are not bound anymore to the short wave groups. The infragravity reflection coefficient (R^2) is calculated by dividing the local seaward energy flux by the local shoreward energy flux. Relatively seen, the reflection at H_s=1 m decreases from 1.5 seaward of the surf zone, to 0.5 at the point where the short waves start breaking, and increases again in shoreward direction where it reaches 1 close to the shoreline. The values of R^2 are less than one because bound infragravity wave energy is significant. Bound infragravity waves have a different depth dependence than free waves, which leads to a partially standing wave in the cross-shore direction. At the shallowest point R^2 is almost one, so there is almost a perfect reflection at the beach.

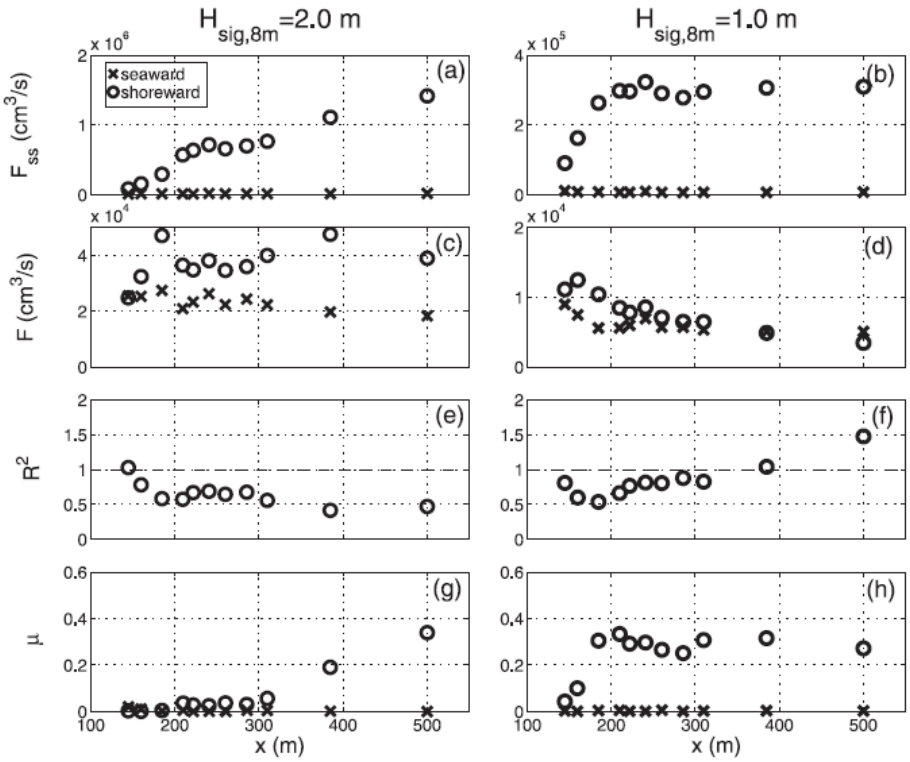

Figure 1.20: (a) and (b) Bulk seaward and shoreward sea-swell energy fluxes; (c) and (d) bulk seaward and shoreward infragravity energy fluxes; (e) and (f) bulk infragravity reflection coefficient R^2; and (g) and (h) measures of nonlinear phase coupling μ^+ versus cross-shore location x: (left) 7 November 1997, 0700-1000 EST, $H_{sig,8m}$=2.0 m and (right) 10 September 1997, 0100-0400 EST, $H_{sig,8m}$=1.0m. The μ^+ bi-phases, not shown, are close to 180°, as observed by Ruessink [1998]. Circles and crosses correspond to shoreward and seaward infragravity wave propagation, respectively. Note the different vertical scales for fluxes in the left and right panels. Source: Sheremet et al. [2002].

Battjes et al. [2004] concluded from laboratory experiments that the growth rate of the incoming lf waves increases significantly with frequency (Figure 1.21), being of the order of Green's law ($H \sim h^{-1/4}$) for the lower frequencies and comparable to the shallow-water limit ($H \sim h^{-5/2}$) of *Longuet-Higgins and Stewart [1962]* equilibrium solution for the highest of the (subharmonic) frequencies. This implies a frequency-dependent effectiveness of the transfer of energy between high frequency and low frequency waves.

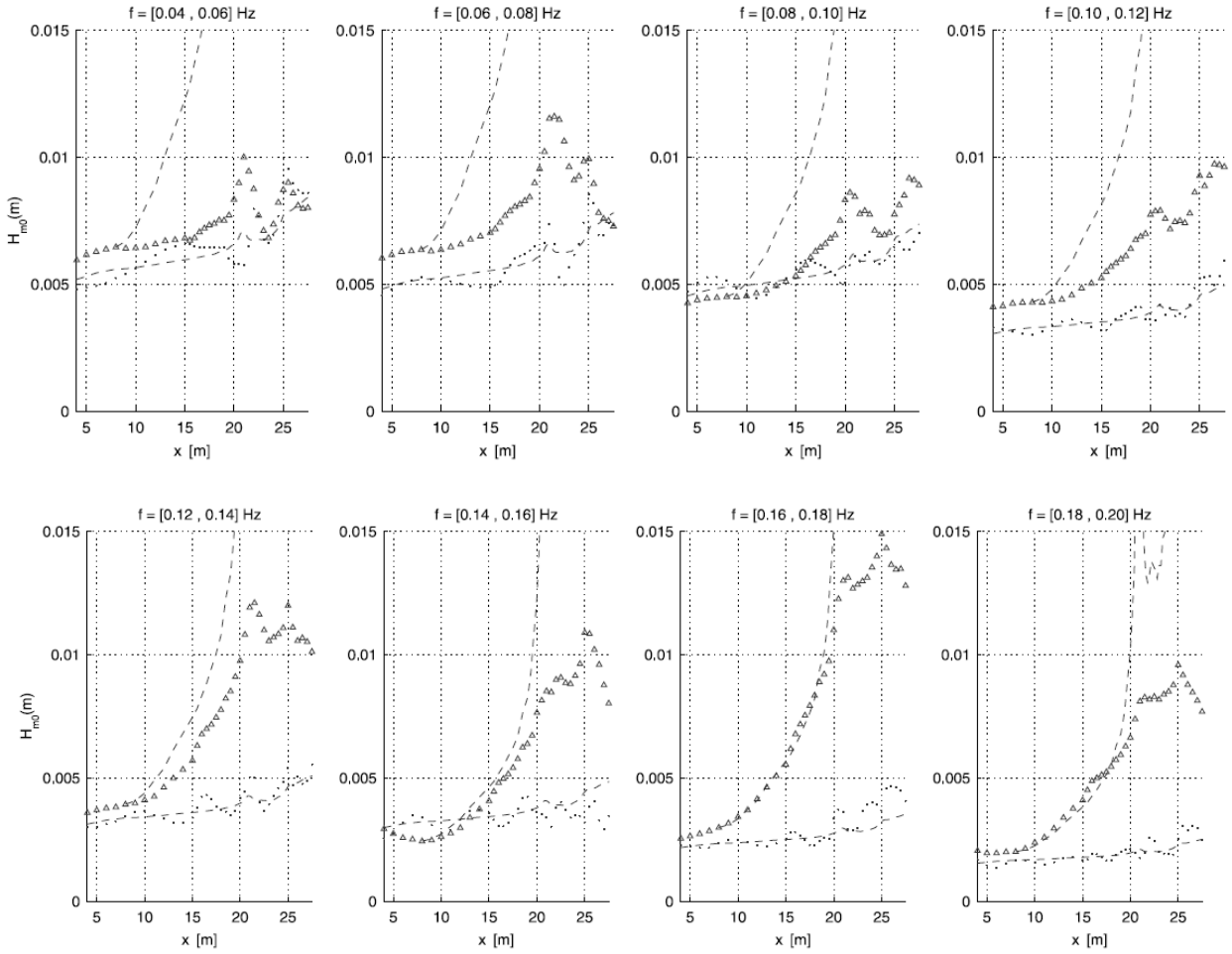

Figure 1.21: H_{m0} values of incoming (triangles) and outgoing (dots) low frequency waves for different frequency bands. Lower dashed curve: Green's Law ($H \sim h^{-1.4}$), fitted to outgoing wave heights in the zone offshore from x=20m; upper dashed curve: LHS62 asymptote ($H \sim h^{-5/2}$), initiated with wave height at x=8 m. Source: Battjes et al. [2004].

Furthermore, also a significant decrease in height of the outgoing waves relative to the incoming waves is observed. This implies a significant dissipation of incoming wave energy (90%) in the narrow zone between the most inshore stationed instrument and the shoreline. Also in this process frequency dependence is noted; with a higher frequency of the low frequency waves there is more dissipation, as the outgoing waves are smaller compared to lower low frequencies. Thus, the dissipation state of low frequency waves is not only determined by the spatial location as discussed earlier in this chapter, but also by the frequency of the wave itself.

This increase in dissipation with increasing frequency is visible in several numerical model results of other researchers. It could be due to numerical errors, but those researchers also point out that the higher frequency subharmonic waves are less separated in frequency from the harmonic waves than lower frequency components. Therefore they

could be more affected by the breaking of the harmonic, short waves. However, the dissipation could also be induced by the breaking of the low frequency waves themselves.

1.3.2 Beta parameter

Battjes et al. [2004] determined a bed slope parameter governing the amount of reflection of infragravity waves. It is well known that a given bed slope appears steeper, in a manner of speaking to longer (low frequency) waves, than it does to shorter (high frequency) waves, because the former experience a greater change in depth within a wavelength than the latter. This leads to the dimensionless parameter, the normalized bed slope, expressing the relative depth change per wave length.
It can be written as $h_x/\kappa h$, in which h and h_x are characteristic values of depth and bed slope in the (sub)region considered and $\kappa=\omega/c_g$ is the wavenumber, where $\omega=2\pi f$. Approximating c_g as $\sqrt{(gh)}$, they obtain the following dimensionless parameter (β) representing the normalized bed slope:

$$\beta = \frac{h_x}{\omega}\sqrt{\frac{g}{h}}, \qquad (3)$$

the characteristic value of *h* depends on the region and the process considered; it will be specified in each particular case. While for large values of β long waves are nearly fully reflected from the shoreline, for small values of β (β_s<0.06, mild-slope regime) reflections at the shoreline are small.

The conventional criterion used to distinguish breaking and non-breaking short waves on a slope also applies to low-frequency waves near the shoreline, therefore can be assumed that the observed energy losses are due to breaking of the long waves.
The steep-slope regime and mild-slope regime are separated by a transition value $\xi\approx2.5$, implying that $\beta\approx1$ (wherein the water depth is replaced by the incident wave height). This is applied to the region near the waterline. The slope is there 1:25, combined with a incident low frequency wave height of 0.025 m and a critical value of $[\beta_{Hif}]\approx1$, this gives a transition frequency of about 0.12 Hz. When Figure 1.21 is re-examined, it shows that there is indeed a transition at this frequency between almost full reflection at lower frequencies, and strong dissipation at higher frequencies. However, there is no direct evidence for the breaking of low-frequency waves in the data.

The mechanisms that could be responsible for this energy loss in the nearshore zone are discussed in more detail in the next chapter.

1.4 Conclusions

The bound infragravity wave reaches its maximum energy just before the onset of short wave breaking, with more energetic conditions it diminishes and the phase coupling with the short wave envelope decreases. The free infragravity energy is dominant at low and high energy conditions. During intermediate and high energy conditions the infragravity energy is decreasing in the surf zone in the onshore direction, which implies energy dissipation. On low-sloping beaches, infragravity wave motions dominate the swash. With increasing energy conditions, the saturation that is present in the high frequency wave band extents into the low frequency wave band. This would be specific for Iribarren numbers lower than 0.3.

The energy dissipation is clearly visible when incident and outgoing waves are compared; the outgoing waves are much smaller in wave height. There is frequency dependence visible, higher low frequencies are more sensitive to energy dissipation. The bed slope parameter may be useful to estimate the amount of reflection.

2. Dissipation

In chapter 1 is concluded that energy losses at infragravity frequencies can be significant in the nearshore zone. This contrasts with the common view that infragravity waves reflect perfectly from a beach (R^2=1) and form a cross-shore standing pattern. This energy loss can be examined from the energy balance equation, which contains the (most) relevant physical processes (dissipation, non-linear interaction and reflection). The possible mechanisms for this energy loss are discussed in the first part of this chapter, after which the introduction of a rather simple energy balance will be given.

2.1 Dissipation mechanisms

2.1.1 Bottom friction

According to *Henderson and Bowen [2002]* the large energy dissipation of infragravity waves in the surf zone can be due to bottom friction. They analyzed data that was collected on a steep beach and came up with a standard bottom stress parameterization which follows the observed dissipation (D) rather well,

$$D(\omega) = f_e |u| \left| \langle u \rangle_\omega \right|^2, \tag{4}$$

where ω is the specific wave frequency, u is the velocity and f_e is a dimensionless energy dissipation factor. Observed values of f_e are usually in the order of 0.01-1.

In Figure 22 the onshore surf beat energy flux (q_x) is plotted against the water elevation, which is decomposed into $\overline{\eta^2}^{1/2}\overline{\eta_{sb}^2}$ where η is the surface elevation above still water level and $\overline{\eta_{sb}^2}$ is the sea surface variance due to the progression of the infragravity wave. A line was fitted through the data points, and the slope of this line is inserted in an equation to estimate the energy dissipation factor f_e

$$f_e \approx \frac{\beta}{(g/h)^{3/2} l}, \tag{5}$$

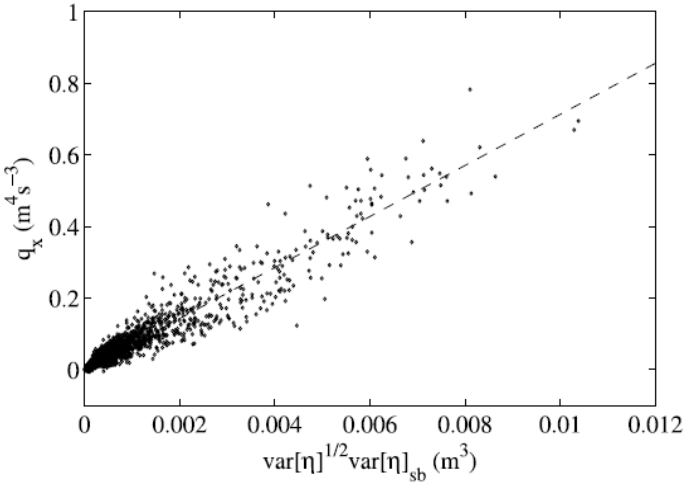

Figure 2.1: onshore surf beat energy flux q_x, versus $\overline{\eta^2}^{1/2}\overline{\eta^2_{sb}}$ at frame 1. Dashed line is $q_x = \beta\overline{\eta^2}^{1/2}\overline{\eta^2_{sb}}$, with β chosen to give least squares fit. Each data point is estimated from a half-hour time series segment. Source: Henderson and Bowen, [2002].

where *l* is the distance from the frame to the shore, β is the slope of the dashed line in Figure 2.1, and *h* is the specific water depth shoreward of the frame (taken as half the water depth at the frame). From this estimate follows a value for f_e of 0.08.
However, later research by *Henderson et al. [2006]* showed that with small drag coefficients ($<10^{-2}$) dissipation is too weak to affect the energy balance, whereas with larger drag coefficients (as the value of 0.08 found by *Henderson and Bowen [2002]*) the correlation of the energy balance with the data becomes weak. The high value of 0.08 can be due to the neglect of the nonlinear energy component in the calculation. With a nonlinear energy transfer from infragravity frequencies to higher frequencies, this would imply more energy dissipation and therefore lower f_e values.

2.1.2 Interaction with the swell field

Henderson et al. [2006] and *Thomson et al. [2006]* stated that bottom friction is not responsible for the low frequency energy dissipation. However, they did not assign it to possible breaking of the low frequency waves (as *Van Dongeren et al. [2007]* and *Battjes et al. [2004]*) as will be discussed in section 2.1.3, but to the energy transfer to higher frequency sea and swell waves.
According to them it would be unlikely for infragravity waves to break under circumstances where higher frequency waves do not break. However, in these non-breaking zones, they did record a significant loss in infragravity energy. Although dissipation due to breaking could still be present shoreward of their most inner sensor (in <0.5 m water depth) and during higher energy conditions, in their opinion interaction with short waves seems more likely.
A pair of sea-swell waves with frequencies *f1* and *f-f1* produces a longer fluctuation, *f*, the infragravity wave. The total radiation stress fluctuation (*f*) is produced by several pairs of higher frequency waves, with variable frequencies.
Henderson et al. [2006] concluded that the total nonlinear energy transfer to low frequency waves [0.005-0.05 Hz] was mostly negative (from long waves to short waves) near the shore and positive (from short waves to long waves) near the bar. During examined periods with low shear wave conditions (during moderate and low energy conditions) infragravity energy flux gradients balanced nonlinear energy transfers, implying that the nonlinear interactions between long and short waves are important. This is discussed further in section 2.3.
The most rapid nonlinear energy gain and loss are shown respectively in Figure 2.2a and b. They resulted from interactions of two short waves (at swell frequency) and one infragravity wave. The most rapid gain of energy was observed further offshore at a

water depth of around 2 m, whereas the most rapid energy loss was present close to the shore at a water depth of around 1 m.

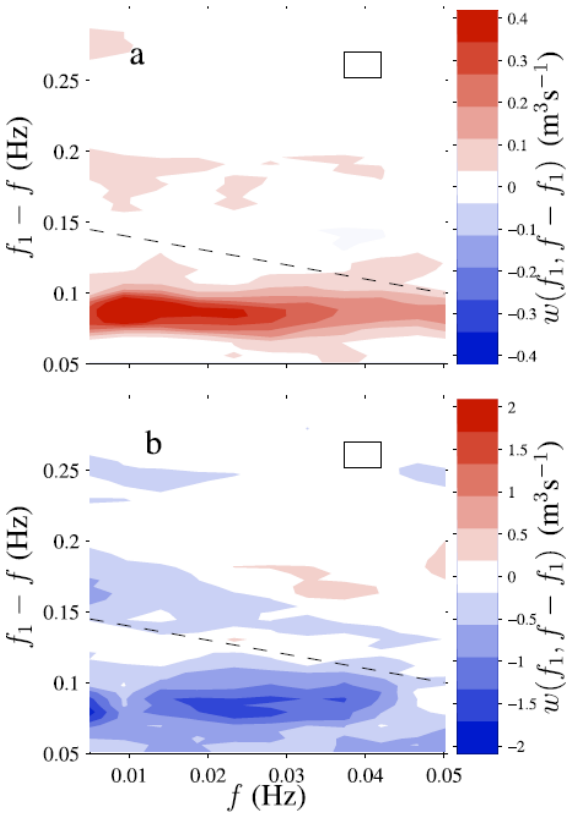

Figure 2.2: Nonlinear working with $w(f_1,f\text{-}f_1)$ on frequency f motion by triads with frequencies $(f,f_1,f\text{-}f_1)$. (a) 27 September (1000–1300), averaged between cross-shore locations 90 and 110 m. (b) 13 September (1000–1300), averaged between cross-shore locations 4 and 14 m. Rectangles indicate the size of regions over which bispectra were smoothed to estimate w(f1, f _ f1). Below the dashed lines (which mark f1 = 0.15 Hz), triads consist of one infragravity and two swell (0.05–0.15 Hz) waves. Source: Henderson et al. [2006].

Thomson et al. [2006] also point to triad interactions as mechanism for the energy dissipation. Furthermore, from observations and numerical model simulations, they observed tidal fluctuations in the nonlinear energy transfer to and from low frequencies in the surf zone (Figure 2.3). They found that the energy loss of low frequency waves is more pronounced during the low tide when the beach profile is convex, than during high tide when the beach profile is concave.

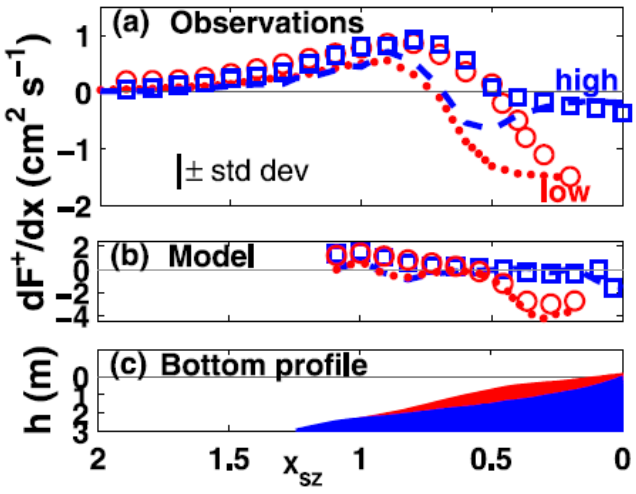

Figure 2.3: Shoreward infragravity frequency energy flux gradients dFþ/dx from (a) observations and (b) numerical model simulations, and (c) water depth at low (red) and high (blue) tide versus normalized surf zone location (xsz). The energy flux gradients dFþ/dx are estimated from differences in the flux (F+, equation (1)) between neighboring locations (red-dotted curves are low tide, blue-dashed curves are high tide) and from nonlinear transfers (equation (2)) at each location (red circles are low tide, blue squares are high tide). Source: Thomson et al. [2006].

2.1.3 Breaking of the infragravity wave

Contradicting the results of *Henderson and Bowen [2002]*, *Van Dongeren et al. [2007]* conclude from laboratory experiments that bottom friction is not the mechanism accounting for the large amount of energy dissipation at the shoreline. When plotting the dissipation components of breaking (D_{br}) and bottom friction (D_{bot}) in graphs, with infragravity wave height as a function of the still water depth, the importance of both parameters can be shown clearly (Figure 2.4).

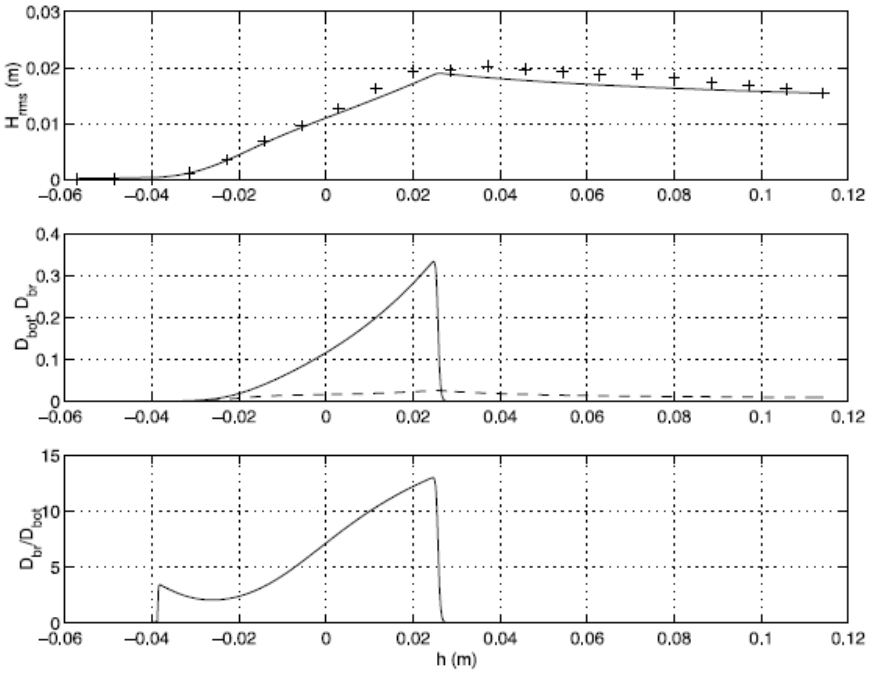

Figure 2.4: (top) Low-frequency wave heights as a function of still water depth (solid line shows the energy model; pluses are measurements). The dry beach is to the left. (middle) Dissipation due to breaking (solid line) and due to bottom friction (dashed line). (bottom) Local ratio of the two local dissipation rates. Source: Van Dongeren et al. [2007].

The modeled infragravity wave height (solid line, top panel) is in good correlation with the data (plusses) and shows the energy decay when the waves are approaching the shore. It can be seen that a sudden decay due to breaking is dominating, rather than the smaller overall present bottom friction. The lowest panel shows the relative importance of the two dissipation components, it is clear that dissipation due to breaking is at a certain location up to 12 times higher than dissipation due to bottom friction.

However, field evidence of long wave breaking is scarce. As is discussed in chapter 1, *Ruessink et al. [1998]* and *Ruggiero et al. [2004]*, who studied the swash zone have found saturation in the high frequency band to extent into the low frequency band. This implies long wave breaking.

Instead of assigning the infragravity wave energy loss to interaction with the swell field, *Van Dongeren et al. [2007]* consider the interaction with the long waves itself. These interactions would result in a steepening of the wave front and in the end in the breaking of the wave. This process is illustrated by frequency spectra (Figure 2.5) of the wave propagation in a flume with a mild slope (1:35).

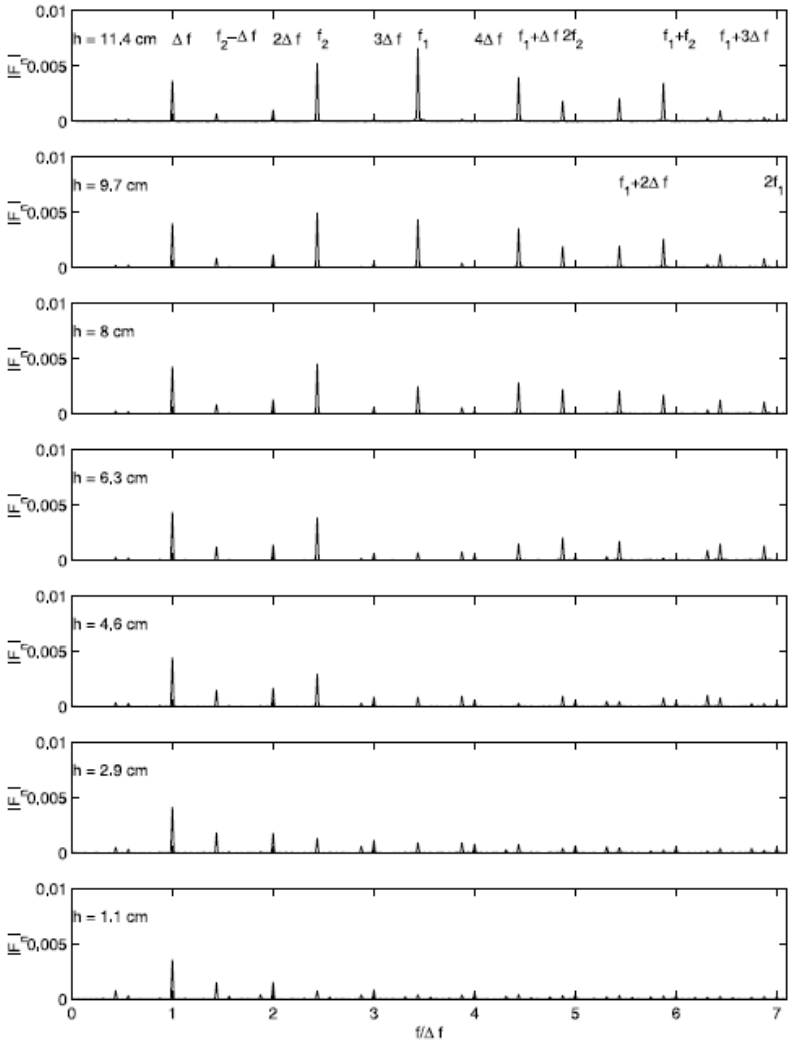

Figure 2.5: Frequency spectra of case A-1 at various depths. The most important frequency components are indicated in the first and second panels. The frequency spectra axis is normalized by Δf=0.1953 Hz. Source: Van Dongeren et al. [2007].

The spectra show that besides the primary components *f1* and *f2* with their higher harmonics, and delta f with its multiples, there are different components present. These components are triad interactions between *Δf* and *f1*, *f2*, e.g. *f1+Δf* and *f2-Δf* (the *Thomsen et al. [2006]* method). However, these components do not seem to affect the front of the low frequency wave (and thereby do not steepen it, which would most likely lead to breaking) as they affect the leeside. This selection procedure (to study the effect of one single frequency on the long wave shape) is not possible for field data as natural

waves are not monochromatic. However, bispectral analysis is possible, with this method the interaction of two long waves (the Δf, Δf in Figure 2.5) to 2Δf can be demonstrated. As can be seen in the frequency spectra, the primary components and their associated frequencies disappear from the field due to breaking when they are approaching shallow water. The low frequency components are then not coupled anymore to those frequencies, and interactions with the wave itself are more likely to become dominant. This indicates that the variance at multiples of the difference frequency is primary due to self-self interaction. For example, the energy at *2Δf* is mostly the result of the self-self interaction *Δf+Δf* and not by *2f1-2f2* or other difference contributions from the higher frequency field. This (Δf, Δf) to 2Δf interaction is analogous to how short waves transform in shape while breaking.

In order to check these results *Van Dongeren et al. [2007]* performed another flume test, but now with only free infragravity waves that have the same frequency as the induced bound waves in the earlier test (Figure 2.6).

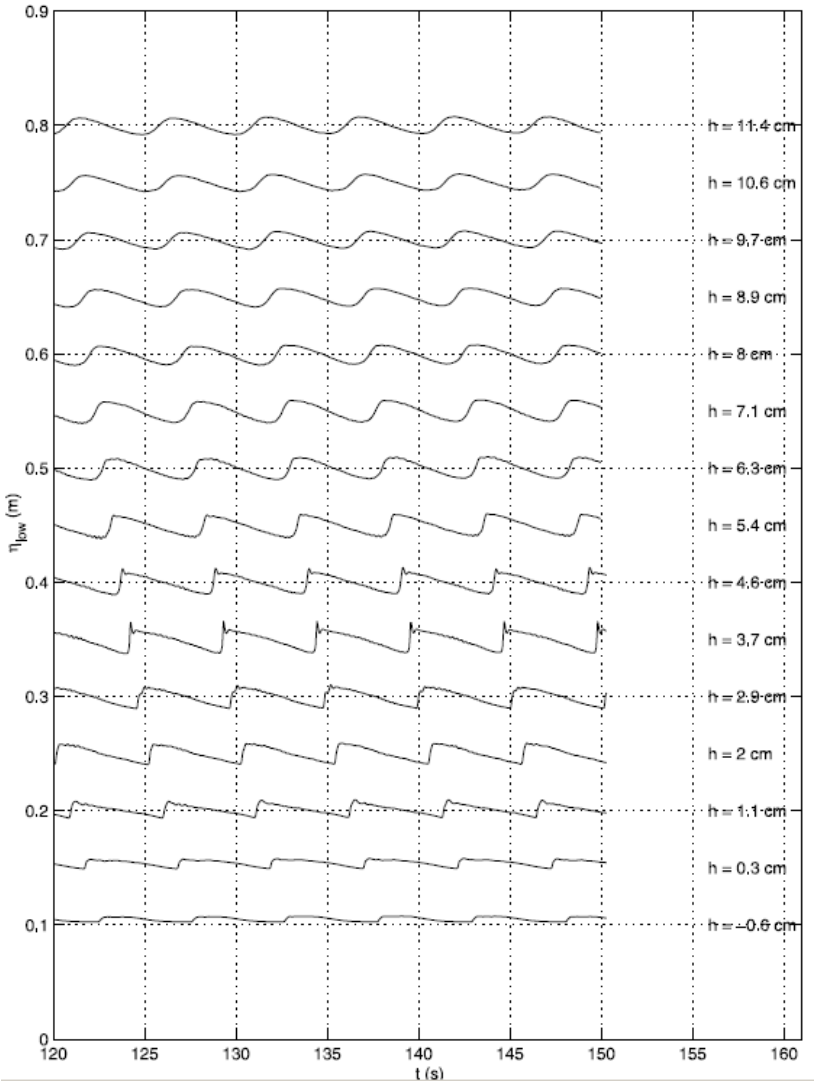

Figure 2.6: Time series of the total measured time series for consecutive gauge positions around the still water line for a free long wave with a frequency equal to the difference frequency of case A-1. Source: Van Dongeren et al. [2007].

The free waves show almost the same behavior; they steepen up and turn into turbulent bores. This leads to their conclusion that indeed self-self interactions are dominating under these low sloping conditions, and that breaking is the dominant infragravity dissipation mechanism.
Unfortunately, this mechanism cannot be verified in the field in the same way as *Van Dongeren et al. [2007]* carry out in their laboratory test. In the field there are always short waves present together with the long waves, so the behavior of the long wave cannot be studied individually, but again here bispectral analysis can be applied.

2.2 Energy balance

Several researchers have derived an energy balance specifically for infragravity waves. *Henderson and Bowen [2002]* produced a rather simple equation that is expanded by *Henderson et al. [2006]*, that is applicable also when low wave frequencies are not that much lower than short wave frequencies, which is normally the case.
The total energy flux is composed of linear and nonlinear components. The linear energy flux

$$F_L = \int_{f=0.005\,Hz}^{0.050\,Hz} hC_f(g\eta,u)\,df\,, \tag{6}$$

is the co-spectrum between the sea-surface elevation above still water level (η) times the gravitational acceleration (g), and the cross-shore velocity (u), multiplied with the water depth. The nonlinear energy flux F_N

$$F_N = \int_{f=0.005\,Hz}^{0.050\,Hz} C_f(g\eta,M)\,df + \int_{f=0.005\,Hz}^{0.050\,Hz} C_f(S_{xx},u)\,df\,, \tag{7}$$

is composed of two terms. The first term is the co-spectrum between η times g, and the sea-swell mass flux (M). The second term is the co-spectrum between the sea-swell radiation stress (S_{xx}) and u. When combining equations (6) and (7), the total energy flux F at infragravity frequency f is

$$F(f) = hC_f(g\eta,u) + C_f(g\eta,M) + C_f(S_{xx},u)\,, \tag{8}$$

with the sea-swell mass flux (M) and the sea-swell radiation stress (S_{xx}) as

$$M = \eta' u' \text{ and } S_{xx} = hu'u' + g\eta'\eta'/2\,, \tag{9}$$

where the primes (') denote the sea-swell variables (band-passed between 0.05 and 0.4 Hz). The net energy balance is

$$\frac{\partial F(f)}{\partial x} = W(f) - D(f)\,, \tag{10}$$

with the gradient of the cross-shore energy flux F(f), equal to the nonlinear transfer of energy to motions at frequency f from motions at other frequencies and D(f) is the dissipation component. Assumed is that the frequencies that are exchanging energy with the infragravity frequencies, are dominated by sea-swell frequencies [0.05-0.5 Hz].

Furthermore, the influence of mean currents and rollers, and wave reflection at the beach are not included in the equations.

For nearly shore-normal shallow water waves the nonlinear-energy transfer to motions at an infragravity frequency *f* ,

$$W(f) = C_f(S_{xx}, \partial u / \partial x), \tag{11}$$

here C_f is the co-spectrum between the sea-swell radiation stress S_{xx} and the cross-shore velocity gradient ($\partial u / \partial x$). Positive *W* values indicate energy transfers to motions at frequency f, whereas negative values indicate energy transfers from motions at frequency f. To evaluate non-linear energy transfers, the cross-shore gradient of *u* must be calculated

$$\frac{\partial u}{\partial x} = -\frac{1}{h}\left(\frac{\partial \eta}{\partial t} + u\frac{\partial h}{\partial x}\right), \tag{12}$$

where h is the water depth.

When $\frac{\partial F(f)}{\partial x} = W(f)$ there is no dissipation of energy present by e.g. bottom friction or long wave breaking (section 2.1).

The nonlinear component is often neglected in models (*Sheremet et al. [2002]; Henderson and Bowen [2002]; Thomson et al. [2006]*). *Henderson et al. [2006]* discussed in their research if this simplification of the energy balance is justifiable. They concluded that in deeper water (>2m water depth) the linear energy flux was indeed correlating with the total energy flux (r^2 = 0.74). However, in the nearshore zone (< 2m water depth) the linear and total energy flux were uncorrelated (r^2 = 0.04). Therefore they strongly recommend including the nonlinear component in models regarding the inner nearshore zone.

2.3 Applying an energy balance

Henderson and Bowen [2002] derived an equation to estimate the excess of dissipation relative to forcing of infragravity wave energy in a specific region. In this equation only the linear flux is taken into account:

$$\left[hC_{p,u}(\omega)\right]_{x=b} - \left[hC_{p,u}(\omega)\right]_{x=a} + \int_{x=a}^{b}\left(E\left[D'(\omega)\right] - E\left[N'(\omega)\right]\right)dx = 0, \tag{13}$$

where *D'(ω)* is the dissipation per unit frequency, and *N'* stands for the sum of the nonlinear terms (equal to *W(f)* from section 2.2). If the forcing mechanism is larger than the dissipation between the two locations, the outcome will be negative. With data of water pressure, mean water depth and velocity at two locations in cross-shore position it is possible to solve the equation. With this equation it is not possible to single out the

absolute amounts in energy of dissipation and forcing, but only to give the dissipation relative to forcing.

Field data of *Henderson and Bowen [2002]* in water depth of 1.5 to 3.5 m, on a steep sloping beach, indicated that the infragravity energy flux was mostly directed onshore in the nearshore zone (<3.5 m) which indicates that dissipation was dominating in this area (Figure 2.7). There has to be noted that this does not mean that the forcing mechanism was weak, but only that the dissipation was stronger than the forcing.

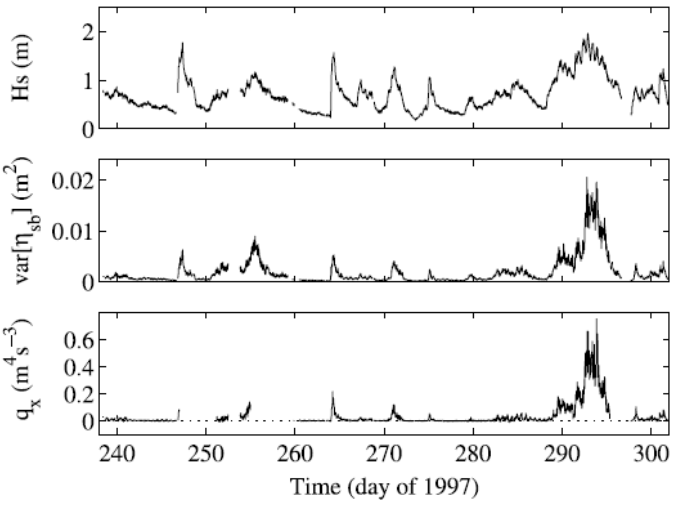

Figure 2.7: Time series of half-hourly significant wave height Hs, surf beat sea surface elevation variance, η_{sb}^2, and shoreward surf beat energy flux, q_x, during Sandyduck at most seaward frame (+/- 3.5 m water depth). Source: Henderson and Bowen [2002].

From the above mentioned equation the net forcing strength *S* can be defined:

$$S = \frac{Net\ surf\ beat\ energy\ generated\ in\ one\ beat\ period}{Total\ surf\ beat\ energy} = S \approx \frac{q_{x|_{x=b}} - q_{x|_{x=a}}}{(f)\int_{x=a}^{b} \varepsilon\, dx} \quad , \qquad (14)$$

wherein ε is the energy density which can be estimated with $\varepsilon = g\overline{\eta_{sb}^2}$ and η_{sb}^2 is the sea surface elevation variance due to the infragravity wave. If *S* is positive, the net forcing exceeds the dissipation.

When the most shoreward station (1.5 m water depth) was within the saturated surf zone (the edge is represented by vertical dashed line in Figure 2.8) the forcing was mostly dominant between the offshore station (at 3.5 m water depth) and the most shoreward station (Figure 2.8a). However, onshore of the most shoreward station dissipation was dominant, and increased in strength when the wave height increased. *Henderson and Bowen [2002]* conclude that when the energetic conditions were large, dissipation dominated in the surf zone and forcing dominated seaward of the surf zone.

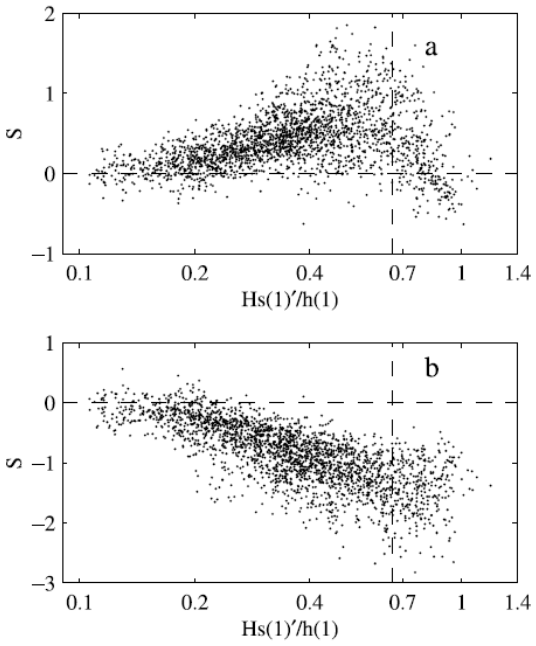

Figure 2.8: Estimated net forcing strength, S, versus shoaled significant wave height divided by the water depth, H_s'/h, at the most shoreward frame: a) net forcing strength between most inner and outer frames and b) net forcing strength onshore of the most inner frame. The vertical dashed lines indicate $H_s(1)'/h(1) = \gamma$. Each data point is estimated from a half-hour time series segment. Source: Henderson and Bowen [2002].

2.4 Conclusions

Several long wave energy dissipation mechanisms have been put forward, however there is few field data present to support any of these hypotheses. Bottom friction as a dissipation mechanism is not supported by most researchers. Long wave breaking and nonlinear interactions with short waves are at present the most likely mechanisms accounting for long wave energy dissipation.

The available data indicate that the nonlinear mechanisms may already be present under moderate energy conditions outside the surf zone. Possibly, long-wave breaking is most relevant to high-energy conditions on low-sloping beaches.

3. Sediment suspension and transport direction

Besides the dilemma of the way wherein low frequency energy is dissipated, there are also questions regarding sediment suspension and transport direction of the sediment induced by the low-frequency waves. First a definition of sediment transport will be given, subsequently the situation out- and inside of the surf zone will be discussed, with ultimately a possible explanation for the contradicting results in the literature.

3.1 Sediment transport calculations

The sediment transport rate is defined as the velocity (*u*) times the sediment concentration (*c*) present in the water column. With averaging over time the local net sediment transport rate is defined as

$$\langle uc \rangle_{net} = \frac{1}{n} \sum u \cdot c \,, \tag{15}$$

where *n* is the number of samples. A positive (negative) value indicates onshore (offshore) transport (depends on the definition of *u*). The products of velocity and concentration can be decomposed into mean (overbar) and oscillatory (tilde) components (*Osborne and Greenwood, [1992a]*):

$$c = \bar{c} + \tilde{c} \quad and \quad u = \bar{u} + \tilde{u} \,. \tag{16}$$

From (13) and (14) the local net sediment transport rate can also be given as:

$$\langle u \cdot c \rangle = \left\langle \left(\bar{u} + \tilde{u} \right) \left(\bar{c} + \tilde{c} \right) \right\rangle = \bar{u}\bar{c} + \left\langle \bar{u}\tilde{c} \right\rangle + \left\langle \bar{c}\tilde{u} \right\rangle + \left\langle \tilde{u}\tilde{c} \right\rangle . \tag{17}$$

The terms $\left\langle \bar{u}\tilde{c} \right\rangle + \left\langle \bar{c}\tilde{u} \right\rangle$ go to zero because by definition the time averaged sum of these terms is equal to zero. Consequently,

$$\langle u \cdot c \rangle = \bar{u}\bar{c} + \left\langle \tilde{u}\tilde{c} \right\rangle , \tag{18}$$

the term $\bar{u}\bar{c}$ is called the local mean sediment transport rate, and $\left\langle \tilde{u}\tilde{c} \right\rangle$ is a measure of the correlation between the oscillatory terms of velocity and sediment transport (once called flux coupling). Low values indicate a random oscillation, whereas large values indicate a large correlation in movement. The oscillatory component can be subdivided into a high (*h*) and low (*l*) frequency part, based on *Ruessink et al. [1998d]*:

$$\left\langle \tilde{u}\tilde{c} \right\rangle = \left\langle (u_h + u_l)(c_h + c_l) \right\rangle = \left\langle u_h \cdot c_h \right\rangle + \left\langle u_l \cdot c_l \right\rangle \,, \tag{19}$$

the two terms on the right hand side of the equation are respectively called the high and low frequency flux. The interactions combined of a product of high and low frequencies

are neglected, as they are relatively very small compared with the other components, because the velocity and concentration at different frequencies are uncorrelated. Equation (18) and (19) can be combined:

$$\langle u \cdot c \rangle = \overline{u}\overline{c} + \langle u_h \cdot c_h \rangle + \langle u_l \cdot c_l \rangle . \qquad (20)$$

3.2 Seaward of surf zone

Osborne and Greenwood [1992b] concluded from field experiment conducted just outside the surf zone, that under non breaking conditions, the largest sediment concentrations (although still relatively small compared to those of short waves) are present under the bound infragravity wave trough, due to the fact that the largest short waves are present at that location (Figure 3.1c and d). Those larger short waves exert larger bed shear stresses and therefore suspend more sediment than the smaller short waves. With the offshore stroke of the wave sediment is transported seaward (Figure 3.1b). With increasing energy conditions (breaking waves shoreward of measuring location) the offshore transport increased greatly, and at least equaled the transport by short waves.

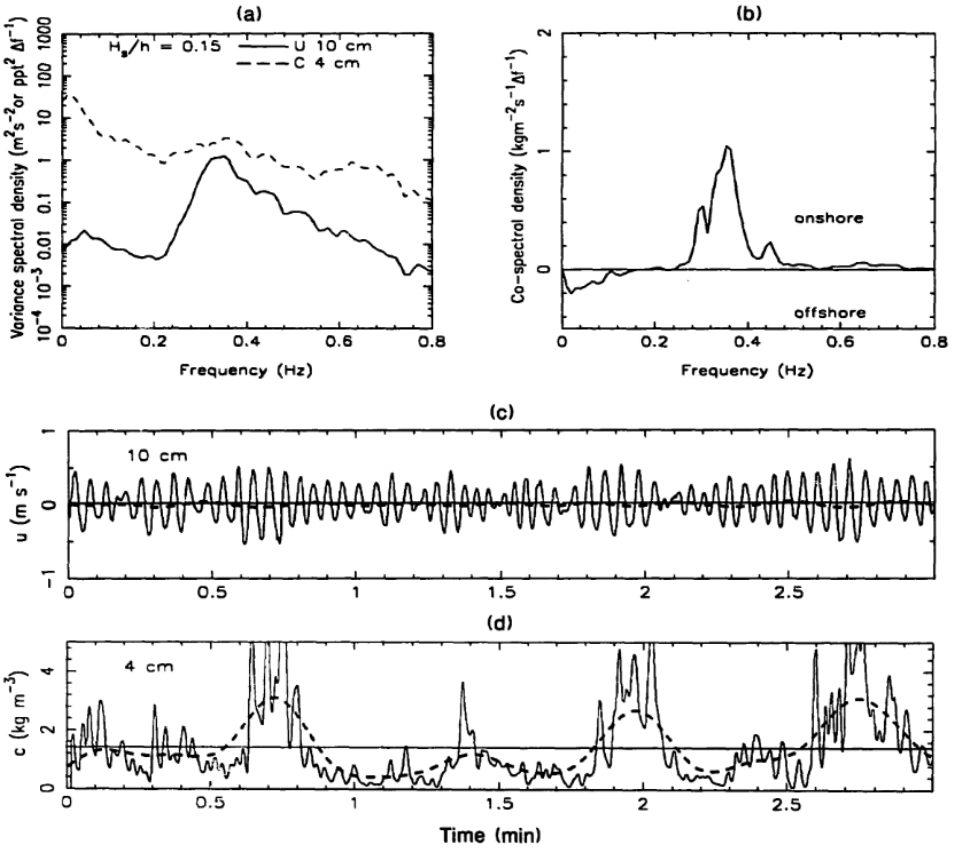

Figure 3.1: (a) Cross-shore velocity (z≈0.10 m; solid line) and suspended sediment concentration (z≈0.04 m; dashed line) spectra from the 85 m station under shoaling waves (H_s/h=0.15). (b) Co-spectrum of cross-shore velocity and sediment concentration; (c) time series of cross-shore velocity (solid line) and band-pass filtered velocity (dashed line); (d) the cross-product of velocity and suspended sediment concentration (solid line) and the band-pass filtered series (dashed line). Source: Osborne and Greenwood [1992b].

3.3 Surf zone

Beach and Sternberg [1988] concluded from field experiments in the surf zone of a low-sloping beach, that sediment is suspended under the infragravity trough. As can be seen in Figure 3.2, the first 5.5 minutes are dominated by strong low frequency (0.01 Hz) fluid motions, whereas the last part of the record is dominated by short waves (0.1-0.2 Hz) (Figure 3.2 a, b and c). Note that when velocity is stated as positive in this Figure, the transport is in the offshore direction. Suspension events for the infragravity dominated half persist for periods of 30-45 seconds and reach sediment concentrations up to 20-40 g/l which can be advected into the water column at a height of at least 26 cm above the bed (Figure 3.2 d, e, f and g). On the other hand, the suspension events of the short wave dominated part are lasting for only a couple of seconds, reach concentration maxima of 8 g/l and are advected up to 8 cm above the bed. Thus now infragravity waves stir the sediment, where outside the surf zone short waves stir.

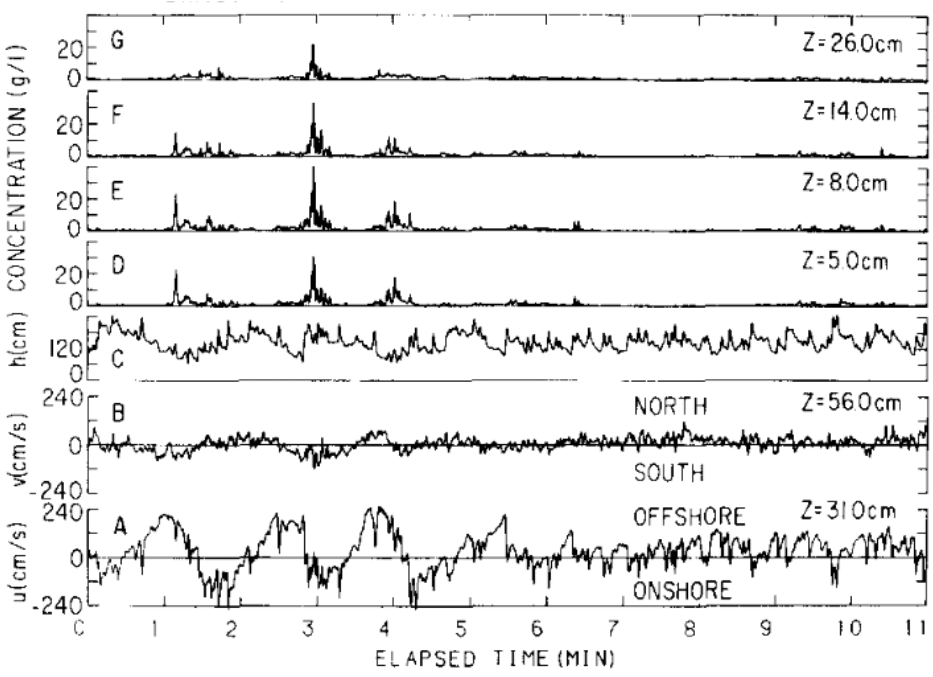

Figure 3.2: Time series as recorded at the central array. A. Cross-shore velocity, B. Longshore velocity, C. Sea level fluctuations. D-G. Suspended sediment concentration at four levels z above the bed. Source: Beach and Sternberg [1988].

Further review of the graphs tells that the sediment associated with the infragravity frequency is suspended under the wave trough, and remains in suspension during flow reversal and following onshore flow beneath the wave crest. When the onshore flow ends, sediment concentrations are low (sediment has been deposited) and the vertical sediment distribution is relatively uniform. The main transport direction of sediment is therefore onshore.

Osborne and Greenwood [1992b] confirm the fact that in the surf zone the sediment transport due to infragravity waves is onshore directed. At a more shoreward location than discussed in section 3.2 (in a bar trough) short waves are breaking, and the long wave is not bound anymore to the short wave group. During a large period of the high energetic conditions during their field campaign there was a distinctive onshore transport (Figure 3.3c).

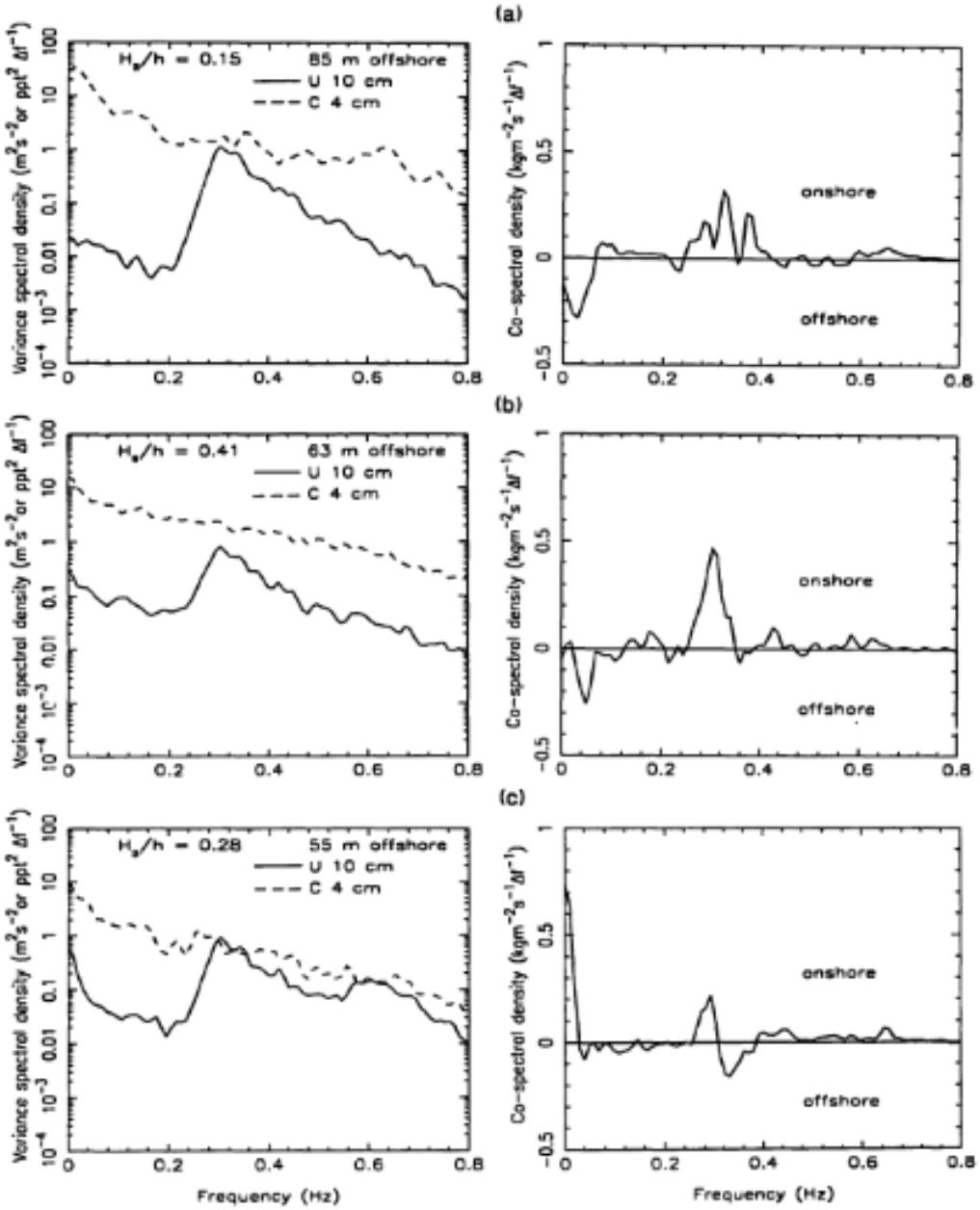

Figure 3.3: Spatial variability of cross-shore velocity (z ≈0.10 m; solid line) and sediment concentration (z ≈0.04 m; dashed line) spectra and the associated co-spectra (z ≈0.04 m; solid line) under a range of wave conditions: (a) 85 m station, H_s/h=0.15; (b) 63 m station; H_s/h=0.41; (c) 55 m station, H_s/h=0.28. Source: Osborne and Greenwood [1992b].

This is due to the combination of high sediment concentrations and the onshore phases of the long wave, which are now coinciding with the short wave height maxima instead of minima (Figure 3.4).

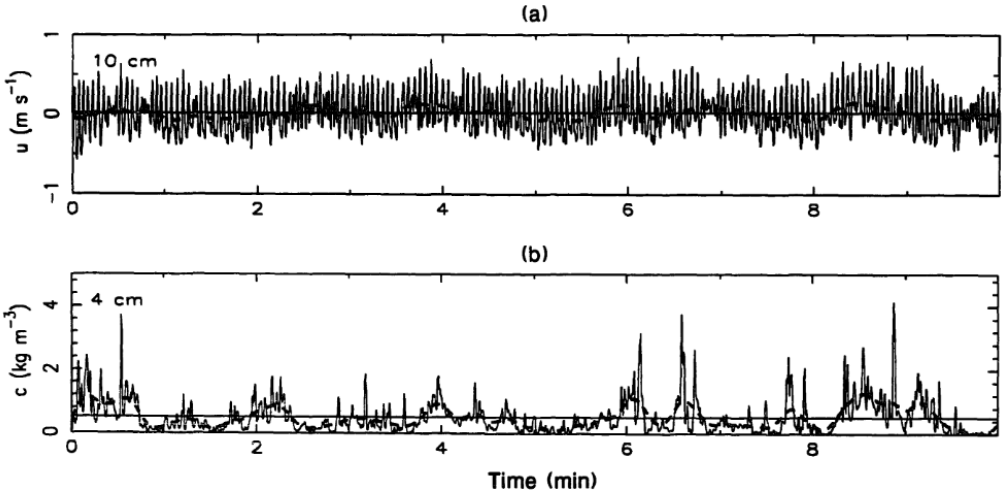

Figure 3.4: Observed (solid) and low pass filtered (dashed line) time series of cross-shore velocity (a) and suspended sediment concentration (b). Source: Osborne and Greenwood [1992b].

Van Dongeren et al. [2007] support the fact that the largest short waves are not present anymore at the long wave trough in shallow water. They observed in their lab test, that in shallow water (at h≤ 4.6 cm in Figure 3.5) the long wave is not bound anymore to short wave groups, and the largest short waves are present on the long wave crest instead of at the long wave trough. This is due to the fact that the highest short waves can only exist when the local water depth is temporarily increased under a long-wave crest, and that there is less intensive breaking present.

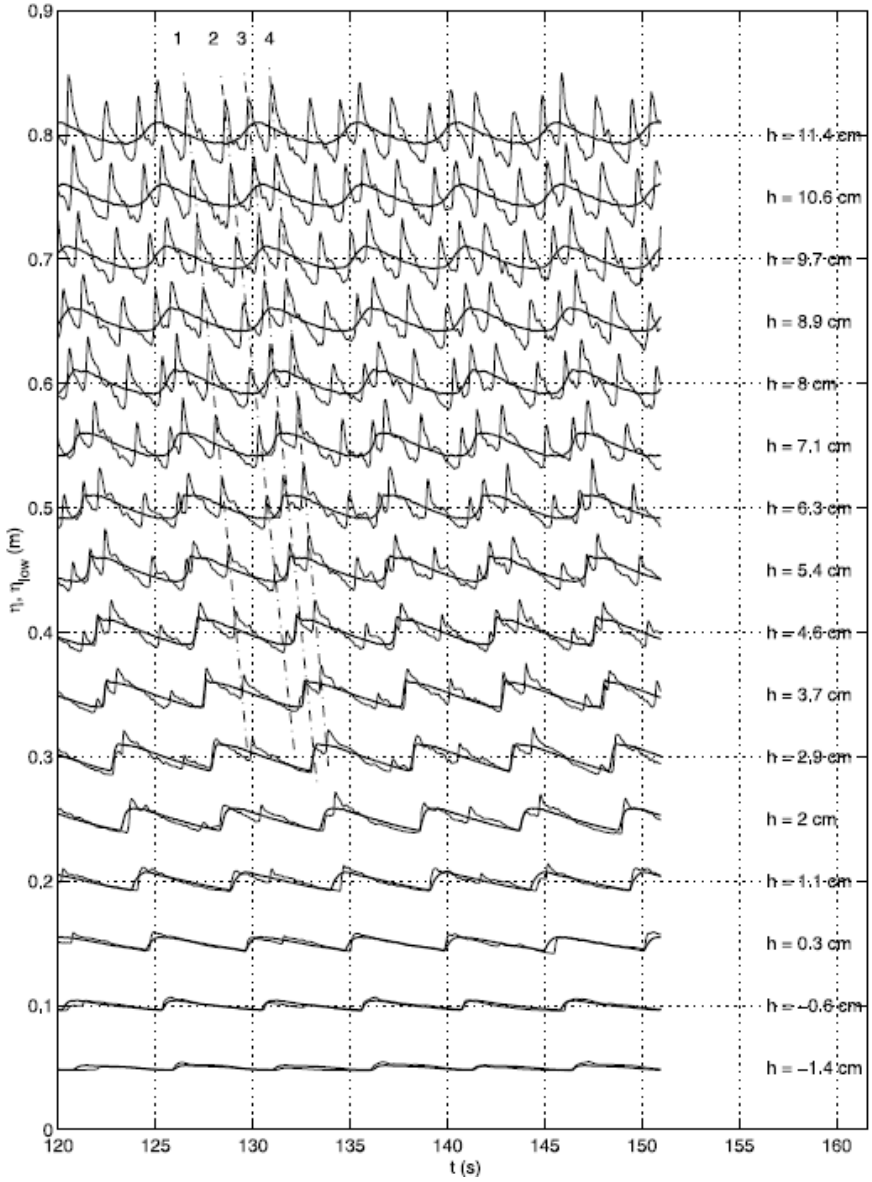

Figure 3.5: Time series of the filtered (low-frequency component and its higher harmonics) long wave (thick solid line), and total measured time series (thin solid line) for consecutive gauge positions around the still water line for case A-1. Tracks of converging wave crests are shown as dash-dotted lines. Source: Van Dongeren et al. [2007].

Houser and Greenwood [2005] analyzed the results of a field research, performed at the shoreward slope of a bar under storm conditions. The results reveal that there was an onshore directed sediment transport present at infragravity frequencies. This sediment transport increased rapidly when $H_s/h > 0.4$ (Figure 3.6b,f).

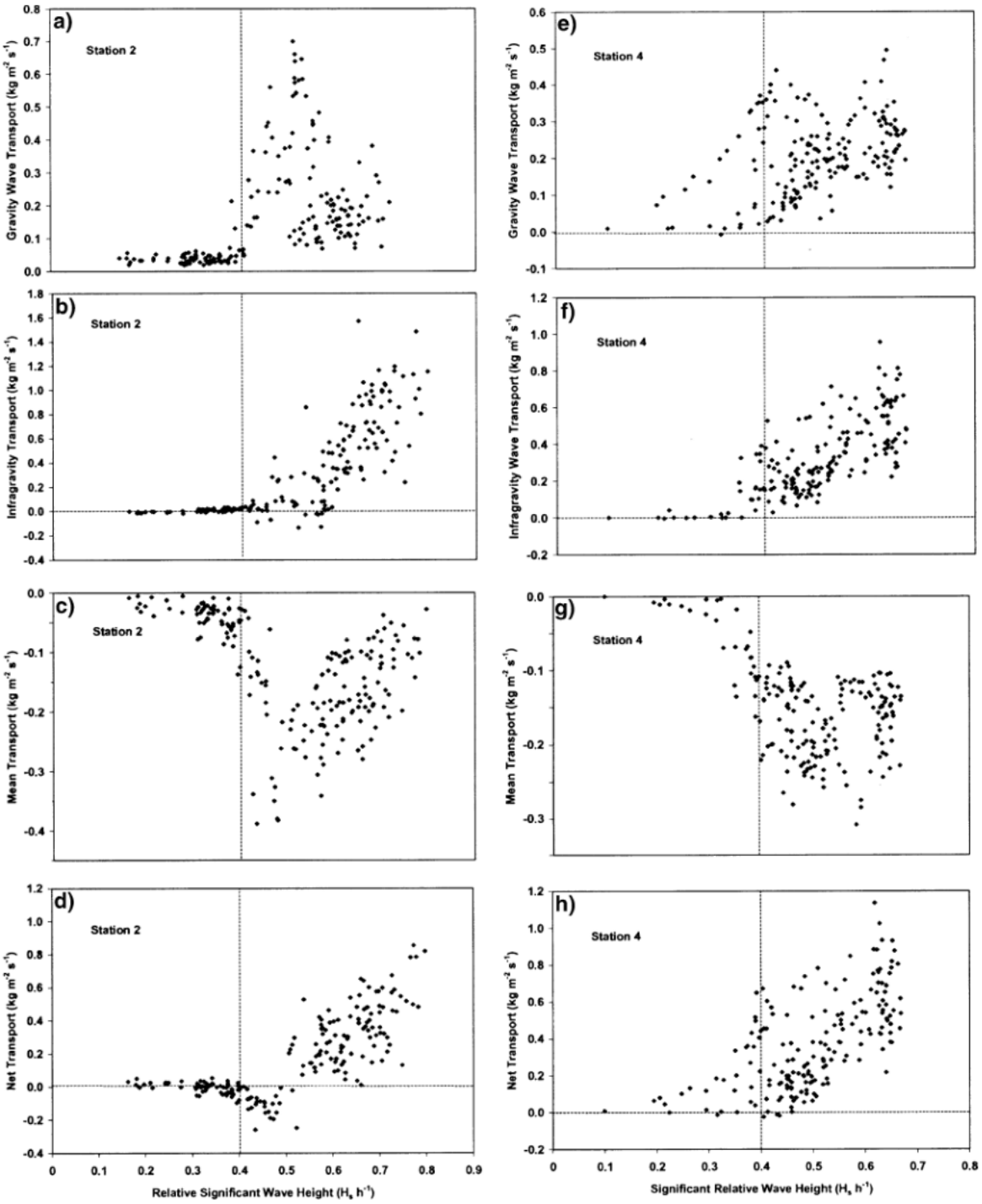

Figure 3.6: Measured gravity wave (a, e), infragravity wave (b,f), mean (c, g), and net suspended sediment transport (d, h) at Stations 2 (a-d) and 4 (which is positioned half a meter deeper in offshore direction) (e-h) relative to the respective local relative significant wave height (H_s/h). Positive (negative) values indicate a shoreward (lakeward) flux of sediment. Note the relative significant wave value of 0.4 is shown by the vertical dotted line. Also note the different scales between S2 and S4. Source: Houser and Greenwood [2005].

The dominance of the lower, infragravity frequencies under high energetic conditions can be seen in the co-spectra of Figure 3.7.

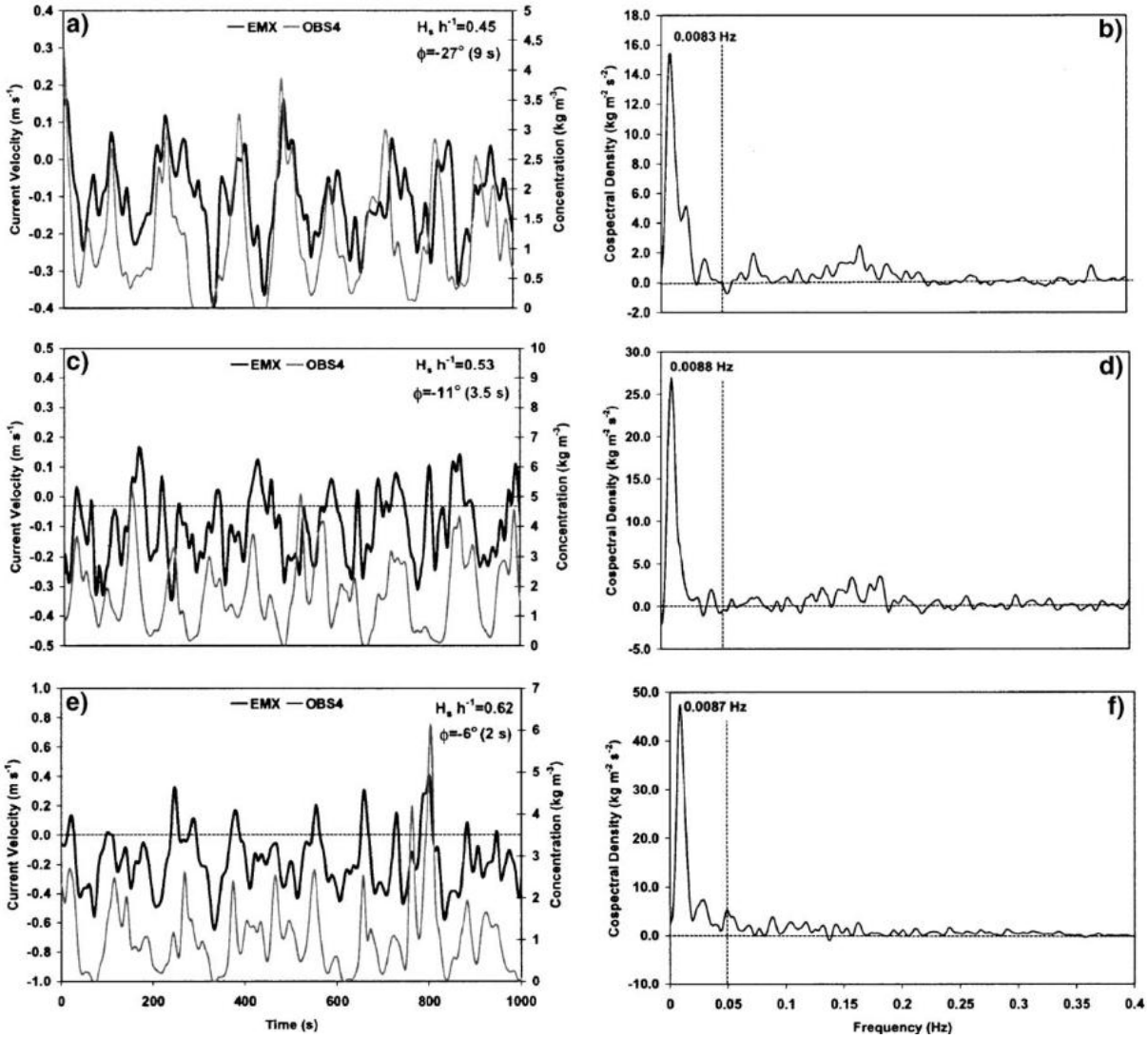

Figure 3.7: Representative low-pass filtered (0.05 Hz filter) current velocity and sediment concentration (a, c, e) with corresponding co-spectra of current velocity and suspended sediment concentration for Station 4 (b, d, f). Positive (negative) values indicate a shoreward (lakeward) flux of sediment. Also shown are the relative significant wave height ratios (H_s/h) and the average phase lag (φ) between the suspended sediment concentration and the current velocity. Source: Houser and Greenwood [2005].

Furthermore, the sediment concentrations increase ahead of the infragravity wave crest and remain in suspension during the onshore stroke of the wave. Further analysis shows that this phase lag can increase up to 9 seconds (-27 degrees).
This allows relatively more sediment to be transported in the onshore direction.

On the contrary, *Russell [1993]* concluded from his research that in the (inner) surf zone during high energetic conditions, a mean offshore transport at infragravity wave frequencies was present (Figure 3.8 *storm day and storm night*). Sand is suspended in response to the offshore velocities of the trough of the infragravity wave, and reached concentrations over 30 g/l which lasted for periods of 30 seconds. During more calm

periods (Figure 3.8 *calm day*) the gravity band was dominating the transport, and the total net transport was smaller, and more onshore directed.

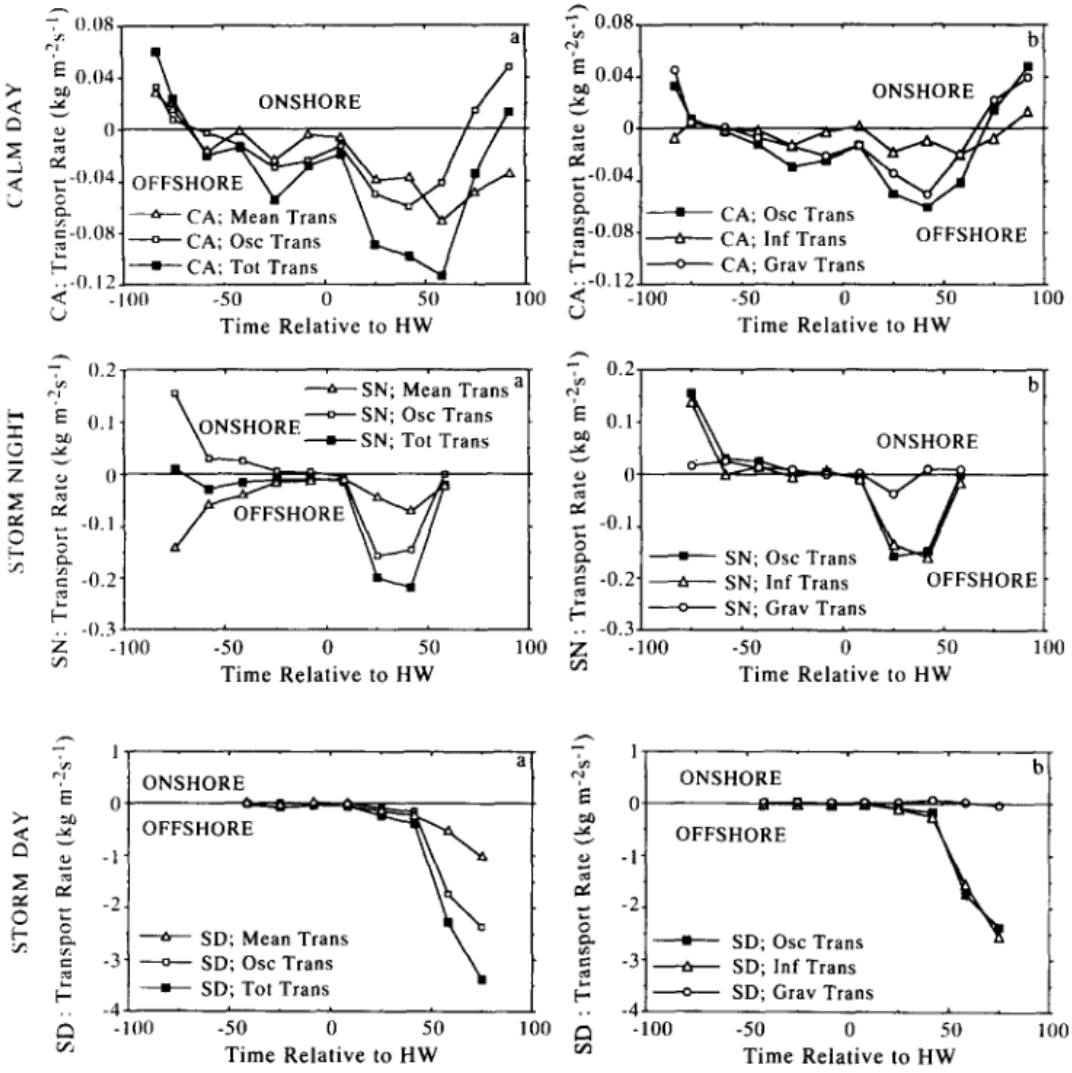

Figure 3.8: Sediment transport rate data plotted against time relative to high water, for the calm day (CA), storm night (SN) and storm day (SD). (a) The total sediment transport rate and its steady (mean) and unsteady (oscillatory) components. (b) The total oscillatory transport, and its gravity and infragravity components. Source: Russell [1993].

Furthermore, *Russell [1993]* observed that sediment suspension events were more frequent on the ebb tide, and their occurrence, density and duration increased with decreasing water depth. This may be caused by the water table of the beach, which lags the tide by 1-3 hours. Water effluence may cause increased erosion of the beach. Another option is that at the ebbing tide the bed forms formed during flooding tide are destroyed and thereby suspend the sediment in the water column.

Beach and Sternberg [1991] find contradicting transport directions in the inner surf zone (and swash zone) of a mild sloping beach. It is visible in Figure 3.9c that the sediment concentration in the infragravity wave band lags the cross-shore velocity by more than -

90°, which leads to onshore transport. However at a specific frequency of 0.004 Hz the phase has shifted to the other side of -90°, therefore leading to offshore transport (Figure 3.9b).

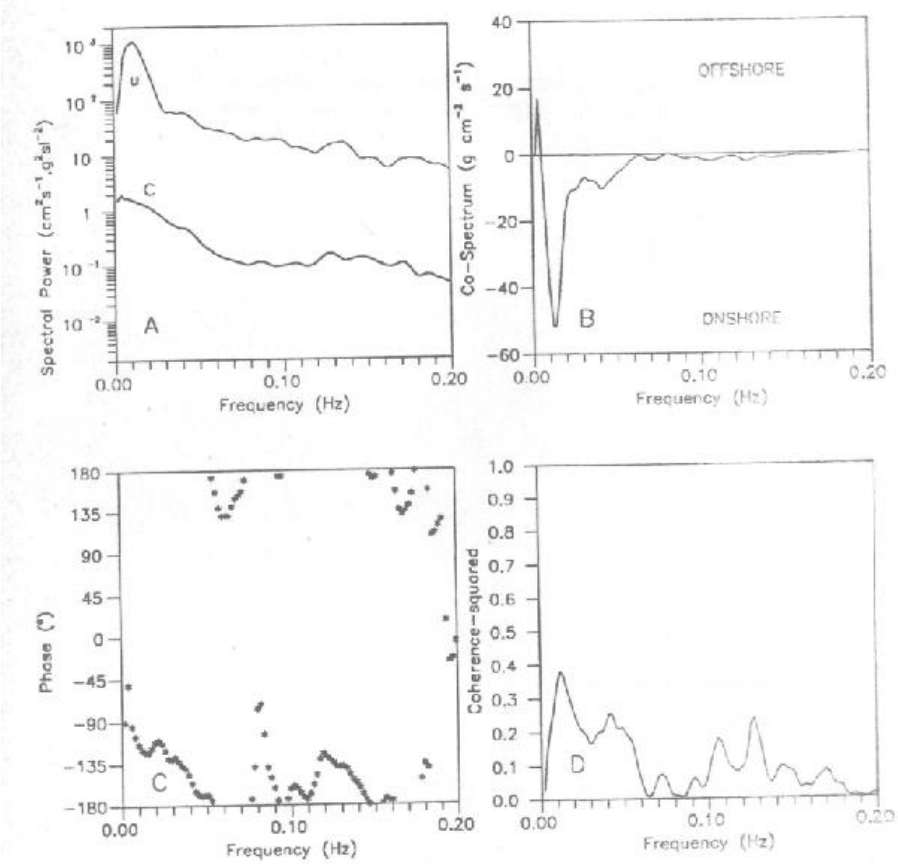

Figure 3.9: Inner surf zone: (a) spectra of cross-shore velocity, u, and suspended sediment concentration, c (z=4.5 cm), (b) co-spectrum of u and c, (c) relative phase angle between u and c, and, (d) coherence squared between u and c. 95% confidence level is 0.17. Source: Beach and Sternberg [1991].

Aagaard and Greenwood [2008] confirm the contradicting transport directions in the surf zone. As can be seen in results of their research (Figure 3.10), the transport direction in the inner surf zone can either be directed onshore as offshore, depending on the spatial location (they do not distinguish sediment transport direction per frequency).

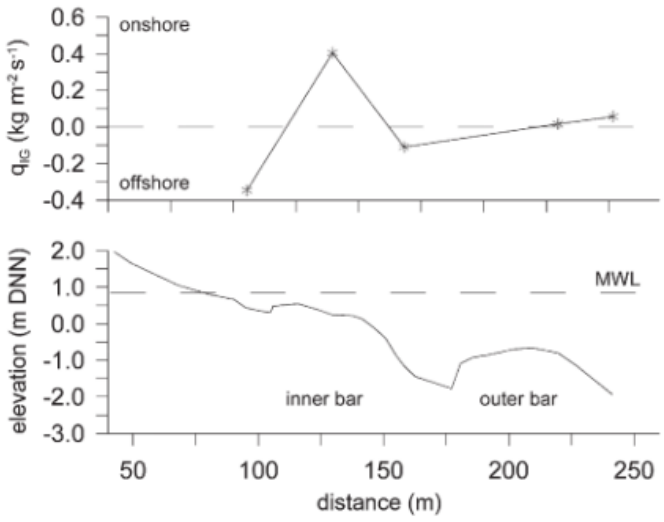

Figure 3.10: Spatial distributions of the net cross-shore suspended sediment flux at infragravity frequencies (q_{IG}) during a storm at Skallingen (upper panel). The lower panel shows the cross-shore bathymetry. Note: the dashed line indicates the mean water level during this particular instrument burst. Source: Aagaard and Greenwood [2008].

In the inner surf zone (h/h_b<1) the contribution of the infragravity wave to the total sediment transport can increase rapidly, but there is no clear pattern in the magnitude or the direction (Figure 3.11).

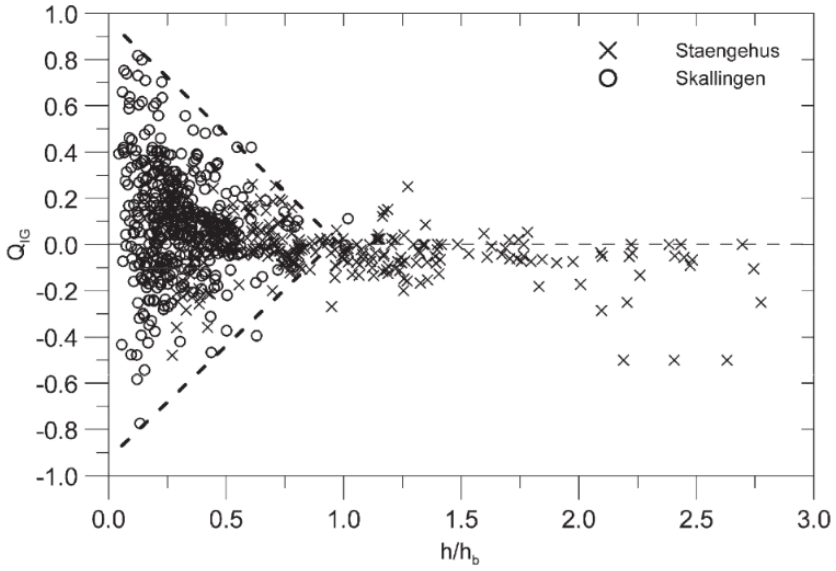

Figure 3.11: Normalized oscillatory IG wave sediment flux (Q_{IG}; (2)) plotted as a function of the local water depth relative to the water depth at first (outer) wave breakpoint (h/h_b). The sloping dashed lines approximate maximum observed values of Q_{IG}. Source: Aagaard and Greenwood [2008].

3.4 Resuspension maxima

Aagaard and Greenwood [2008] introduce the presence of resuspension maxima to explain the contradictions in transport direction by infragravity waves in the inner surf zone. The sediment concentrations in the water column are largest where maxima of relative wave heights occur. These maxima occur on upper seaward slopes and bar crests, where orbital velocities are large and incident short waves are breaking. Bed shear stresses peak under maxima of short wave heights, and due to breaking of the short waves additional turbulence reaches the bed and resuspends the sediment.
The infragravity wave acts then as an advection mechanism, and transports the sediment away from this re-suspension maxima. As can be seen in Figure 3.12, infragravity wave motions transport sediment onshore from the landward location of the resuspension maxima (under the wave crest), and offshore from location seaward of this maxima (under the wave trough). The data suggests that the transport takes place over a distance of around 20 meters, wherein the sediment gradually settles out of the water column on the seaward or landward stroke, and is deposited.

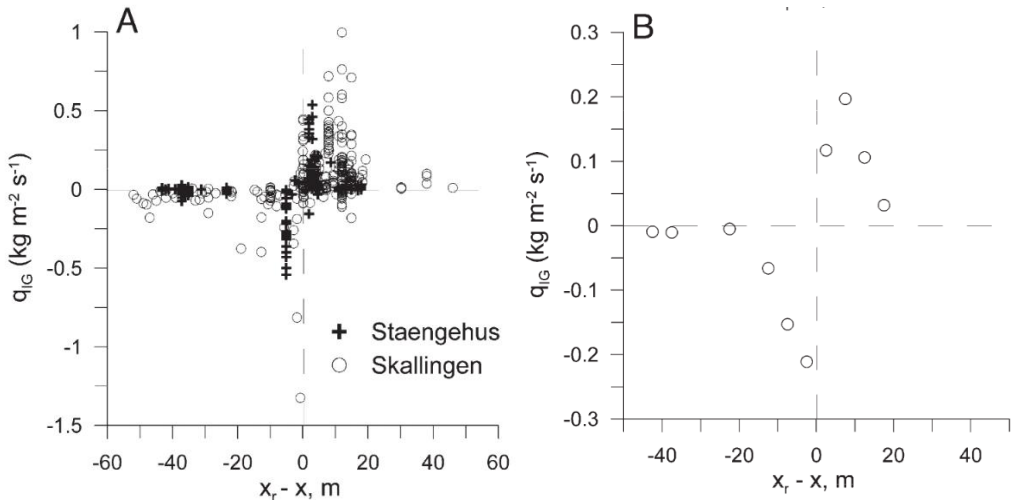

Figure 3.12: (a) Observed net infragravity sediment fluxes (q_{IG}) plotted against measurement position relative to resuspension maxima (x_r-x) for all experiments at Skallingen and Staengehus. Positive sediment fluxes signify a net onshore sediment transport and positive values of (x_r-x) indicate that the measurement position was located landward of the resuspension maximum; (b) cross-shore infragravity transport shape function computed from the data in (a). The measurements have been aggregated into 5 m cross-shore bins. Source: Aagaard and Greenwood [2008].

3.5 Conclusions

Sediment transport is determined by velocity and sediment concentrations, and can be divided into mean and oscillating components. Seaward of the surf zone, the sediment is transported offshore at infragravity frequencies. However, within the surf zone there are contradicting transport directions. This could be due to the relative location to a resuspension maximum, where from the sediment is transported in opposite directions.

Part II - Master research

Lay-out

The lay-out of this thesis is as follows. The research questions will be presented in chapter 1. Then, a description of the Ameland campaign will be given in chapter 2. The propagation and reflection of the infragravity waves will be investigated in chapter 3, from which it will become clear that there must be significant energy dissipation. The potential mechanisms for this energy dissipation will be explored in chapter 4. Then, the role of infragravity waves in sediment suspension and transport direction will be examined in chapter 5. Finally, the research conclusions will be presented, together with recommendations for future research in chapter 6.

1. Research subjects

From the literature review (Part I) is concluded that several aspects of the infragravity wave behavior are still unclear. The temporal and spatial variability of propagating wave components indicate energy dissipation of infragravity waves in the shallow nearshore. Several dissipation mechanisms have been put forward, however little field evidence supports these hypotheses. Also, contradicting sediment transport directions were observed in the inner surf zone, wherefore only one possible mechanism was put forward, without any confirmation by other research.

1.1 Aims

To improve our understanding of cross-shore hydrodynamics of infragravity waves and their role in sediment transport on a low-sloping beach, the following aims are defined:

- To study the temporal and spatial variability in total, onshore and offshore propagating infragravity energy over a low-sloping beach.
- To study processes related to infragravity wave dissipation on a low-sloping beach.
- To study the role of infragravity waves on sediment suspension and transport direction in the inner surf zone of a low-sloping beach.

1.2 Hypotheses

The hypotheses of the processes present are listed underneath.

- The spectra of incident and outgoing infragravity waves show a significant decline in energy of the outgoing waves. This is because the incident waves are not fully reflected but undergo a significant energy dissipation. The amount of reflection is frequency dependent.
- Dissipation of the infragravity wave is not caused by bottom friction but due to non-linear energy transfer back to the sea-swell waves, or by breaking of the infragravity wave itself.
- In the inner surf zone, sediment transport is in contradicting directions. This could be due to the position of a re-suspension maxima, induced by short waves, from which the sediment is transported away from this maxima in opposite directions, by the infragravity wave.

1.3 Research questions

The research questions put forward here are derived from the aims and hypotheses. These questions are to be answered by the analysis of the field data.

- What are the temporal and cross-shore variations in incident, outgoing and total infragravity wave energy?
- Is infragravity wave reflection frequency dependent?
- What is/are the mechanism(s) responsible for infragravity wave energy dissipation?
- Do infragravity waves play a role in the suspension of sediment, or do they solely act as advection mechanism?
- Is sediment transport magnitude and direction, temporal and cross-shore varying? If so, what is the mechanism behind these variations?

2. Field experiment and analysis

2.1 Field site

The field campaign took place in the autumn of 2010 (23 September - 2 November) on the mild-sloping beach of Ameland (Figure 2.1). Ameland is one of the wadden islands situated in the north of the Netherlands, it is east-west orientated and has a length of around 25 km.

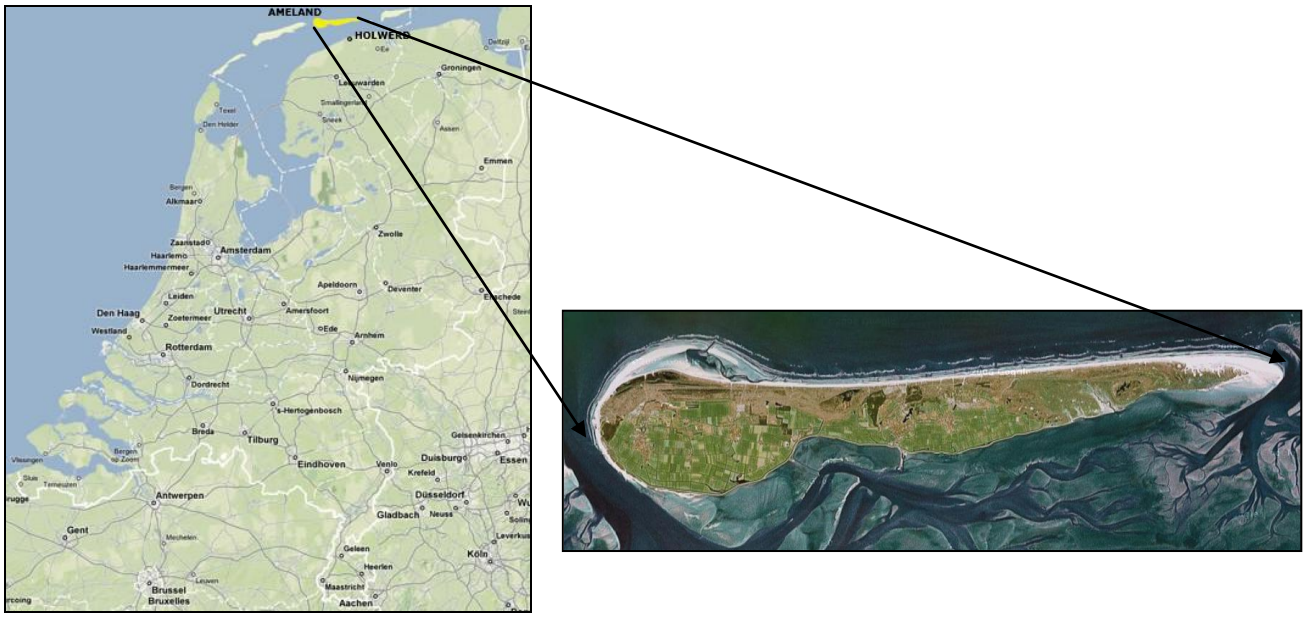

Figure 2.1: Location of Ameland. Source: www.maps.google.com and www.vvvameland.nl.

The cross-shore instrument array was positioned in the northwest of Ameland, near beach pole 5 (Figure 2.2). A shallow ebb-tidal delta is present at the northwest side of Ameland, which limits the wave conditions at the beach greatly. The beach slope is low-sloping with a ratio of 1:80. The field site is characterized by a bar at the most seaward positioned instruments.

Figure 2.2: Approximated location of cross-shore instrument array. Source: www.maps.google.com

2.2 Data collection

The data set collected during the campaign consists of observations of pressure, cross-shore and longshore velocity, and sediment concentration. The instruments were placed in a north-south oriented, cross-shore array. The array was positioned between the low and high water line, with a total cross-shore distance of around 200 m. The maximum water depth at the most seaward location was around 2.5 m. Along this transect three small triangular frames and one larger triangular frame were placed, together with ten OSSI's (see Figure 2.3). OSSI's (Ocean Sensor System Inc.), are pressure transducers attached to a pole, that was 'screwed' into the sand for around one meter. The small frames were made heavier by attaching +/- 20 kg of lead to each 'leg', and were attached to a pole buried in the sand. The larger frame was totally built up by poles of which the base was 'screwed' into the sand.

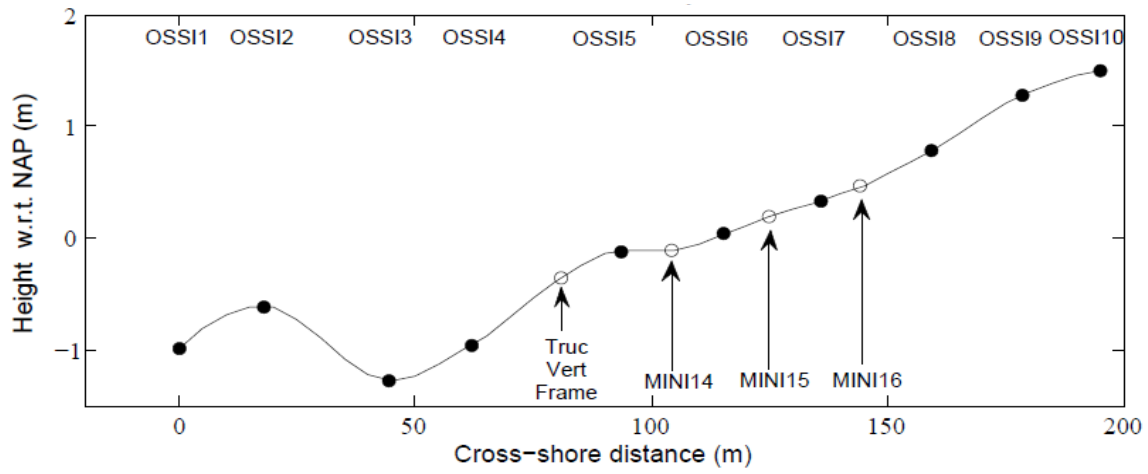

Figure 2.3: Instrument array.

The small frames, also called miniframes or tripods, were all equipped with one Keller pressure transducer, one electromagnetic flowmeter (EMF), three Optical Back-Scatter Sensors (OBSs) and a floater. The larger frame, also called Truc Vert frame, was equipped with different instruments, to be used for another master research project. Three Sontek Acoustical Doppler Velocitymeters (ADVs) were placed at different heights above the bed, together with five OBSs, a Keller pressure transducer and a floater. The OSSI's measure pressure and were placed at positions in between the frames, and further seaward and shoreward (see Figure 2.3). The EMFs, Keller pressure transducers and OBSs all measured with a sampling frequency of 4 Hz, the OSSI's with 5 Hz, and the ADVs with 10 Hz.

The instruments on the frames were connected to a PVC container (see Figure 2.4). The central element in this container is a data logger, which measures the signals from the instruments and controls their power supply. The data logger has very low power consumption and can easily be programmed. The data is stored on a Campbell Scientific

solid state storage module. A battery pack inside the container provides the power supply for the data logger and the instruments. The capacity of the battery pack is enough for 20 days of continuous measurements (http://coastalresearch.nl/research/equipment /mini-tripods).

Figure 2.4: (left) An OSSI, (centre) a miniframe with f.l.t.r. OBSs , an EMF, a floater and a pressure sensor. (right) the Truc Vert frame with f.l.t.r. three ADVs, the OBS-array, and a pressure transducer and floater on the most right 'leg'.

Due to erosion of sand during swash at the rising tide, and deposition of sand at the falling tide, the miniframes sank into the sand, and instrument heights lowered. Every day during low tide, the instrument heights were measured. When necessary the instruments were readjusted to a defined aimed height above the bed. The OSSI's were positioned at around 5-10 cm above the bed during the campaign, and the EMFs of the miniframes were repositioned at around 20 cm above the bed every day. The OBSs were positioned at different heights above the bed, the lowest just above 5 cm and the highest just above 20 cm. Data was downloaded every day from each miniframe, and around twice a week from the Truc Vert frame. The OSSI data was downloaded twice during the campaign.

With DGPS measurements, the transect was measured several times during the campaign. To obtain morphological data for the periods without DGPS data, the measured instrument heights with a correction to NAP (Dutch Ordnance Datum) were also used to derive bathymetric profiles.

As part of another Master research project, DGPS data of the intertidal section between beach poles 3.8 and 5.2 was obtained daily. Once a week surveying was conducted at an additional location between beach poles 9 and 10. Furthermore, extensive DGPS mapping was performed three times during the campaign. Due to technical issues with the equipment, no DGPS measurements could be performed from 04-10-2010 to 14-10-2010.

2.3 Initial data processing

The initial data processing will be discussed in this section. More specific data processing methods and calculations will be introduced when relevant in the following chapters.
The data output of the instruments was in milivolt, and was therefore converted to physical units for further data analysis. By subtracting the air pressure (measured continuously every ten minutes) from the pressure measured by the pressure transducers, water level fluctuations were obtained.
Pressure was converted to free surface elevation with a depth correction using linear wave theory. The second order trend in the dataset was removed. After filtering the data into e.g. high (0.05-1 Hz) and low (0.005-0.05 Hz) frequencies, auto- and co-spectra were calculated. The spectra were obtained by determining the distribution of power at a unit of frequency. This was done by dividing the data series into blocks with length 3600, using 50% overlap. Each block was tapered with a Hamming window of the same length, with 38 effective degrees of freedom and a confidence interval from 0.6679 to 1.6609.
Several basic parameters were computed. The water depth (h) is equal to the mean value of pressure (p) plus the instrument height,

$$h = mean\,(p) + zInstrument \quad (m)\,. \tag{1}$$

The mean wave angle and spread are calculated by principal component analysis. The mean angle is related to the orientation of the first eigenvector and the spread is the square root of the relative contribution of the second eigenvector.
The cross-shore and alongshore root mean square velocities, u_{rms} and v_{rms} respectively, are calculated by taking the square root of the variance of u and v:

$$u_{rms} = \sqrt{\mathrm{var}(u)} \quad (m/s)\,, \tag{2}$$

$$v_{rms} = \sqrt{\mathrm{var}(v)} \quad (m/s)\,, \tag{3}$$

The significant wave height is equal to four times the standard deviation of the sea surface elevation (η):

$$Hm0 = 4 \cdot std(\eta) \quad (m)\,, \tag{4}$$

2.4 Wave and water level conditions

2.4.1 Offshore boundary conditions

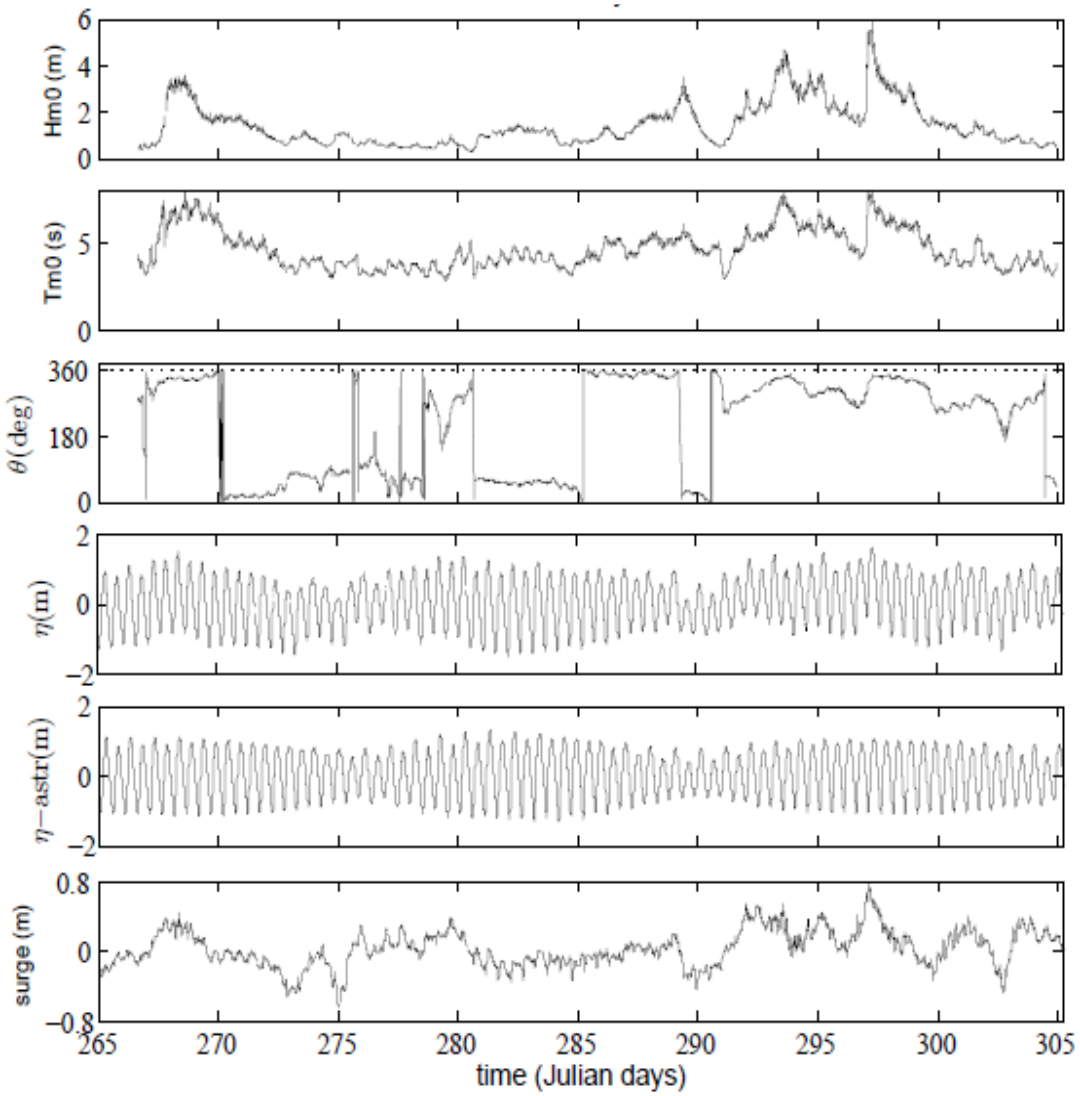

Figure 2.5: Offshore boundary conditions during the Ameland campaign. a) Significant wave height (Hm0), b) significant wave period (Tm0), c) wave direction (θ), d) measured offshore water level fluctuations (η), e) astronomical tide and f) the local surge.

The significant wave height (*Hm0*), the wave period (*Tm0,2*) and wave direction (*θ*) were measured by a directional buoy positioned seaward of the outer delta near Ameland in about 24 m depth. The offshore water level fluctuations were measured at the tidal station Terschelling Noordzee, located 20 km to the west of the instrument array. By subtracting the astronomical tide (Figure 2.5e) from the measured tide, the local surge (Figure 2.5f) was estimated. The shore normal line is plotted at 360 degrees in Figure 2.5c.

The field campaign contained two periods with storm conditions. At Julian days 268 and 269 the first storm caused the offshore significant wave heights to reach 3.5 meters. Then a period of calm conditions followed, and from Julian day 293 up to 299 another

period of storm was present. This storm period caused the development of larger offshore significant wave heights, that reached up to 5-6 meters.

2.4.2 Transect

Mostly due to the ebb-tidal delta located some kilometers off the coast, the wave characteristics of the energy conditions were altered when reaching the instrument array.

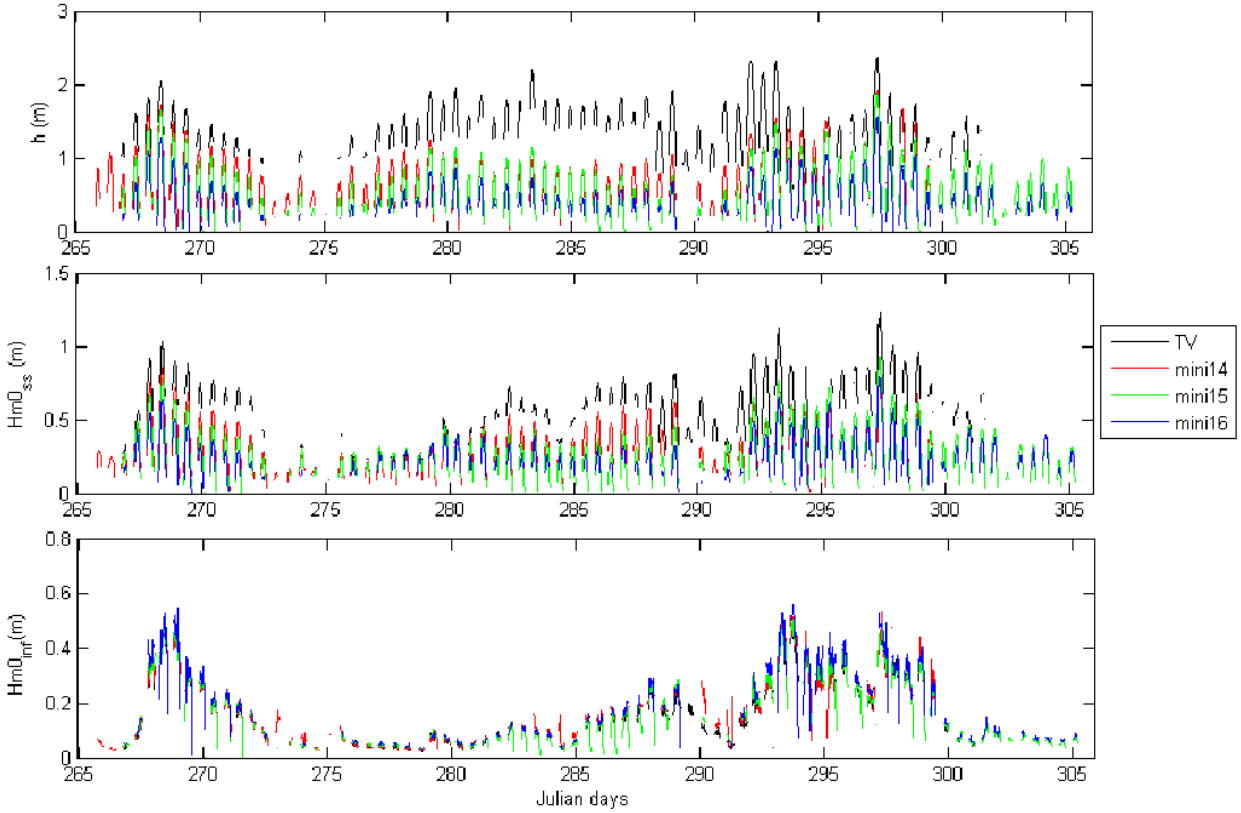

Figure 2.6: Wave characteristics at the instrument array. (Top) Water depth (h), (middle) Significant short wave height ($Hm0_{ss}$), (bottom) Significant infragravity wave height ($Hm0_{inf}$).

The significant short wave heights were much lower (< 1 m) at the transect, due to breaking on the delta and bed friction between the delta and the transect. The short waves are tide-modulated due to breaking on the delta and over the transect. The significant infragravity wave heights reached up to 0.57 meter during high energetic conditions. The infragravity wave heights are dependent on the deep-water short wave height.

The significant infragravity wave height ranged between 0.02 and 0.57 m during the campaign. The ratio of infragravity to sea-swell variance (*m0*) varied from less than 0.01 to about 3.5, with the highest ratios at the shallowest locations during the most energetic conditions (Figure 2.7).

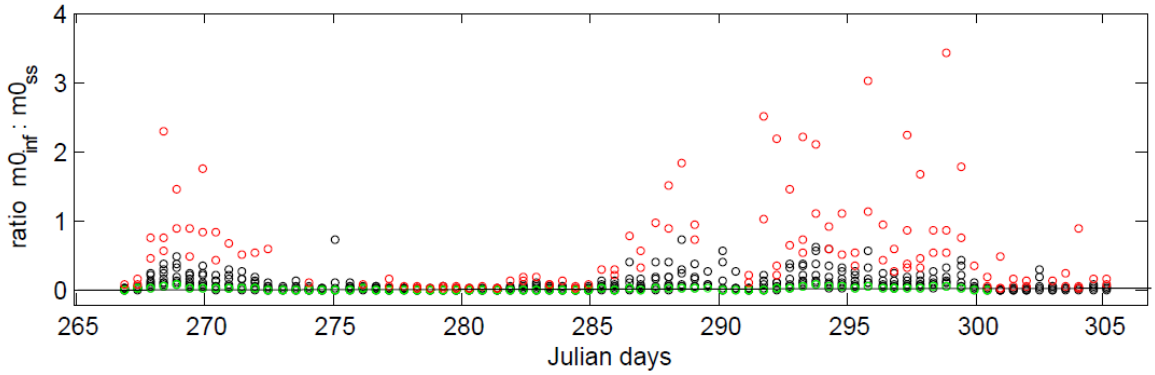

Figure 2.7: Ratio of the infragravity to sea-swell variance (m0) at the array. Green circles indicate the most seaward positioned pressure sensor, OSSI1, red circles indicate the four most landward positioned pressure sensors.

At all locations, the infragravity significant wave height ($Hm0_{inf}$) correlated well with the offshore significant sea-swell height ($Hm0_{ss,0}$) (Figure 2.8). At the most seaward located pressure sensor OSSI 1, the best-fit linear line had a skill (R^2) of 0.84, and a constant of proportionality of 0.12 (Figure 2.8b).

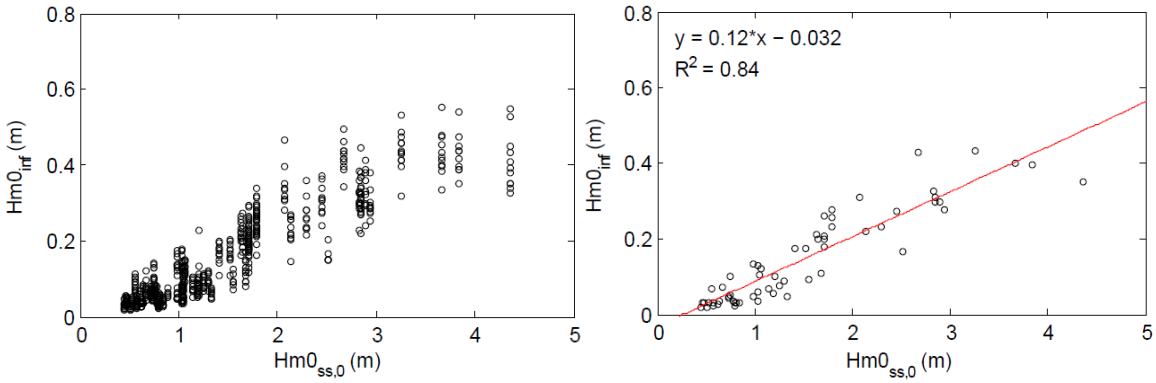

Figure 2.8: (Left) Infragravity wave height plotted against offshore significant sea-swell wave height, (right) Infragravity wave height at OSSI 1 plotted against offshore significant sea-swell wave height.

2.5 Cross-section transect

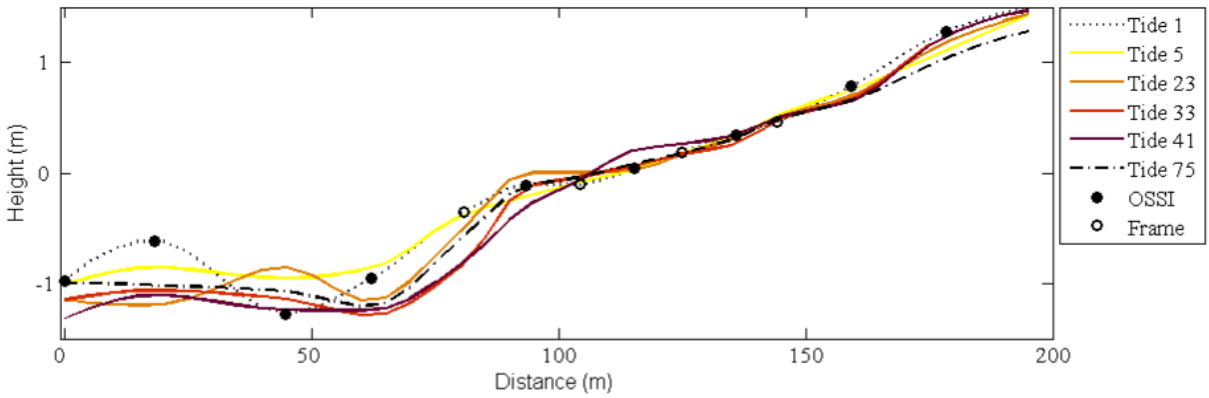

Figure 2.9: Morphological development during the Ameland campaign. Cross-section of the first and last measured tide are plotted, together with the four tides selected for further analysis. The closed circles represent OSSI's, and the open circles represent the frames.

The higher part of the transect did not erode or accrete considerably during the campaign (Figure 2.9). The bed at OSSI 10 lowered with about 20 cm in total. At the seaward side of the transect, an initially clear bar- trough system flattened. The bar crest moved in the onshore direction during the first weeks, where after the bed more or less flattened.

2.6 Data selection

The dataset was analyzed by selecting two hours around high tide for each of the 75 recorded tides. Furthermore, to be able to study the variations in behavior of the infragravity waves with respect to energetic conditions, four tides were selected representing four different energy conditions. From high to low: *Tide 5, Tide 41*, *Tide 33* and *Tide 23*.

The sea-swell significant wave heights (*Hm0*) along the transect for the four selected tides are plotted in Figure 2.10a. The significant wave height on the seaward (landward) side of the ebb-delta is plotted at x = -100 m (x = -80 m) instead of the real cross-shore location, to be able to point out the development of the significant wave height seaward of the transect.

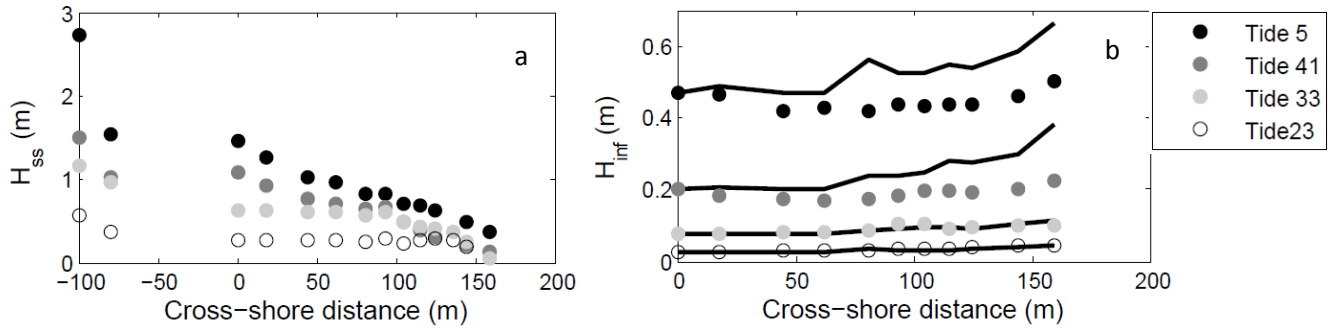

Figure 2.10: Significant wave heights of (a) sea-swell waves and (b) infragravity waves. The lines in the right hand plot are H_{inf} predictions for conservative free long waves according to Green's Law.

At high (Tide 5) and intermediate (Tide 41) energy conditions H_{ss} decayed over the entire transect. At the lower energy conditions (Tide 33 and 23) wave breaking is restricted to the landward side of x ≈ 100 m.

The infragravity wave height (Figure 2.10b) was approximately constant over the entire transect. To check whether this is according to the expected shoaling behavior in shallow water, the observations are compared with predictions for conservative, free infragravity waves based on Green's Law. Green's law states that the product of the wave height squared and the water depth, is the same for each cross-shore location through energy conservation,

$$H_{p1}^{\ 2} \cdot h_{p1} \approx H_{px}^{\ 2} \cdot h_{px} \ , \qquad (5)$$

where H_{p1} is the wave height at the most offshore location, in our case OSSI 1, and H_{px} can be the wave height at any location in the cross-shore direction. The water depth, h, is selected for those same cross-shore locations. From this the wave height at H_{px} can also be predicted,

$$H_{px} = H_{p1}\left(\frac{h_x}{h_{p1}}\right)^{-0.25} \quad . \tag{6}$$

The predictions for our data show the same behavior as the observed lower energy conditions, for Tide 23 and most of Tide 33 (x < 125 m). However, for the shallower part of Tide 33, and intermediate and high energy conditions, the predictions show increasingly divergence with the data. When coming closer to the shoreline and during more energetic conditions the observed infragravity waves undergo less shoaling than predicted. This points out a significant energy loss at infragravity frequencies, when infragravity waves are energetic and sea-swell waves are breaking.

3. Propagation and reflection of the infragravity wave

The first research question: *"What are the temporal and cross-shore variations in incident, outgoing and total infragravity wave energy?"* studies if the outgoing infragravity wave energy flux is smaller than the incoming energy flux due to energy dissipation. This is expected based on Part I of this thesis, and on the divergence of H_{inf} with Green's Law during energetic conditions, as seen in Chapter 2. The second question: *"Is infragravity wave reflection frequency dependent?"* studies whether infragravity wave propagation and reflection varies with frequency, as is expected based on Part I.

3.1 Reflection

Shoreward propagating low frequency waves reflect at the shoreline and then propagate in the seaward direction. Reflection coefficients <1 (>1) imply an energy sink (source) between the shoreline and the observation site. Reflection is calculated by dividing the offshore directed energy flux by the onshore directed energy flux. The seaward and shoreward energy fluxes can be determined in different ways (e.g. *Sheremet et al. [2002]* and *Van Dongeren et al. [2007]*). For this section, the energy fluxes were calculated with the method of *Sheremet et al. [2002]* because it allows to separate also the short-wave fluxes into incoming and outgoing fluxes. Surface elevation time series of shoreward and seaward propagating components were constructed by detrending, high-pass filtering and performing a linear-theory pressure-to-sea surface correction. The energy (E) and cross-shore energy fluxes (F) of shoreward (+) and seaward (-) propagating infragravity waves at frequency f and location x are:

$$E^{\pm}(f,x) = \frac{1}{4}\left[C_{pp}(f,x) + (h/g)C_{uu}(f,x) \pm (2\sqrt{h/g})\,C_{pu}(f,x)\right], \quad (7)$$

$$F^{\pm}(f,x) = E^{\pm}(f,x)\sqrt{gh}, \quad (8)$$

where C_{pu} is the pressure (p) velocity (u) co-spectrum and C_{pp} and C_{uu} are p and u auto-spectra, respectively. The net cross-shore flux is:

$$F^{+} - F^{-} = hC_{pu}. \quad (9)$$

Energy flux densities were integrated over the infragravity frequency band (0.005–0.05 Hz) to estimate bulk infragravity fluxes $F_b^{\pm}$ and bulk reflection coefficients R^2:

$$F_b^{\pm}(x) = \int_{0.005Hz}^{0.05Hz} F^{\pm}(f,x)\,df, \quad (10)$$

$$R_b^{\,2}(x) = F_b^{-}(x)/F_b^{+}(x). \quad (11)$$

Analogously, bulk values for the sea-swell band (0.05-0.33 Hz) were computed.

In Figure 3.1 the bulk reflection coefficients for the infragravity and sea-swell bands are plotted against the offshore sea-swell variance ($m0_{ss}$). The reflection of infragravity waves is, as expected, higher (0.3-0.5), than for sea-swell waves (< 0.1). However, the reflection coefficients for infragravity waves are much lower than 1, which indicates a significant energy dissipation.

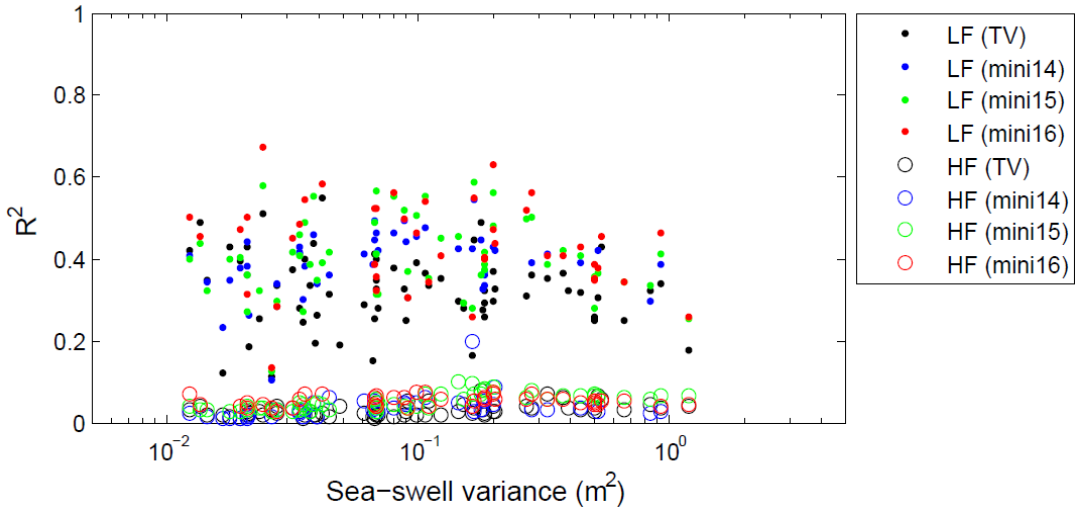

Figure 3.1: Reflection (R^2) plotted against offshore sea-swell variance. The open circles (dots) represent reflection at sea-swell (infragravity) frequencies.

Reflection at sea-swell and infragravity frequencies is not influenced by sea-swell variance (Figure 3.1). On average the reflection at more shoreward locations (frame 15 and 16) is somewhat higher. For sea-swell waves this is probably caused by energy dissipation of incoming sea-swell waves. Whereas for infragravity waves, this may be caused by both energy loss of the seaward travelling infragravity waves, and energy loss of incoming infragravity waves.

Miche [1951] determined that monochromatic waves, normally incident on a plane laboratory beach are following the Miche number regarding reflection.

$$R^2 \approx 1 \quad when \quad M = \frac{16g^2}{(2\pi)^5} \frac{\tan^5 \beta}{H^2{}_\infty f^4} \geq 1 \ , \tag{12}$$

where β is the beach slope, H_∞ and f are the deep water wave height and frequency respectively and g is the gravitational acceleration. *Miche [1951]* suggested that

$$R^2 \approx M \quad when \quad M < 1, \tag{13}$$

with the remainder of energy dissipated due to wave breaking. Based on these equations, the reflection of (high frequency) waves would follow the Miche number. Since we are dealing with lower frequency waves, H_∞ and f were substituted by infragravity wave height at OSSI 1 and a representative infragravity frequency respectively. For a frequency of 0.02 Hz, the infragravity waves are in between M = 10^{-3} and M =10^{0} (larger

spread than the reflection rates), much higher numbers as expected than the sea-swell waves, which are in between M = 10^{-12} and M = 10^{-10}.

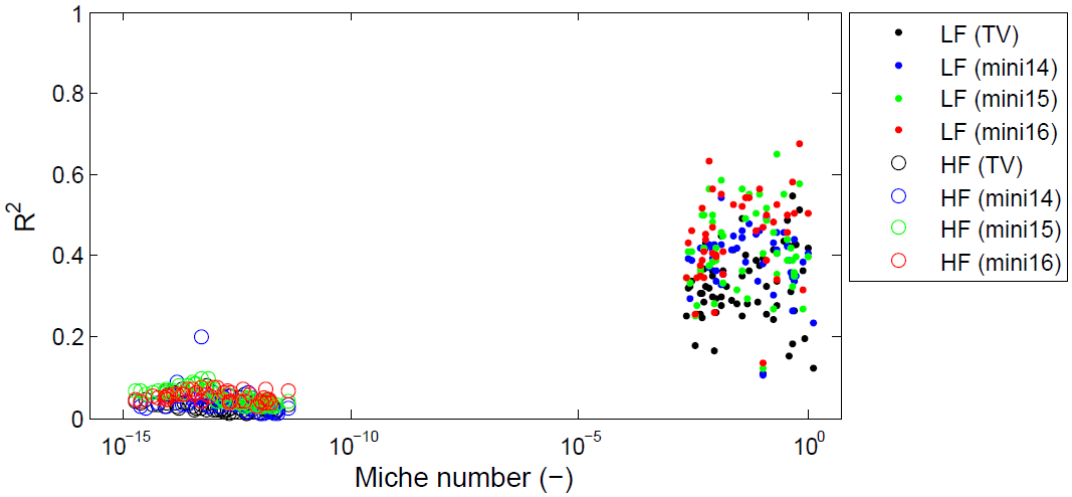

Figure 3.2: Reflection (R^2) plotted against Miche number. The open circles (dots) represent reflection at high (low) frequencies.

3.2 Fluxes

As mentioned before, the seaward and shoreward energy fluxes can be determined in different ways (e.g. *Sheremet et al. [2002]* and *Van Dongeren et al. [2007]*). The *Van Dongeren et al. [2007]* method for infragravity waves was used here because it is applicable as well on the OSSI's, where only pressure data is available, whereas for the *Sheremet et al. [2002]* method velocity observations are required to be able to separate into incoming and outgoing energy fluxes.

The *Van Dongeren et al. [2007]* method is a multi-sensor separation method, based on the *Battjes [2004]* method with modifications for shoaling and phase speed effects. As it is a multi-sensor method, multiple sensors are used to determine reflection coefficients at one location. More sensors, say five instead of three, were used for periods > 50-70 s to obtain more accurate results, but consequently, more sensors on the outer sides of the instrument array do not return values.

Because this method is only applicable on infragravity frequencies, the sea-swell fluxes were calculated with the product of the auto-spectra of pressure with the group velocity (c_g), followed by an integration over the frequency bands to obtain the bulk sea-swell flux. This method does not separate between incoming and outgoing fluxes, but as the outgoing sea-swell flux is (very close to) zero it can be neglected.

The bulk sea-swell fluxes decrease in the shoreward direction for all conditions (Figure 3.5a), whereas incoming infragravity energy fluxes decrease only during high to moderate energy conditions (Tide 5 and 41). For low energy conditions (Tide 23 and 33)

energy fluxes increase towards the shore (Figure 3.5c-f). In all cases seaward directed infragravity fluxes are significantly lower than shoreward directed fluxes, although reflection coefficients are still considerable (0.3-0.5) (Figure 3.5b). Overall, reflection coefficients for less energetic tides (Tides 23 and 33) are considerably higher than those of the more energetic tides (Tides 5 and 41), which indicates more infragravity energy dissipation during more energetic conditions. Reflection coefficients of infragravity waves increase slightly in the shoreward direction at more energetic tides, whereas reflection at less energetic tides shows a decrease. This points toward a different region of dissipation for incoming waves during higher energetic conditions. Energy dissipates already in deeper water (Figure 3.5c-f).

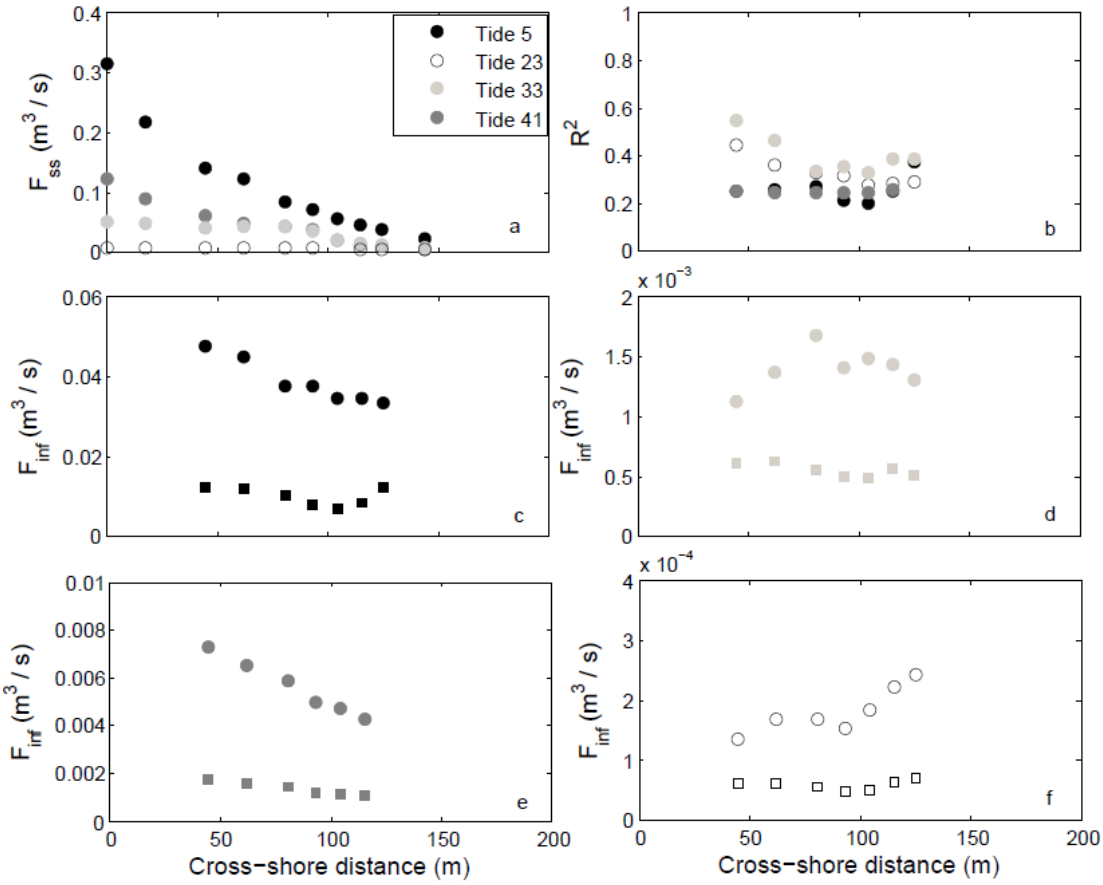

Figure 3.5: Energy fluxes and reflection for the selected tides. (a) Sea-swell flux, (b) reflection, (c-f) infragravity flux where dots (squares) are representing shoreward (seaward) energy fluxes, c) Tide 5, d) Tide 33, e) Tide 41, f) Tide 23.

3.3 Frequency dependence

To study which infragravity frequencies loose energy, the dominant cross-shore structure, phase difference and reflection coefficient were calculated for several infragravity frequencies. When at the magnitude of the dominant cross-shore structure a maximum or minimum coincides with a phase jump of +/- π, the wave is characteristic of a standing wave, and no energy dissipates. This energy conservation is reflected in the

higher reflection coefficients (R^2 ≈1). When however, no clear maximum and minimum is present in the dominant cross-shore structure, and the phase difference is increasing approximately linearly towards the shore, a progressive wave is present due to energy dissipation of the shoreward propagating wave. This energy dissipation is reflected in the much lower reflection coefficients (R^2<<1).

First the data was compensated for clock drift, then the dimensionless dominant cross-shore structure was determined by an eigenfunction analysis of the cross-spectral matrix at each infragravity frequency (Emperical Orthogonal Function, EOF), based on *Henderson et al. [2000]*. Furthermore, the phase difference and reflection at all measuring locations were determined at the same frequencies. The phase difference was calculated from a cross-spectrum of pressure with respect to the most outer positioned instrument, OSSI1, set such that the phase difference is initially zero. For all four tides, the dominant eigenfunction explained 90-99% of the variance.

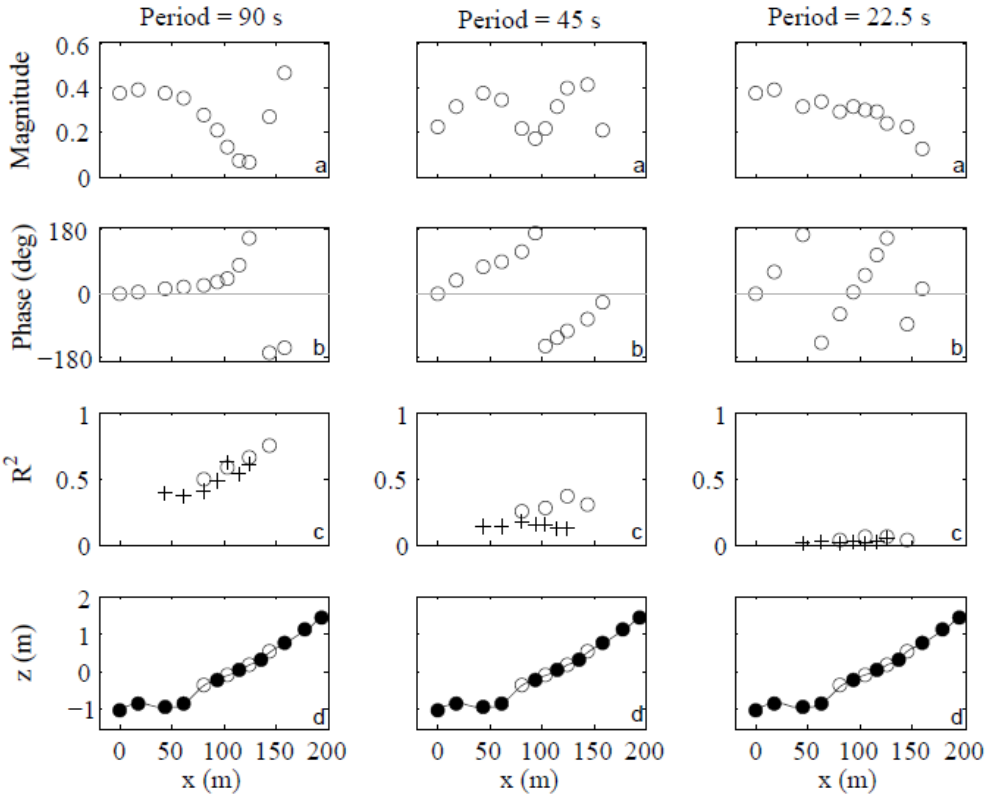

Figure 3.6: Three infragravity wave periods during high energetic conditions (Tide 5). a) eigenfunction dominant cross-shore structure, b) phase, c) reflection coefficient R2, circles (plusses) show the Sheremet et al., [2002] (Van Dongeren et al., [2007]) method, d) cross-shore transect, closed (open) circles show the positions of the OSSI's (frames).

In Figure 3.6, the results for high energetic conditions (Tide 5) are plotted. For the period T = 90 s (f = 0.11 Hz) wave, a clear maximum and minimum in the cross-shore pattern can be observed, together with a phase jump at the minimum value. This is clearly a standing wave, which is also reflected in the overall high reflection coefficients (0.4-0.8). For the T = 45 s (f = 0.022 Hz) wave, the dominant cross-shore pattern is somewhat

disturbed, with no clear maximum and minimum. Furthermore, the phase difference is increasing linearly, which is indicative of a progressive wave. The energy dissipation that is causing this progressive wave pattern, is also reflected in the lower reflection coefficients (0.1-0.4). For the T = 22.5 s (f = 0.044 Hz) wave, the flattening of the dominant cross-shore structure, and the steeper linear increase of the phase difference show that significant energy dissipation is present, which is also reflected in the very low reflection coefficients (0-0.1). The transition from a standing to a progressive wave is approximately at T of 65 s (f = 0.0167 Hz). This change from cross-shore standing to progressive infragravity waves corresponds with the results of *Henderson et al. [2000]*, although they observed the transition at much higher frequencies (0.03 Hz).

Compared to lower energetic conditions, Tide 23 (Figure 3.7), Tide 33 and Tide 41 (not shown here), more energy dissipates. At low energetic conditions the phase difference is progressing slower and the overall reflection coefficients are higher. In the case of Tide 23, R^2 = 0.5-1 for the 90 s wave, R^2 =0.3-0.6 for the 45 s wave and R^2 =0.1-0.3 for the 22.5 s wave. This confirms the results of section 3.2, where the larger energy dissipation at more energetic conditions was also observed.

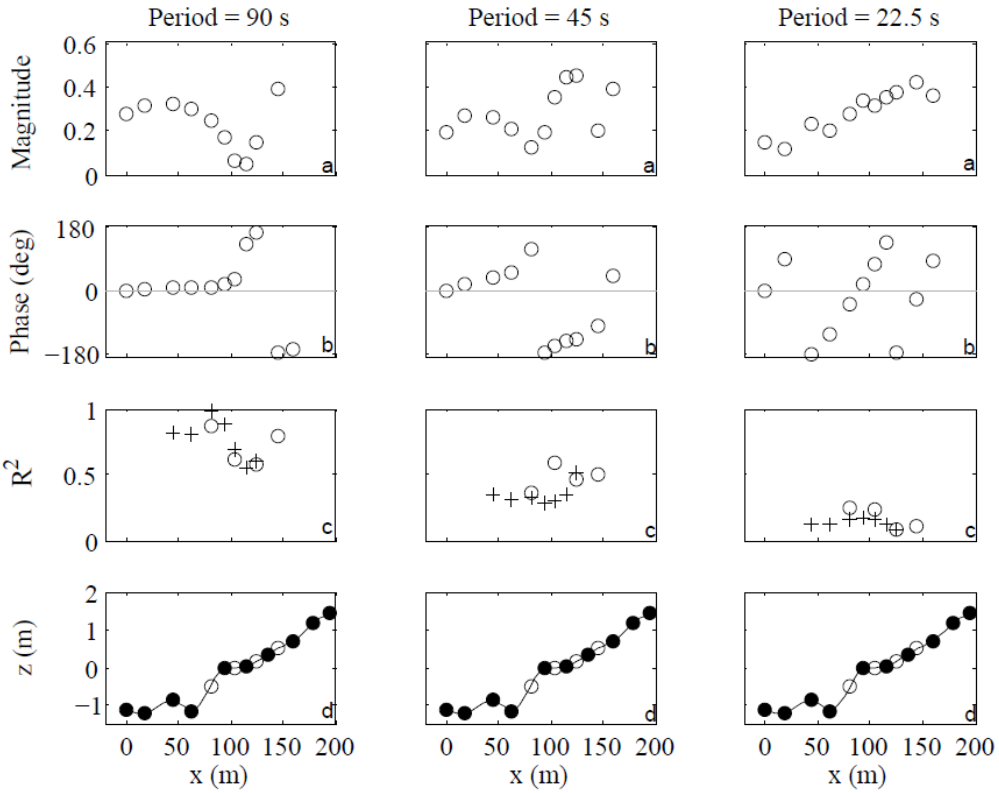

Figure 3.7: Three infragravity wave periods during low energetic conditions (Tide 23). Descriptions are the same as for figure 3.6.

A first indication of the energy dissipating mechanism can be found in the fact that for the shorter infragravity periods (< 60 s) dissipation takes place in very shallow water (0.5 - 1 m), what suggests that breaking is the dominant dissipation source.

3.4 Conclusions

Infragravity waves experience a considerable reflection (R 0.3-0.5), but are clearly not reflecting fully (R^2=1). This implies a significant energy dissipation of the infragravity wave, as expected. The incident infragravity energy flux decreases in the shoreward direction during more energetic conditions (Tide 5 and 41), whereas for less energetic conditions (Tide 23 and 33) the infragravity energy flux increases. The outgoing energy flux stays more or less constant. The reflection coefficient increases (decreases) slightly in the shoreward direction at more (less) energetic conditions. The relation between incident and outgoing infragravity wave energy does not show a temporal variation.

The infragravity reflection coefficient is indeed frequency dependent. Infragravity frequencies above about 0.0167 Hz, have a different cross-shore structure compared to frequencies < 0.0167 Hz (for all energetic conditions). This is due to significant energy dissipation at the higher infragravity frequencies.
At more energetic conditions more energy dissipates and reflection coefficients are smaller. That the energy dissipates in shallow water (h = 0.5-1 m), points to infragravity wave breaking as dissipation mechanism.

4. Dissipation mechanisms

The research question studied in this chapter is: *"What is/are the mechanism(s) responsible for infragravity wave energy dissipation?"*. In the previous chapter an inshore infragravity wave dissipation source was found, which is contradicting the *Henderson et al. [2006]* and *Thomson et al. [2006]* concept of a non-linear energy transfer back to the sea-swell waves. However, it agrees with the laboratory observations of *Van Dongeren et al. [2007]* who suggested infragravity wave breaking. Therefore the wave breaking concept as mechanism for energy dissipation will be studied further in this chapter. First the bottom friction and wave breaking are modeled according to the *Van Dongeren et al. [2007]* method, to examine the contribution of both components. Then the relation of the reflection coefficient with the bed slope parameter β_H is examined. Finally, the size of the infragravity surf zone is determined.

4.1 Modeling dissipation components

To examine the contribution of bottom friction and wave breaking to the total energy dissipation of the infragravity waves, *Van Dongeren et al. [2007]* modeled the cross-shore energy equation for linear, shoreward-propagating long waves based on laboratory data:

$$\frac{d}{dx}\left(\sqrt{gh}\,\frac{1}{8}\rho g H_{rms,lf}^{2}\right) = -D_{bot} - D_{br} \quad , \tag{11}$$

where g is the gravitational acceleration, h is the water depth, H_{rms} is the root mean square wave height at a specific low frequency, and D_{bot} and D_{br} are terms that account for dissipation of wave energy due to bottom friction and breaking, respectively. The dissipation rate due to breaking [*Battjes and Janssen, 1987]* is modeled as

$$D_{br} = \alpha_{br} f_{lf} \rho g \frac{H_{rms,lf}^{2}}{4}, \tag{12}$$

where α_{br} is a tuning parameter taken to be 1 and f_{lf} is the specific infragravity frequency. The bottom friction dissipation rate is modeled according to *Henderson and Bowen [2002]* as:

$$D_{bot} = f_{cw}\rho\left(\frac{g}{h}\right)^{3/2}\frac{H_{rms}}{\sqrt{8}}\frac{H_{rms,lf}^{2}}{8} \quad , \tag{13}$$

where f_{cw} is the friction coefficient, chosen as 0.015. *Van Dongeren et al. [2007]* have relaxed the assumption of weak low-frequency motions by using H_{rms} instead of $H_{rms,hi}$.

This method was applied on the four selected tides of our field data set, at a frequency representative for conservative standing waves (0.011 Hz), and at a frequency

representative for progressive waves (0.044 Hz). With as input parameters *h* and $H_{rms,}$ is by continuous re-iteration at every dx (defined as 1 m), the evolution of $H_{rms,lf}$ and the energy flux was obtained.

Unfortunately can due to different calculation methods, the modeled energy fluxes not be compared directly with the calculated energy fluxes by the *Van Dongeren et al. [2007]* multi-sensor separation method described earlier in section 3.2. The modeled $H_{rms,lf}$ can be compared with the calculated $H_{rms,lf}$ of the *Van Dongeren et al. [2007]* multi-sensor separation method. The modeled $H_{rms,lf}$ for the low infragravity frequency (0.011 Hz) follows the calculated values quite well, except for the jump at the shoreline (which is representative for the standing wave pattern), and the shoaling of the waves during calmer wave and water level conditions (Tide 33 and 23) (Figure 4.1). On the contrary, the modeled wave height at higher infragravity frequencies does not follow the observed trend at all. This is largely due to the overestimation of the energy dissipation attributed to D_{br}. If the term f_{lf} in the equation for D_{br} is lowered to e.g. 0.011 Hz, with all other parameters kept the same, the modeled trend follows the observations far better.

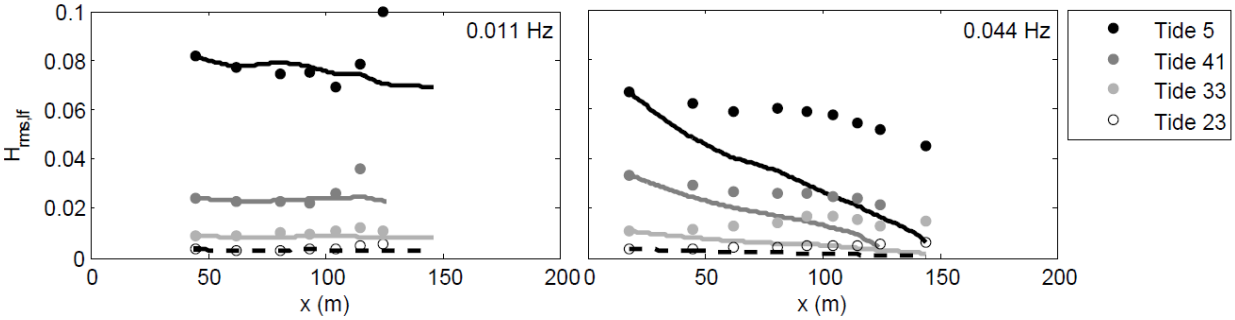

Figure 4.1: *Van Dongeren et al.* multi-sensor separation method (dots) and modeled (line) infragravity frequency wave height for the four selected tides. left) For 0.011 Hz, right) for 0.044 Hz.

The D_{br} - term dominates the total energy dissipation for all conditions and at both frequencies (Figure 4.2). At a frequency of 0.011 Hz, D_{bot} and D_{br} have the same order of magnitude, and both reflect the topography (e.g. the increase in energy dissipation due to bottom friction and breaking at Tide 23 and 33 at x~100 m, the location of the beach face). D_{bot} increases towards the shore due to the decrease in water depth. Whereas at 0.044 Hz D_{br} is overestimated, and is much larger than D_{bot}.

Although this method seems to confirm the dominance of infragravity wave breaking, it is so far not capable of predicting the $H_{rms,lf}$ at all infragravity frequencies and is therefore not reliable.

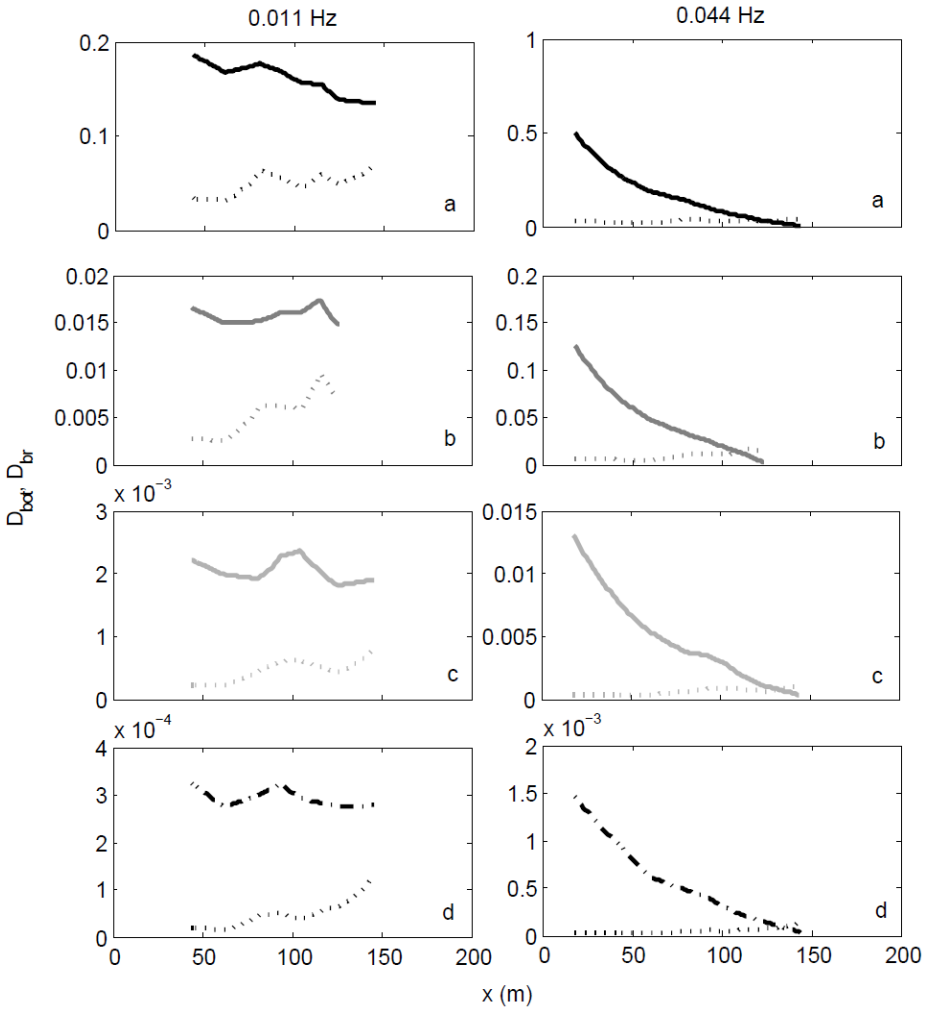

Figure 4.2: Dissipation due to breaking (solid and dash-dotted line) and due to bottom friction (dashed line). On the left (right) for the infragravity frequency of 0.011 Hz (0.044 Hz), for a) Tide 5, b) Tide 41, c) Tide 33 and d) Tide 23.

4.2 Beta parameter

To examine the role of wave breaking further, the relation of the reflection coefficient with the bed slope parameter β_H is determined. *Van Dongeren et al. [2007]* determined this bed slope parameter that governs the amount of reflection of infragravity waves. It is well known that a given bed slope appears steeper, in a manner of speaking, to longer (low frequency) waves, than it does to shorter (high frequency) waves, because the former experience a greater change in depth within a wavelength than the latter. This leads to the dimensionless parameter, the normalized bed slope, expressing the relative depth change per wave length.

Van Dongeren et al. [2007] obtained the following dimensionless parameter (β_H) that represents the normalized bed slope:

$$\beta_H = \frac{h_x}{\omega}\sqrt{\frac{g}{H}}\ , \qquad (14)$$

where h_x is the bed slope, ω is the radian frequency of the low frequency waves, H is the wave height of the incoming long wave near the shoreline and g (9.81 m/s^2) is the gravitational acceleration. Based on their laboratory observations, *Van Dongeren et al. [2007]* define slope regimes that are defined by β_H. The mild-sloping regime (β_H <1.25), where waves are experiencing energy loss due to wave breaking and have minimal reflection, and the steep-sloping regime (β_H >1.25), where waves almost fully reflect.

For our dataset, the amplitude reflection coefficient ($R=\sqrt{R^2}$) indeed depends on β_H *(*Figure 4.3), although the change from mild- to steep-sloping regime is at a higher β_H (≈3). Longer period waves (T > 60 s) are in the steep-sloping regime (β_H >3), whereas shorter period waves (T < 60 s) are in the mild sloping regime (β_H <3).
This confirms the inshore dissipation source of wave breaking noted in chapter 3.
It has to be noted that *Van Dongeren et al. [2007]* estimated β_H and R for the seaward edge of the swash zone for short waves, whereas our estimates are at a more seaward position, due to the lack of swash observations and restrictions of the infragravity separation method which gives results in the centre of the array.

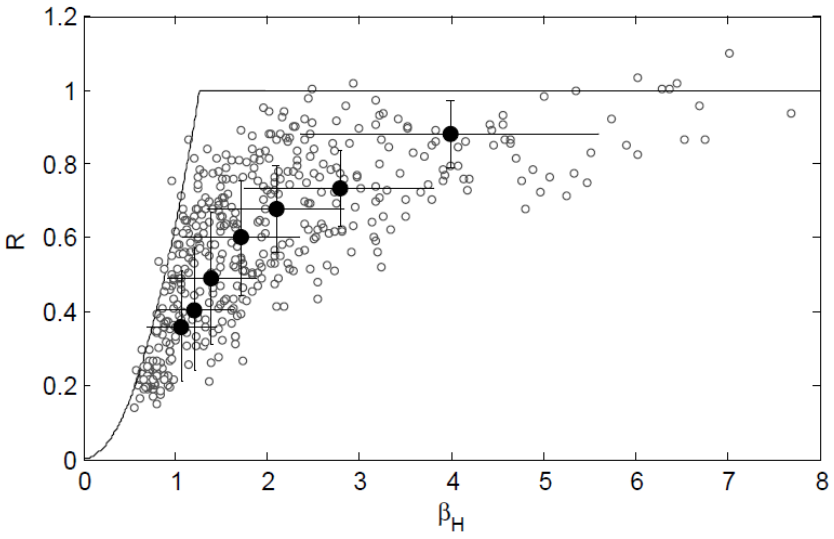

Figure 4.3: Shoreline amplitude reflection coefficient plotted against β_H parameter. Gray dots are for f = 0.011 Hz to f = 0.044 Hz with a step size of 0.0055 Hz. The black dots are the class-mean values for the same frequencies (from 0.011 Hz on the left end to 0.044 Hz on the right end), with error bars of +/- one standard deviation. The fitted line is the relation between R and β_H after Battjes [1974], R = 0.2π β^2_H.

4.3 Infragravity surf zone

In the laboratory experiments of *Battjes et al. [2004]* and *Van Dongeren et al. [2007]* infragravity wave breaking was restricted to the inner part of the sea-swell surf zone. However, for Tide 5 of our dataset, the H_{inf} (Figure 2.10b) suggests a larger zone of breaking.

To determine the size of the infragravity wave surf zone relative to the sea-swell surf zone, gradients of the onshore infragravity wave flux are calculated for the infragravity frequency bands that showed energy dissipation [0.0167-0.05 Hz] and plotted against the normalized position within the sea-swell surf zone.

The non-dimensional positions of the instruments were calculated by combining the wave model of the *Battjes-Janssen model [1978]* with the parameterization for the wave height / water depth ratio of *Battjes and Stive [1985]*. The positions are with regard to the breakpoint (x=1), the swash (x=0) and a position seaward of the surf zone (x>1). Bed friction is neglected.

The cross-shore energy fluxes were calculated from offshore wave and water level data and bed profiles. The cross-shore wave energy flux is constant if the waves are not breaking. If the energy flux is 85% of its offshore value, the edge of the surf zone is assumed to be reached. To check the model predictability, the modeled significant wave height (H_{m0}), is plotted together with the measured H_{m0} in Figure 4.4 for the four tides selected in chapter 2.

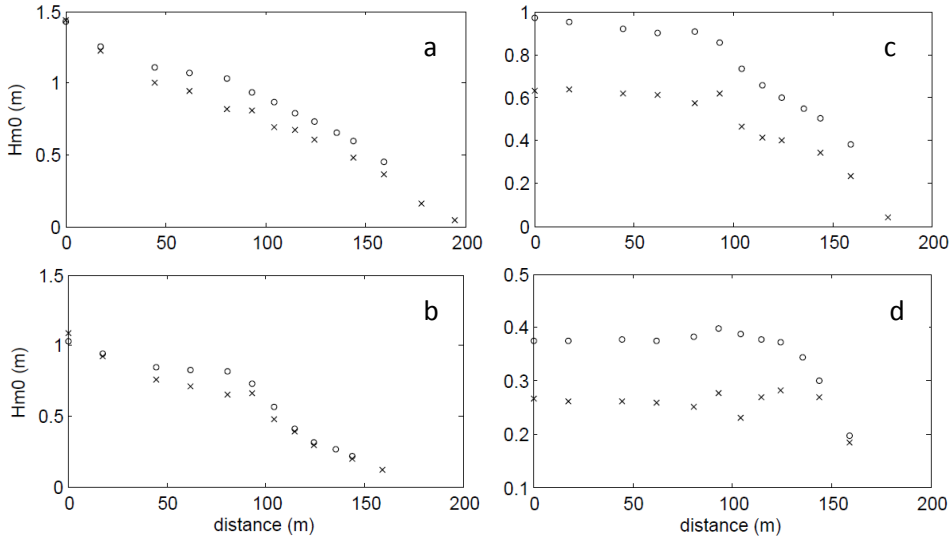

Figure 4.4: Significant wave height along the transect at (a) high (Tide 5) (b) intermediate (Tide 41) (c) low (Tide 33) and (d) lower (Tide 23) energetic conditions. Circles are predictions of the model, crosses are observed data.

During high (Tide 5) and intermediate (Tide 41) energetic conditions the difference in H_{m0} is ~ 10-15 %, possibly due to the neglect of bed friction. The predicted points follow the measured trend very well. For the lower energetic conditions however, the difference is much larger with ~35%. Here it seems that bed friction plays a more important role, although the overall trend is followed quite well.

Plotted against the normalized cross-shore positions, is the gradient of the onshore infragravity energy flux, which was calculated with the *Van Dongeren et al. [2007]* method. The gradient of the flux is estimated using central differences.

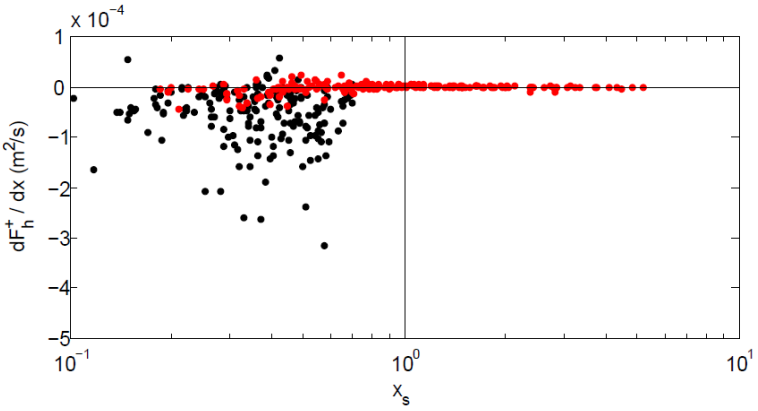

Figure 4.5: Cross-shore gradient in onshore infragravity flux [0.0167-0.05 Hz] dF_h^+/dx, versus normalized cross-shore distance x_s. Black (red) circles are from tides where OSSI1 is inside (outside) the surf zone.

During high energetic conditions, e.g. Tide 5, the gradient in onshore infragravity flux is negative and waves are breaking over the entire transect (OSSI1 up to miniframe 16). Because during Tide 5 the sea-swell surf zone stretches from x =-29.5 to ± x = 175 m during this tide, the region with infragravity wave dissipation in the [f = 0.0167-0.05 Hz] band covers at least 75% of this zone. For other energetic tides similar percentages are found.

When energetic conditions are decreasing, the sea-swell surf zone is becoming smaller as the seaward edge lies closer to the shore. At Tide 23 this is even at x =124 m. In Figure 4.5 the tides where OSSI1 is outside the surf zone are depicted in red. At those tides the gradients in the infragravity onshore flux are small, and only when close to the shore the gradients become negative and waves are breaking.

4.4 Conclusions

Infragravity wave breaking is the mechanism responsible for the energy dissipation seen in Chapters 2 and 3. The shorter period waves (T < 60 s) are largely responsible for this energy loss. Longer period waves (T > 60 s) are in the steep-sloping regime (β_H >3) and have high reflection rates, whereas shorter period waves are in the mild-sloping regime (β_H <3) where waves are dissipating energy due to breaking, and have low reflection rates.

During storm-conditions (e.g. Tide 5) the infragravity wave surf zone can cover at least 75% of the sea-swell surf zone.

5 Sediment suspension and transport direction

The first research question studied in this chapter is: *"Do infragravity waves play a role in the suspension of sediment, or do they solely act as advection mechanism?"*. The second research question is: *"Is sediment transport magnitude and direction, temporal and cross-shore varying? If so, what is the mechanism behind these variations?".* The layout of this chapter is as follows. First the term sediment transport is defined. Secondly, sequences of velocity and concentrations are examined for a possible correlation between low frequency waves and sediment suspension. Then, co-spectra of sediment concentration are examined to determine the dominant transport frequency band and direction at different locations and conditions. Subsequently, sediment transport is divided into gravity band, infragravity band and mean transport.

5.1 Sediment transport calculations

In chapter 3 of Part I, the sediment transport rate is defined as

$$\langle u \cdot c \rangle = \overline{u}\overline{c} + \langle u_h \cdot c_h \rangle + \langle u_l \cdot c_l \rangle , \quad (15)$$

where *u* is cross-shore velocity and *c* is sediment concentration. The term $\overline{u}\overline{c}$ is the current-related sediment transport rate reflecting the transport by the cross-shore mean current. The second and third terms are the oscillatory component corresponding to the transport by short and infragravity waves respectively.

As a reminder of Part I, the infragravity transport can be non-zero for two reasons:

- The infragravity waves are sufficiently strong to entrain sand themselves. This results in suspension events substantially longer than the period of the short waves.
- The infragravity waves are phase-coupled to sand suspension by short waves, for example under bound infragravity waves or in very shallow water where short waves become modulated by infragravity motions.

5.2 Sediment suspension

In this section the role of the infragravity wave in sediment suspension is examined. Therefore, time series of *u* and *c* at different heights above the bed are studied, and correlations between sediment concentrations and short-wave and infragravity wave heights and corresponding velocities are determined.

To see if short waves and infragravity waves are correlated, the infragravity sea surface elevation (η) is plotted with the short-wave envelope. With a negative correlation, the largest short waves are present at the infragravity wave trough (as for bound long

waves), and with a positive correlation the largest short waves are present at the infragravity wave crest (as for free waves in shallow water).

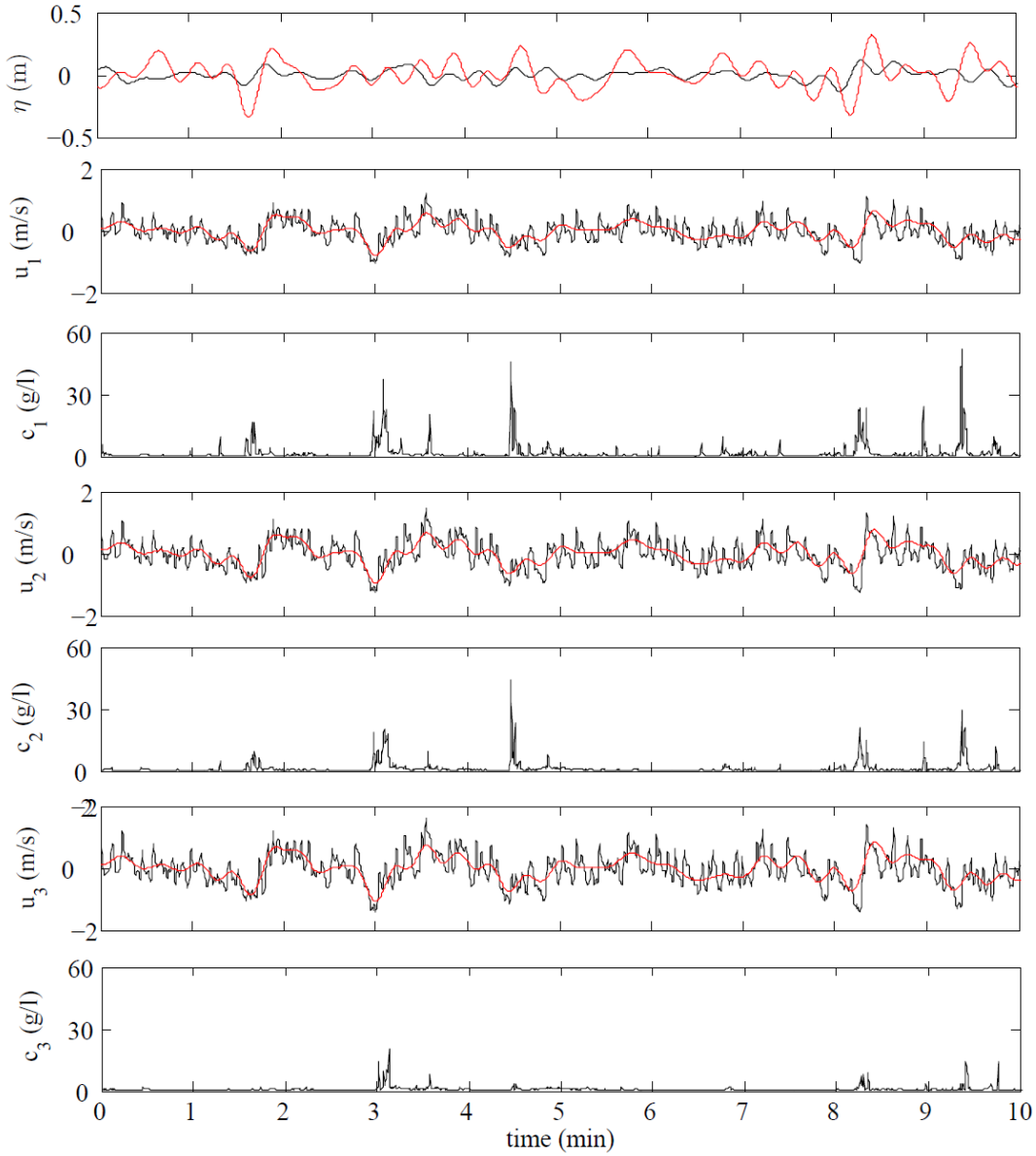

Figure 5.1: For high energetic conditions (Tide 5) at frame 14, sediment concentrations (c in m/s), velocities (u in m/s) for infragravity wave (red) and total velocities (black), and sea surface elevation (η in m) for infragravity and short-wave envelope for low and high short waves (lower frequency filtered). Sediment concentrations c_1 at 0.068 m, c_2 at 0.140 m and c_3 at 0.213 m above the bed.

At high energetic conditions the sediment reached concentrations up to 50 g/l close to the bed which lasted for periods of 10-20 s (Figure 5.1). Higher up the water column, concentrations reached 20 g/l, and lasted for a shorter period of a few seconds. Sediment is suspended at least up to 0.2 m above the bed. *Beach and Sternberg [1988]* also measured equivalent sediment concentrations, that reached high heights in the water column, and they ascribed this to the infragravity wave stirring. Although there has to be noted that the sediment suspensions they observed lasted for a longer period of 30-45 s.

The large concentration bursts in our data seem phase coupled to the infragravity wave trough, where short wave negative velocities reach a maximum. Due to the negative velocities we can expect an offshore transport at low frequencies, $\langle u_l \cdot c_l \rangle$ <0.

Occasional sediment suspension takes place at high positive total velocities, this behavior is only apparent at frame 14 during high energetic conditions. The sediment concentrations decrease strongly with height above the bed, and lasts for a short period of a few seconds.

The correlation between the infragravity wave and the short wave envelope is positive, which means that the largest short waves are predominantly present at the infragravity wave crest. The correlation increases in the shoreward direction from 0.30 at the Truc Vert frame, to 0.57 at frame 16. The largest short waves are present on the infragravity wave crest in shallow water, because the water depth is there temporarily increased, thus wave breaking is less intense. However, in general sediment is not suspended at the infragravity wave crest, but at the trough. This might be because at the infragravity wave trough the water level is lowered and the strong negative infragravity velocities combined with the strong negative short-wave velocities can reach the bed and bring sediment into suspension, whereas during raised water levels at the infragravity wave crest the water motions may not (fully) reach the bed.

At lower energy conditions, e.g. Tide 33, at the same cross-shore location, the sediment concentrations are in the same order as during high energy conditions and reach at least the same height of 0.2 m in the water column (Figure 5.2). However, these sediment bursts are less frequent and because the velocities are much smaller $\langle u_l \cdot c_l \rangle$ will be smaller. In shallower water (not shown here) the maximum concentrations decrease to around 5 g/l, independent of height above the bed. The correlation between the short wave envelope and the infragravity waves is changing from negative to positive in shoreward direction. At the Truc Vert frame the correlation is -0.47, changing to 0.28 at frame 16. This indicates that bound waves are present at seaward positions.

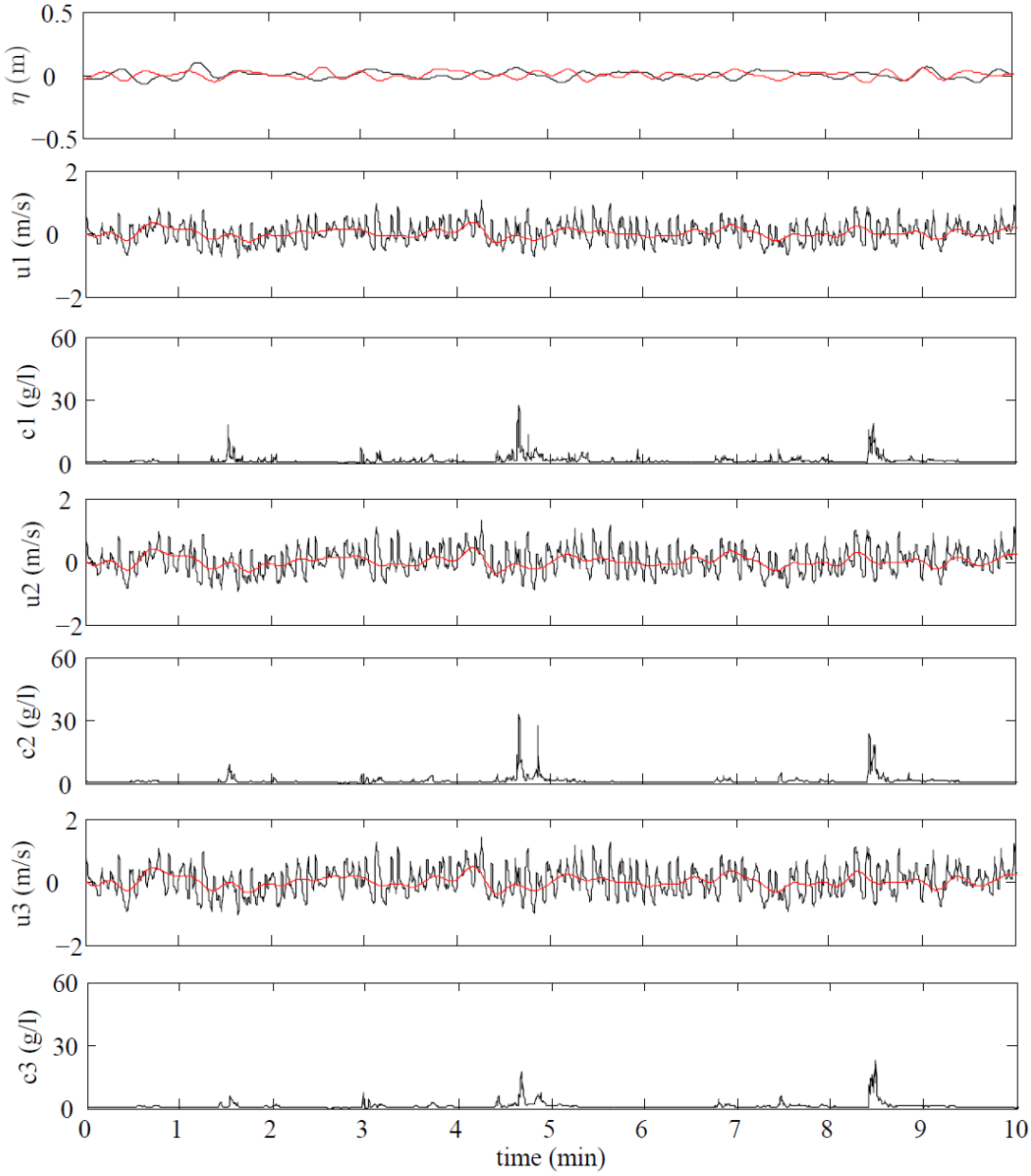

Figure 5.2: For lower energetic conditions (Tide 33) at frame 14, sediment concentrations (c in m/s), velocities (u in m/s) for infragravity wave (red) and total velocities (black), and sea surface elevation (η in m) for infragravity and short-wave envelope for low and high short waves (lower frequency filtered). Sediment concentrations a) at 0.069 m, b) at 0.149 m and c) at 0.220 m above the bottom.

To check if the sediment bursts correlate to infragravity troughs as observed in Figure 5.1, correlations between sediment concentrations and short-wave and infragravity wave characteristics as wave height and velocity are determined in the same way as *Alsina and Cáceres [2011]*. They calculated the correlations with the Pearson's product-moment correlation coefficient (PMCC) for moving averaged values in order to remove possible time lags between instruments, missing data and random effects which might affect it.

The PMCC between two random variables *X* and *Y* is typically defined as the covariance of the two variables divided by the product of their standard deviations:

$$R_{X,Y} = \frac{\mathrm{cov}(X,Y)}{\sigma_X, \sigma_Y}. \quad (16)$$

The moving averaging window is set to 5s. The correlation oscillates between -1 and 1, indicating perfect negative/positive linear dependence between variables, and as it approaches zero there is less of a relationship.

Alsina and Cáceres [2011] found that during high-energy wave conditions sediment suspension events coincided with high square short-wave velocities present at infragravity wave troughs. High suspended sediment concentrations were also observed to coincide with negative peaks in long-wave horizontal velocity modulation. No strong correlation was found with short-wave height, short-wave horizontal velocity or Turbulent Kinetic Energy (TKE). They did find strong correlations of square short-wave velocities at the infragravity wave trough and sediment concentrations of up to R = 0.63, depending on cross-shore location and height above the bed.

For our dataset a moving averaging window is used of 1s, to avoid too much smoothing and thereby manipulation of the data, but to still remove some minor effects present in the data. Correlations with the sediment bursts are calculated for:

- Infragravity wave trough
- Short-wave trough
- Combination of the short-wave trough at the infragravity wave trough, and the infragravity wave trough itself
- Squared negative short-wave velocity
- Squared negative short-wave velocity at the infragravity wave trough
- Squared negative infragravity wave velocity
- Combination of the squared negative short-wave velocity at the infragravity wave trough, and the squared negative infragravity velocity

Only the combined negative velocities at the infragravity wave trough correlate strongly with the sediment bursts, and only during high energetic conditions (Tide 5). All other examined wave characteristics show a weak correlation (<0.1) during all energetic conditions.

The correlation between the sediment bursts and the combined negative velocities at the infragravity wave trough increases in the shoreward direction from 0.05 at the Truc Vert frame to 0.40 at frame 14, 0.63 at frame 15 and 0.99 at frame 16 (Figure 5.3). Although at frame 16 the sediment concentrations are so low that the correlations may be biased.

With increasing height above the bed the correlations decrease to 0.3-0.7 at +/- 15 cm above the bed, and < 0.1 at +/- 20 cm above the bed.

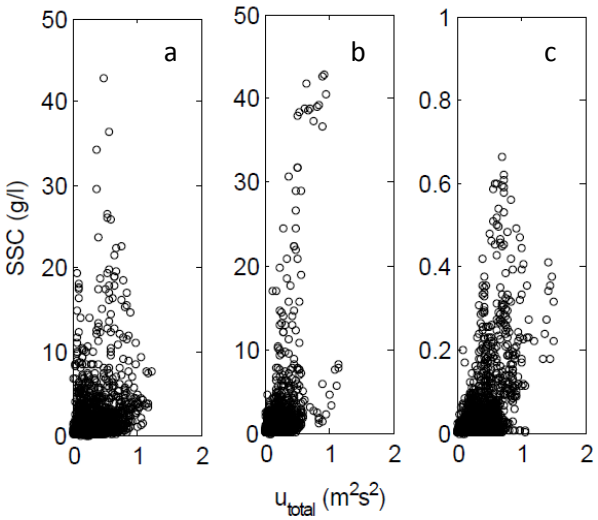

Figure 5.3: Correlation plots between suspended sediment concentration and squared total negative velocities of infragravity and short-waves at the infragravity wave trough at the sensor located closest to the bed at a) frame 14 c_1=0.068m, frame 15 c_1=0.056m, and frame 16 c_1=0.047m, during high energetic conditions (Tide 5).

The dataset of *Alsina and Cáceres [2011]* returns different correlations for high energetic conditions than our data. That might be because of the different beach slope. The results of *Alsina and Cáceres [2011]* are characteristic of a mild sloping beach, that results in an Iribarren number of 0.4. Shoreline dynamics were largely influenced by both short waves and the infragravity waves. Our dataset is characteristic of a low sloping beach, with an Iribarren number of 0.05 at Tide 5 and is showing an infragravity wave dominance.

5.3 Sediment transport

In this section co-spectra of sediment concentration and velocity are plotted to determine the dominant frequency band, and direction of the sediment transport, at different locations and conditions. The role of the current-induced transport will be discussed in section 5.4.

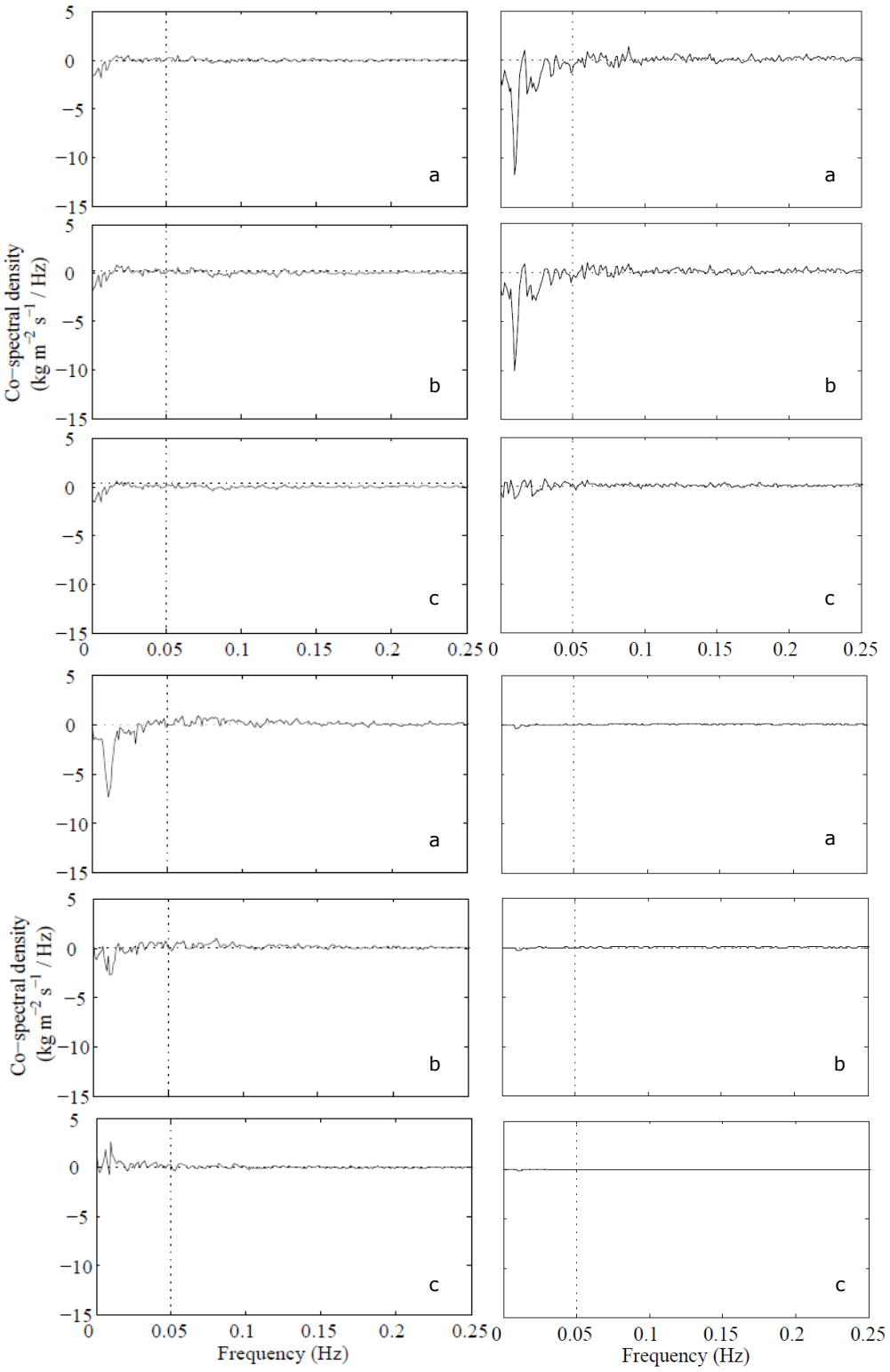

Figure 5.4: Co-spectral density at three heights above the bottom at high energetic conditions. (Top left) Truc Vert frame a) at 0.091 m, at b) 0.155 m, at c) 0.219 m above the bed. (Top right) at frame 14, a) at 0.068 m, b) at 0.140 m and c) at 0.213 m above the bed. (Bottom left) at frame 15, a) at 0.056 m, b) at 0.132 m and c) at 0.222 m above the bed. (Bottom right) at frame 16 a) at 0.047 m, b) at 0.109 m and c) at 0.213 m above the bed.

In the co-spectra density plots for high energetic conditions (Tide 5) (Figure 5.4) a low frequency (< 0.05 Hz) dominance is visible, consistent with *Russell [1993].* He concluded that in the (inner) surf zone of a low sloping beach, during high energetic conditions, a mean offshore transport at infragravity wave frequencies was present. The peak in offshore transport is at 0.011 Hz. At the Truc Vert frame and frame 16 the co-spectral

density is respectively one to two orders of magnitude smaller than at frame 14 and 15. The largest transport is taking place close to the bed, and decreases with height above the bed. At the highest positioned sensors the sediment transport is shifting around zero and does not have a dominant transport direction. The contradicting sediment transport direction that was expected based on Part I (e.g. *Aagaard and Greenwood [2008]*) is not visible.

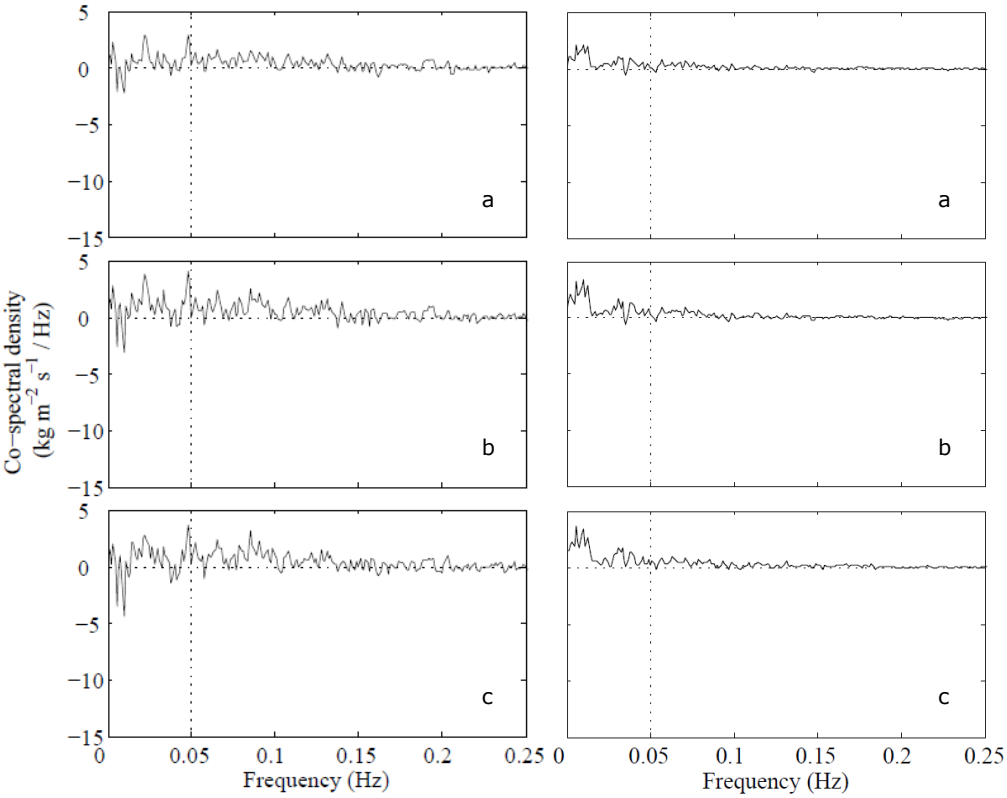

Figure 5.5: Co-spectral density at three heights above the bottom at intermediate (Tide 41) energetic conditions. (Left) at frame 14, a) at 0.153 m, b) at 0.233 m and c) at 0.304 m above the bottom. (Right) at frame 15, a) at 0.117 m, b) at 0.201 m and c) at 0.288 m above the bottom.

The co-spectral density plots at intermediate energetic conditions (Tide 41) are still dominated by the infragravity band (Figure 5.5), but transport is now shifting around zero at frame 14, and is onshore directed at frame 15. The sediment transport at the Truc Vert frame is close to zero (the sensors were > 0.7 m above the bed), and at frame 16 no data is measured. At low energetic conditions (Tide 33 and 23) the short-wave band is equally important as the infragravity wave band.

5.4 Transport components

In this section the relative importance of the short-wave, infragravity and current-induced transport to the total transport are examined. Integration over depth was not

performed because the amount of sensors in the water column is limited. Instead sensors are classified into three regimes; 0-5 cm, 5-10 cm, and >10 cm above the bed.

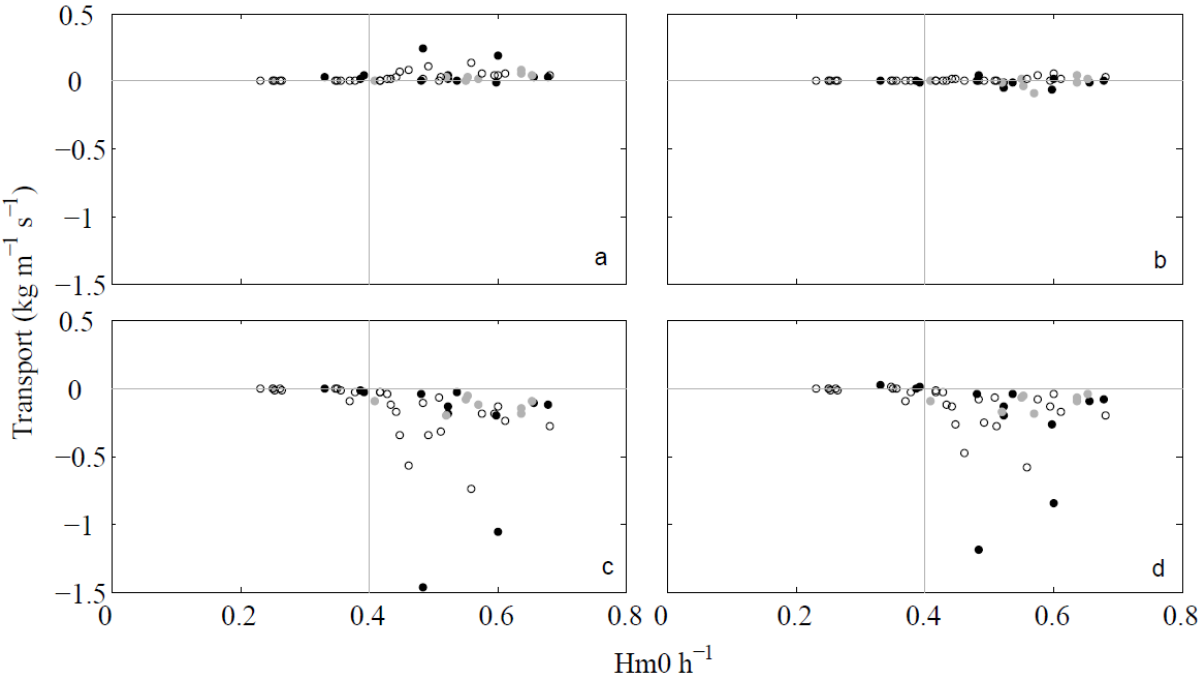

Figure 5.6: Sediment transport at frame 14. Sediment transport by a) short-wave, b) infragravity wave, c) current-induced and d) total transport. Black solid dots are concentrations measured at = 0-5 cm, gray solid dots at 5-10 cm, and black open dots at >10 cm.

Before the short-waves start breaking and *Hm0 h^{-1}* > 0.4, barely any sediment is transported (Figure 5.6). During wave breaking sediment transport is mostly offshore directed, except for the short-wave component where onshore transport dominates. The current-induced transport (R^2=0.95, constant of proportionality is 1.2) and the short-wave sediment transport (R^2=0.52, constant of proportionality is -0.17) dominate the total transport at frame 14. At frame 15 and the Truc Vert frame the current-induced transport dominates as well, but the importance of infragravity and short-wave components increases slightly. At frame 16, total transport is dominated by the infragravity transport (R^2=0.65, constant of proportionality is 1.3) and the current induced transport has decreased (R^2=0.81, constant of proportionality is 0.3).

5.5 Conclusions

Large sediment suspension events at high energetic conditions were found to correlate strongly with large negative velocities at the infragravity wave trough, consisting of both the infragravity and short-wave component. With increase in height above the bed, and in shallower water, concentrations and velocities decrease.

In the co-spectral density of sediment concentrations and cross-shore velocities during high energetic conditions, infragravity dominated offshore transport is visible. So

infragravity waves play a large role in both sediment suspension and the transport of the sediment during high energetic conditions. During low energetic conditions, the transport is smaller and more onshore directed at infragravity frequencies. No contradicting transport direction was found, which is contradicting our hypothesis.
When averaging over the total field campaign, sediment transport is dominated by the current-induced transport, and the infragravity transport is small. The total transport is generally directed offshore.

6 Conclusions

Infragravity waves experience significant energy dissipation during high energetic conditions. This energy dissipation is dependent on frequency. Higher frequencies (>0.0167 Hz) undergo more energy dissipation (R^2<0.1) and display a progressive wave structure. Lower frequencies (<0.0167 Hz) display a standing wave structure, as a large part of their energy is conserved (R^2 = 0.4-0.8).

The mechanism behind the energy dissipation is infragravity wave breaking. The higher frequency waves are in the mild sloping regime (β_H<3), and break, whereas lower frequency waves are in the steep sloping regime and reflect. During storm conditions the infragravity wave surf zone can cover at least 75% of the sea-swell surf zone.

The negative short-wave and infragravity wave velocities at the infragravity wave trough correlate strongly with sediment suspension events. These events last for a period of 10-20 s and reach 50 g/l. Co-spectral density plots show infragravity wave dominance in sediment transport, that is offshore directed. Averaged over the campaign, current-induced transport dominates total transport, that is offshore directed.

Future research

The results point to infragravity energy dissipation due to infragravity wave breaking, but to be able to fully exclude the possibility of energy transfer back to short-waves, bispectral analysis needs to be applied.

Furthermore, a higher resolution data set is needed, that focuses on water depths of 0.5 -1 m, and that consists of more OBS's that cover a larger part of the water column.

7 References

Aagaard, T. and B. Greenwood (2008), Infragravity wave contribution to surf zone sediment transport-the role of advection. Marine Geology 251, 1-14.

Alsina, J.M. and I. Cáceres (2011), Sediment suspension events in the inner surf and swash zone. Measurements in large-scale and high-energy wave conditions. Coastal Eng., 58, 657-670.

Baldock, T. E., D. A. Huntley, P. A. D. Bird, T. O'Hare, and G. N. Bullock (2000), Breakpoint generated surf beat induced by bichromatic wave groups, Coastal Eng., 39, 213–242.

Battjes, J.A. Bakkenes, H.J., Janssen, T.T. and van Dongeren A.R. (2004), Shoaling of subharmonic gravity waves, J. of Geophys.l Res., 109, C02009, doi:10.1029/2003JC001863.

Beach and Sternberg (1991) Infragravity driven suspended sediment transport in swash, inner and outer surf zone. Proc. Coastal sediments '91. ASCE 114-128.

Beach, R.A. and R.W. Sternberg (1998), Suspended sediment transport in the surf zone: response to cross-shore infragravity motion. Marine Geology, 80, 61-79.

Elgar, S., T. H. C. Herbers, and R. T. Guza (1994), Reflection of ocean surface gravity waves from a natural beach, J. Phys. Oceanogr., 24, 1503–1511.

Guza and Thornton (1982), Swash oscillations on a natural beach. J. of Geophysical res. Vol. 81 no. C1, pp. 483-491.

Henderson, S.M., S. Elgar and A.J. Bowen (2000), Observations of surf beat propagation and energetic, Coastal Engineering 2000 - Proc. of the 27th Int. Conf. on Coastal Engineering, ICCE 2000 276, pp. 1412-1421.

Henderson, S. M. and A. J. Bowen (2002), Observations of surf beat forcing and dissipation, J. Geophys. Res., 107(C11), 3193, doi:10.1029/2000JC000498.

Henderson, S. M., R. T. Guza, S. Elgar, T. H. C. Herbers, and A. J. Bowen (2006), Nonlinear generation and loss of infragravity wave energy, J. Geophys. Res., 111, C12007, doi:10.1029/2006JC003539.

Herbers, T. H. C., S. Elgar, R. T. Guza, and W. C. O'Reilly (1995a), Infragravity-Frequency (0.005-0.05 Hz) Motions on the shelf. Part II: Free waves. J. Phys. Oceanogr., 25,1063-1079.

Herbers et al. (1995b), Generation and propagation of infragravity waves. J. Geophys. Res., 100, 24,863-24,872.

Houser, C. and Greenwoord, B. (2005), Hydrodynamics and sediment transport within the inner surf zone of a lacustrine multiple-barred nearshore. Marine Geology 218, pp. 37-63.

Longuet-Higgins, M.S., and Stewart, R.W. (1962), Radiation stress and mass transport in

surface gravity waves with application to "surf beats". J. of Fluid Mech., 13, 481-504.

Miche, M. (1951), Le pouvoir reflechissant des ouvrages maritimes exposes a l'action de la houle. Ann. Points. Chaussees, 121, 285 - 319.

Munk, W.H. (1949), Surf beat, Eos Trans. AGU, 30, 849-854.

Osborne, P.D. and B. Greenwood (1992a), Frequency-dependent cross-shore suspended sediment transport. 1 A non-barred shoreface. Marine Geology 106, 1-24.

Osborne, P.D. and B. Greenwood (1992b), Frequency-dependent cross-shore suspended sediment transport. 2 A barred shoreface. Marine Geology 106, 25-51.

Ruessink, B.G. (1998a), Bound and free infragravity waves in the nearshore zone under breaking and nonbreaking conditions. J. of geophys. res., 103, No. C6, Pages 12,795-12,805, June 15, 1998.

Ruessink, B.G. (1998b), Temporal and spatial variability of infragravity energy in a barred nearshore zone. Cont. Shelf Res. no 18. pp. 585-605.

Ruessink, B.G., Kleinhans, M. G. and Van den Beukel, P.G.L. (1998c), J. of Geophysical res. Vol 103, no C2, pp. 3111-3118.

Ruessink, B.G., Houwman, K.T. and Hoekstra, P. (1998d), The systematic contribution of transporting mechanisms to the cross-shore sediment transport in water depths of 3 to 9 m. Marine Geology 152, pp. 295-324.

Ruggiero, P., Holman, R.A., Beach, R.A., (2004), J. of Geophysical re. Vol. 109 no. C06025.

Russell, P.E. (1993), Mechanisms for beach erosion during storms. Cont. Shelf Res. 13, no. 11 pp. 1243-1265.

Sheremet, A., R. T. Guza, S. Elgar, and T. H. C. Herbers (2002), Observations of nearshore infragravity waves: 1. Seaward and shoreward propagating components, J. Geophys. Res., 107(C8), 3095, doi:10.1029/2001JC000970.

Symonds, G., Huntley, D.A. and Bowen, A.J. (1982). Two dimensional surf-beat: Long wave generation by a time-varying break point. J. of Geophys. Res., 87, 492-498.

Thomson, J., S. Elgar, B. Raubenheimer, T. H. C. Herbers, and R. T. Guza (2006), Tidal modulation of infragravity waves via nonlinear energy losses in the surf zone, Geophys. Res. Lett., 33, L05601, doi:10.1029/2005GL025514.

Tucker, M.J. [1950]. Surfbeats : Sea waves of 1 to 5 minutes period. Proc. R. Soc. London A, 202,565-573.

van Dongeren, A., J. Battjes, T. Janssen, J. van Noorloos, K. Steenhauer, G. Steenbergen, and A. Reniers (2007), Shoaling and shoreline dissipation of low-frequency waves. J. of Geophys. Res., 112, C02011, doi:10.1029/2006JC003701.

Internet

- www.maps.google.com
- www.vvvameland.nl
- Water base historical dataset of Rijkswaterstaat: http://www.rijkswaterstaat.nl/water/scheepvaartberichten_waterdata/historische_waterdata/waterbase/
- Website of the coastal research group of Utrecht University: http://coastalresearch.nl/research/equipment/mini-tripods